



# Università di Ferrara

---

Department of Physics and Earth Science

Master Degree in Physics

Thesis in:

## **Beam dynamics simulations at the hybrid storage ring for EDM investigation**

**Supervisor:**  
**Professor Lenisa Paolo**

**Candidate:**  
**Piccoli Anna**

**Co-Supervisor:**  
**Shankar Rahul**

A.A. 2022-2023



Alla mia Famiglia.



# Abstract

The second half of the last century was marked by many important insights and discoveries in the field of particle physics, first and foremost the development of the Standard Model (SM). However, there are many open questions this model cannot answer; one of them is the baryon asymmetry, i.e. the dominance of matter over antimatter in the Universe.

According to the most accredited theory, the responsible mechanism, called baryogenesis, required the fulfilment of certain necessary conditions within the first moments of the Universe following the Big Bang; the most significant one is the violation of the charge conjugation-parity (CP) symmetry.

The SM predicted value for the asymmetry parameter, which quantifies the baryon asymmetry, is 8 orders of magnitude smaller than the measured one: this means that the SM contributions to CP violation are too weak to explain baryon asymmetry and new sources of CP violation beyond the SM are needed.

The SM is not the ultimate theory of particle physics and among all those developed by theoreticians one of the most plausible extensions, at least till now, is the SUPERSYMMETRY (SUSY) theory. Concerning the baryon asymmetry problem, its characteristic of interest is that the many particle-particle interactions provide more CP violation mechanisms and a non-zero Electric Dipole Moment (EDM) which can be experimentally accessed.

The observation of non-zero EDMs would represent a possible answer to the unsolved problem of baryon asymmetry as well as a clear sign of New Physics beyond the SM.

Very recently a new class of experiments has been proposed to directly measure the EDMs of charged particles via storage rings. In particular, an experimental staged program is presently pursued by the JEDI collaboration at the Forschungszentrum-Jülich in Germany.

The first stage consists in exploiting the COoler SYNchrotron (COSY) to perform feasibility studies on a stored beam of polarized deuterons, the second one deals with construction of a Prototype Storage Ring (PSR) to study the critical features and to develop the key technologies and the last one plans to the construction of the pure electric storage ring to provide the first ever proton EDM (pEDM) measurement.

---

Aim of this thesis is to perform beam dynamics simulations at the hybrid storage ring which is one the proposed lattices for the last stage of the JEDI experiment.

This work is structured into 4 chapters.

Chapter 1 gives the scientific motivation for the EDM investigation.

Initially the CP violation is introduced as the most significant condition for the occurrence of the baryon asymmetry and investigated within and beyond the SM until arriving to the EDM.

Then what the EDM is and how it violates the CP symmetry are explained.

Finally, the experimental background in which the idea for the EDM measurement was developed is presented together with the new proposed method using storage rings.

The beam dynamics in storage rings is discussed in Chapter 2.

The discussion distinguishes between transverse and longitudinal directions and concerns the equation of motions together with their solutions in the matrix formalism, the fields applied and the dedicated devices and the main characteristic effects and principles.

In addition to this, some essentials about spin dynamics are mentioned especially related to the principle of the EDM measurement and the correlated critical aspects.

In Chapter 3 the three staged approach of the JEDI collaboration is introduced: the COSY, the PST and hybrid storage ring.

The layout of the three facilities is described in detail together with the experimental results obtained so far at the COSY.

The experimental results coming from the data analysis on the beam dynamics simulations performed at the hybrid storage ring are presented in Chapter 4.

The simulations performed can be divided into two main categories: the former contains the simulations used to study the 6D phase space and the  $6 \times 6$  transfer matrix, while the latter includes the ones employed in the path lengthening analysis.

# Sommario

La seconda metà del secolo scorso è stata caratterizzata da molte importanti intuizioni e scoperte nell'ambito della fisica delle particelle, primo tra tutti lo sviluppo del Modello Standard. Tuttavia, ci sono molte questioni aperte a cui questo modello non riesce a dare una risposta; una di queste è l'asimmetria barionica, cioè il dominio della materia sull'antimateria nell'Universo.

Secondo la teoria più accreditata, il meccanismo responsabile, chiamato barogenesi, ha richiesto il soddisfacimento di alcune condizioni necessarie entro i primi istanti dell'Universo dopo il Big Bang; la più significativa è la violazione della simmetria coniugazione di carica-parità.

Il valore previsto dal Modello Standard per il parametro di asimmetria, che quantifica l'asimmetria barionica, è di 8 ordini di grandezza inferiore a quello misurato: ciò significa che i contributi del Modello Standard alla violazione di CP sono troppo deboli per spiegare l'asimmetria barionica e quindi sono necessarie nuove fonti di violazione di CP oltre il Modello Standard.

Il Modello Standard non è la teoria definitiva della fisica delle particelle e tra tutte quelle sviluppate dai teorici una delle estensioni più plausibili, almeno fino ad ora, è la teoria della SuperSimmetria. Per quanto riguarda il problema dell'asimmetria barionica, la caratteristica di interesse della teoria della SuperSimmetria è che le numerose interazioni particella-sparticella forniscono più meccanismi di violazione CP e un momento di dipolo elettrico non nullo che può essere sperimentalmente accessibile.

L'osservazione di momenti di dipolo elettrico non nulli rappresenterebbe una possibile risposta al problema irrisolto dell'asimmetria barionica, nonché un chiaro segno di nuova fisica oltre il Modello Standard.

Recentemente è stata proposta una nuova classe di esperimenti per misurare direttamente i momenti di dipolo elettrico delle particelle cariche utilizzando anelli di accumulazione.

In particolare, un programma sperimentale a più fasi è attualmente portato avanti dalla collaborazione JEDI presso il ForschungsZentrum-Jülich in Germania.

---

La prima fase consiste nello sfruttamento del COoler SYnchrotron (COSY) per eseguire studi di fattibilità su un fascio immagazzinato di deuteroni polarizzati, la seconda riguarda la costruzione di un prototipo (PSR) per studiare le caratteristiche critiche e sviluppare le principali tecnologie e l'ultima prevede la costruzione dell'anello di accumulazione puramente elettrico per fornire la prima misura in assoluto del momento di dipolo elettrico del protone.

Scopo di questa tesi è realizzare simulazioni di dinamica di fascio presso l'anello di accumulazione ibrido che rappresenta uno dei reticoli proposti per l'ultima fase dell'esperimento JEDI.

Questo lavoro è strutturato in 4 capitoli.

Il capitolo 1 fornisce la motivazione scientifica dell'indagine sul momento di dipolo elettrico. Inizialmente viene introdotta la violazione della simmetria combinata coniugazione di carica-parità come condizione più significativa per il verificarsi dell'asimmetria barionica e viene indagata all'interno e all'esterno del Modello Standard fino ad arrivare al momento di dipolo elettrico.

In seguito viene spiegato cos'è il momento di dipolo elettrico e come viola la simmetria coniugazione di carica-parità.

Infine, viene presentato il contesto sperimentale in cui è stata sviluppata l'idea della misura del momento di dipolo elettrico e il nuovo metodo proposto che utilizza gli anelli di accumulazione.

La dinamica di fascio negli anelli di accumulazione è discussa nel Capitolo 2.

La trattazione distingue tra le direzioni trasversale e longitudinale e riguarda le equazioni del moto e le loro soluzioni nel formalismo matriciale, i campi applicati e i dispositivi dedicati e i principali effetti e principi caratteristici.

Inoltre, vengono menzionati alcuni concetti essenziali sulla dinamica dello spin, in particolare riguardanti il principio della misura del momento di dipolo elettrico e gli aspetti critici correlati.

Nel Capitolo 3 viene introdotto l'approccio in tre fasi della collaborazione JEDI: il COSY, il PST e l'anello di accumulazione ibrido.

Il layout delle tre strutture è descritto in modo dettagliato insieme ai risultati sperimentali ottenuti finora al COSY.

I risultati sperimentali derivanti dall'analisi dati delle simulazioni di dinamica di fascio realizzate presso l'anello di accumulazione ibrido sono presentati nel Capitolo 4.



---

Le simulazioni effettuate possono essere suddivise in due categorie principali: la prima contiene le simulazioni utilizzate per studiare lo spazio delle fase 6D e la matrice di trasferimento  $6 \times 6$ , mentre la seconda comprende quelle impiegate nell'analisi dell'allungamento del percorso.

---

# Contents

|   |            |
|---|------------|
| <b>Abstract</b>   | <b>V</b>   |
| <b>Sommario</b>   | <b>VII</b> |
| <b>Contents</b>   | <b>XI</b>  |
| <b>1 The EDM as a probe of beyond the SM CP violation</b>                 | <b>1</b>   |
| 1.1 Scientific motivation . . . . .                                       | 1          |
| 1.2 Discrete transformations . . . . .                                    | 3          |
| 1.3 CP violation sources in the SM . . . . .                              | 4          |
| 1.3.1 C and P violations in weak interactions . . . . .                   | 4          |
| 1.3.2 CP violation in weak interactions . . . . .                         | 5          |
| 1.3.3 Other sources of CP violation . . . . .                             | 9          |
| 1.4 CP violation in the SUSY theory . . . . .                             | 10         |
| 1.5 EDM CP violation . . . . .  | 12         |
| 1.6 Past, present and future experiments . . . . .                        | 13         |
| <b>2 Storage ring concepts</b>  | <b>17</b>  |
| 2.1 Frenet-Serret coordinate system . . . . .                             | 18         |
| 2.2 Transverse beam dynamics . . . . .                                    | 19         |
| 2.2.1 Hill's differential equations . . . . .                             | 20         |
| 2.2.2 Solutions to the Hill's differential equations . . . . .            | 24         |
| 2.2.3 Matrix formalism . . . . .  | 25         |
| 2.2.4 Dipole and quadrupole magnets . . . . .                             | 27         |
| 2.2.5 Courant-Snyder phase space ellipse . . . . .                        | 32         |
| 2.2.6 Off-momentum particles: dispersion e chromaticity effects . . . . . | 34         |
| 2.2.7 Sextupole magnets . . . . .   | 35         |
| 2.3 Longitudinal beam dynamics . . . . .                                  | 37         |
| 2.3.1 Radiofrequency cavities . . . . .                                   | 37         |

|          |  |            |
|----------|--|------------|
| 2.3.2    | Phase stability principle . . . . .                            | 38         |
| 2.3.3    | Synchrotron equations of motion . . . . .                      | 40         |
| 2.3.4    | Matrix formalism . . . . .                                     | 42         |
| 2.4      | Spin dynamics . . . . .  | 42         |
| 2.4.1    | Principle of the EDM measurement . . . . .                     | 42         |
| 2.4.2    | Thomas-BMT equation . . . . .                                  | 44         |
| 2.4.3    | Frozen spin condition . . . . .                                | 46         |
| 2.4.4    | Critical aspects . . . . .                                     | 47         |
| <b>3</b> | <b>The JEDI collaboration and experiment at FZ-Jülich</b>      | <b>49</b>  |
| 3.1      | Project overview . . . . .                                     | 49         |
| 3.2      | Staged approach . . . . .                                      | 50         |
| 3.2.1    | Precursor stage: COSY . . . . .                                | 50         |
| 3.2.2    | Proof-of-concept stage: PSR ring . . . . .                     | 53         |
| 3.2.3    | Final stage: pure electric ring . . . . .                      | 55         |
| 3.3      | Hybrid storage ring . . . . .                                  | 56         |
| <b>4</b> | <b>Hybrid storage ring beam dynamics simulations</b>           | <b>59</b>  |
| 4.1      | Bmad and ROOT software . . . . .                               | 59         |
| 4.2      | Lattice . . . . .  | 60         |
| 4.3      | Motivation . . . . .   | 62         |
| 4.4      | 6D phase space and $6 \times 6$ transfer matrix . . . . .      | 63         |
| 4.5      | Path lengthening . . . . .                                     | 71         |
| 4.5.1    | Lattice . . . . .  | 76         |
| 4.6      | Simulations and data analysis results: RF cavity OFF . . . . . | 77         |
| 4.6.1    | Transverse motion contribution . . . . .                       | 77         |
| 4.6.2    | Longitudinal motion contribution . . . . .                     | 83         |
| 4.6.3    | Full formula . . . . .   | 86         |
| 4.7      | Simulations and data analysis results: RF cavity ON . . . . .  | 88         |
|          | <b>Conclusions</b>   | <b>91</b>  |
|          | <b>Appendix A1</b>   | <b>95</b>  |
|          | <b>Appendix A2</b>   | <b>99</b>  |
|          | <b>Appendix B1</b>   | <b>103</b> |

|                     |            |
|---------------------|------------|
| <b>Appendix B2</b>  | <b>111</b> |
| <b>Appendix C1</b>  | <b>121</b> |
| <b>Appendix C2</b>  | <b>125</b> |
| <b>Appendix D</b>   | <b>131</b> |
| <b>Bibliography</b> | <b>133</b> |



## 1

# The EDM as a probe of beyond the SM CP violation

One of the great mysteries of physics is the imbalance between matter and antimatter in the Universe.

According to the most accredited theory, the responsible mechanism involved the violation of the charge conjugation-parity symmetry within the first moments after the Big Bang.

The Standard Model provides some sources of this kind of symmetry violation, but their violation degree is too small to explain the size of the observed asymmetry. New sources beyond the Standard Model must be considered and the electric dipole moment is a powerful probe.

The recent proposal to measure the electric dipole moment of charged particles via storage rings should clarify one of the most puzzling physical problem.

## 1.1 Scientific motivation

The story of the Universe has begun 13.8 billions of years ago. In the scientist community the most accredited theory to explain its origin and expansion is the Big Bang theory. According to it, the Universe has originated and started its expansion from the explosion of an initial state of infinite density and temperature called singularity.

The chronology of the Universe evolution is divided into many epochs each of which is characterized by a particular event of interest. The epochs of the Very Early and Early Universe stages are described in Figure 1.1.

From what is known about the history of the Universe, shortly after the Big Bang both matter and antimatter were produced: the hot dense QGP resulting from the inflationary epoch was made by both quarks and antiquarks which bound together into hadrons and antihadrons during the hadron epoch.

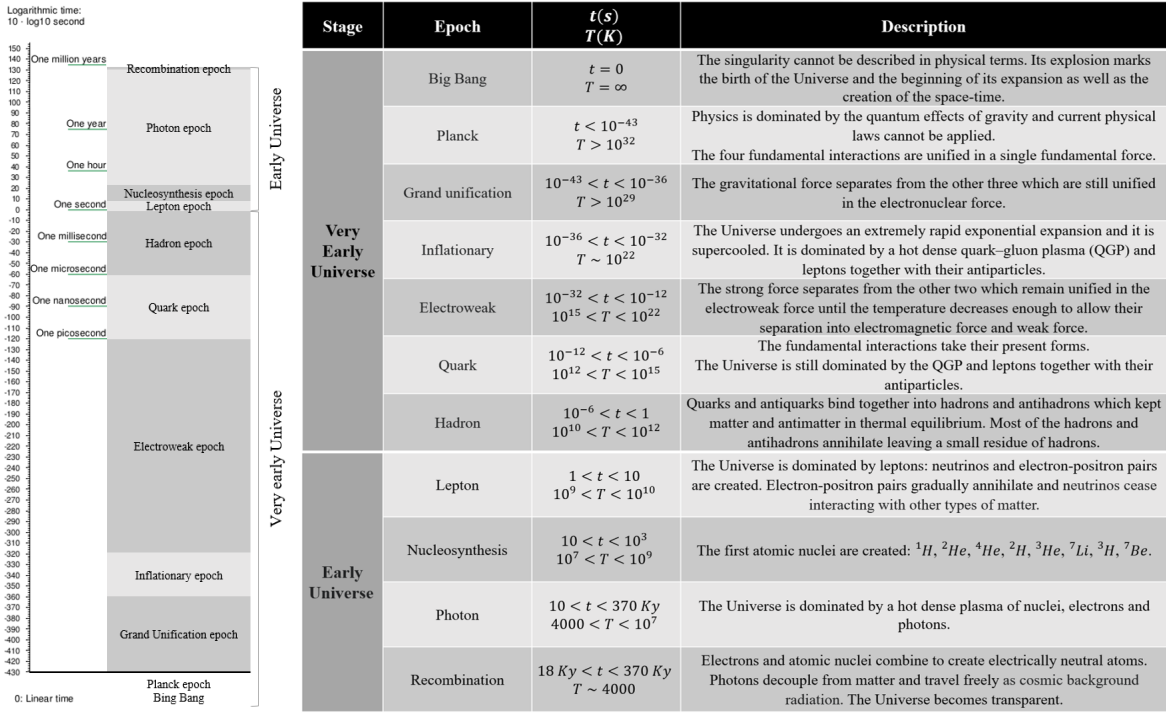


Figure 1.1

Representation of the logarithmic scale timeline of the epochs of the Very Early and Early Universe stages (on the left) and table with the peculiar characteristics of the epochs of the Very Early and Early Universe stages (on the right).

The Big Bang should have produced equal amounts of matter and antimatter, but this was not the case since the annihilation processes between hadrons and antihadrons led to the complete disappearance of antimatter and to the surprising survival of a small amount of matter. Based on some studies on the cosmic background radiation, less than one part in a billion of particles survived the annihilation with antiparticles; in the following billions of years this small amount of matter formed everything present in the Universe.

The imbalance between matter and antimatter is known as baryon asymmetry and it is one of the great mysteries in physics. The responsible physical process is called baryogenesis and probably dates back to the grand unification epoch.

The baryon asymmetry is quantified by the asymmetry parameter which is defined as:

$$\eta = \frac{n_b - n_{\bar{b}}}{n_\gamma} \quad (1.1)$$

where  $n_b$  is the baryon density,  $n_{\bar{b}}$  is the antibaryon density and  $n_\gamma$  is the photon density. Physicists have identified two hypothesis that should explain the baryon asymmetry.



One theory concerns the fact that life has developed in a part of the Universe which is dominated by matter, but there should be other parts dominated by antimatter.

According to the other theory which has received a lot of attention in the last years, baryogenesis is an asymmetric process which needs the fulfilment of certain necessary conditions. These were proposed by Sakharov in 1967:

- baryonic number violation  
It allows to produce an excess of baryons over antibaryons.
- C violation  
It is needed so that the interactions which produce more baryons than antibaryons are not counterbalanced by the interactions which produce more antibaryons than baryons.
- CP violation  
It is required to produce different numbers of left-handed baryons and right-handed antibaryons, as well as different numbers of left-handed antibaryons and right-handed baryons.
- thermal equilibrium violation  
It is necessary to forbid the CPT theorem to assure the compensation between processes increasing and decreasing the baryonic number.

Among these conditions the most significant is the CP violation which implies that a matter process is able to happen at a different rate to its antimatter counterpart. If CP were an exact symmetry, the laws of nature would be completely identical for matter and antimatter and the Universe would contain an equal amount of the two, but it appears to be made of matter.

In the next section the discrete transformations are briefly described.

## 1.2 Discrete transformations

The Nöther's theorem states that if the Lagrangian density of a physical system is symmetric under a certain group of transformations, then there exists a corresponding conservation law and vice versa.

Transformations are divided into two main categories: continuous and discrete. The discrete transformations are parity (P), charge conjugation (C) and time reversal (T).

A parity transformation inverts the spatial coordinates, a charge conjugation transformation turns particles into antiparticles and a time reversal transformation reverses the flow of time.

If a physical system is described by the wavefunction  $\psi(\vec{r}, t)$ , after the individual application of the three transformations the wavefunction transforms as:

$$\psi(\vec{r}, t) \xrightarrow{P} \psi(-\vec{r}, t) \quad (1.2)$$

$$\psi(\vec{r}, t) \xrightarrow{C} \bar{\psi}(\vec{r}, t) \quad (1.3)$$

$$\psi(\vec{r}, t) \xrightarrow{T} \psi(\vec{r}, -t) \quad (1.4)$$

The three transformations collectively are linked by the CPT theorem which states that all the fundamental interactions are symmetric under successive C, P and T transformations taken in any order. It is an exact symmetry and such that one of the basic principles of the Standard Model (SM) confirmed by all the available experiments.

For the individual transformations, the situation is quite different. For years it was assumed that they were exact symmetries as the CPT theorem but starting from the middle of the last century a series of discoveries caused scientific community to change this assumption, in particular in relation to weak interactions.

The next section concerns the symmetries that weak interactions violate and the possible sources of CP violation in the SM.

## 1.3 CP violation sources in the SM

### 1.3.1 C and P violations in weak interactions

The possibility of P violation in weak interactions was suggested by Lee and Yang in 1956 which showed that no experimental proofs existed of P conservation in weak interactions but rather an apparent lack of P conservation existed in the weak decays of  $K^+$  meson since it decays weakly into two final states of opposite parity:

$$K^+ \rightarrow \pi^0 + \pi^+ \rightarrow P = +1 \quad (1.5)$$

$$K^+ \rightarrow \pi^+ + \pi^- + \pi^+ \rightarrow P = -1 \quad (1.6)$$

The experimental proof of P violation arrived in 1957 thanks to the Wu experiment which demonstrated that electrons are preferably left-handed. Furthermore, the same year, the Goldhaber experiment demonstrated that neutrinos are always left-handed and similarly it was shown that antineutrinos are always right-handed.

These were clear manifestations of P maximal violation in weak interactions.

In addition to this, parity violation also implies C violation:

$$\hat{C}v_L = \bar{v}_L \leftarrow \text{not observed} \quad (1.7)$$

$$\hat{C}\bar{v}_R = v_R \leftarrow \text{not observed} \quad (1.8)$$

The symmetry is apparently restored when the combined operation of C and P is considered:

$$\hat{C}\hat{P}v_L = \bar{v}_R \leftarrow \text{observed} \quad (1.9)$$

$$\hat{C}\hat{P}\bar{v}_R = v_L \leftarrow \text{observed} \quad (1.10)$$

Actually, also CP is violated in weak interactions as described in the following.

### 1.3.2 CP violation in weak interactions

The first signs of CP violation in weak interactions arrived from the neutral meson-antimeson pairs.

There exist 4 such doublets:

$$(K^0; \bar{K}^0) \quad (B^0; \bar{B}^0) \quad (B_S^0; \bar{B}_S^0) \quad ; (D^0; \bar{D}^0) \quad (1.11)$$

In 1964 the Cronin-Fitch experiment revealed the CP violation in the neutral kaon system.

The  $K^0$  and  $\bar{K}^0$  mesons are members of the  $J^P = 0^-$  octet.

Experimentally they are distinguishable by their production mode:

$$\pi^- + p \rightarrow K^0 + \Lambda^0 \quad (1.12)$$

$$\pi^+ + p \rightarrow \bar{K}^0 + K^+ + p \quad (1.13)$$

The flavour eigenstates differ from both the CP and mass eigenstates.

The flavour eigenstates are denoted as  $|K^0\rangle$  and  $|\bar{K}^0\rangle$ .

Since the  $K^0$  and  $\bar{K}^0$  mesons are antiparticles of each other, they cannot be CP eigenstates:

$$\hat{C}\hat{P}|K^0\rangle = |\bar{K}^0\rangle \quad (1.14)$$

$$\hat{C}\hat{P}|\bar{K}^0\rangle = |K^0\rangle \quad (1.15)$$

The CP eigenstates are denoted as  $|K_1\rangle$  and  $|K_2\rangle$  and are given by combinations of the flavour eigenstates:

$$|K_1\rangle = \frac{|K^0\rangle + |\bar{K}^0\rangle}{\sqrt{2}} \rightarrow \hat{C}\hat{P}|K_1\rangle = +1|K_1\rangle \quad (1.16)$$

$$|K_2\rangle = \frac{|K^0\rangle - |\bar{K}^0\rangle}{\sqrt{2}} \rightarrow \hat{C}\hat{P}|K_2\rangle = -1|K_2\rangle \quad (1.17)$$

The mass eigenstates are denoted as  $|K_S\rangle$  and  $|K_L\rangle$  ( $S$  and  $L$  stand for *short* and *long* respectively and refer to the lifetimes) and if CP is conserved, then they coincide with the CP eigenstates:

$$|K_S\rangle = |K_1\rangle \quad (1.18)$$

$$|K_L\rangle = |K_2\rangle \quad (1.19)$$

Their masses are very close, while their lifetimes are very different:

$$\Delta m = m_L - m_S = (3.484 \pm 0.006) \times 10^{-12} \text{ MeV} \quad (1.20)$$

$$\tau_S = (89.54 \pm 0.05) \text{ ps} \quad (1.21)$$

$$\tau_L = (51.14 \pm 0.21) \text{ ns} \quad (1.22)$$

They are distinguishable by their decay modes:

$$K_S \rightarrow 2\pi \quad (1.23)$$

$$K_L \rightarrow 3\pi \quad (1.24)$$

The flavour eigenstates can be written as a combination of the mass eigenstates:

$$|K^0\rangle = \frac{|K_S\rangle + |K_L\rangle}{\sqrt{2}} \quad (1.25)$$

$$|\bar{K}^0\rangle = \frac{|K_S\rangle - |K_L\rangle}{\sqrt{2}} \quad (1.26)$$

This means that the neutral kaons are produced and decay as flavour eigenstates but propagate as mass eigenstates, i.e. as mixtures of the flavour eigenstates: this phenomenon is called mixing.

The direct consequence of the mixing phenomenon is the flavour oscillation phenomenon for which a pure  $K^0$  beam develops a  $\bar{K}^0$  component and, as a result, the neutral kaon system oscillates between the two flavour eigenstates as shown by Figure 1.2.

The value of the oscillation period is 13 times the lifetime of  $K_S$ : this means that after few  $ps$  the  $K_S$  component has decayed away, leaving essentially a pure  $K_L$  beam.

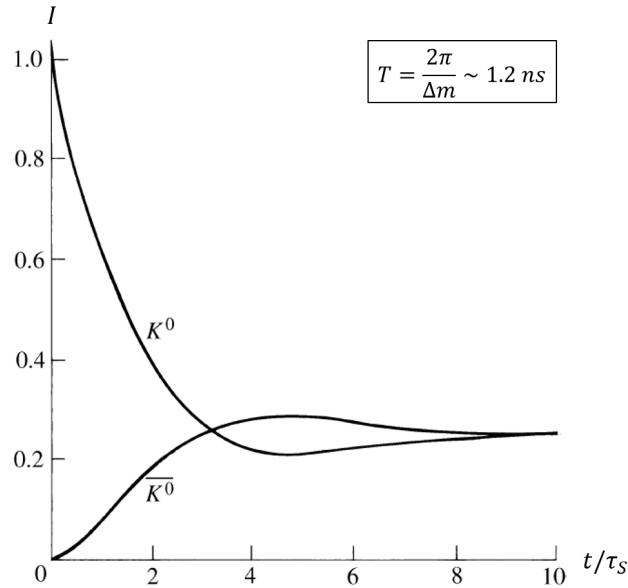


Figure 1.2

Plot of the beam intensity as a function of time normalized to the  $K_S$  meson lifetime which shows the flavour oscillation phenomenon.

The experimental set up of the Cronin-Fitch experiment is shown in Figure 1.3.

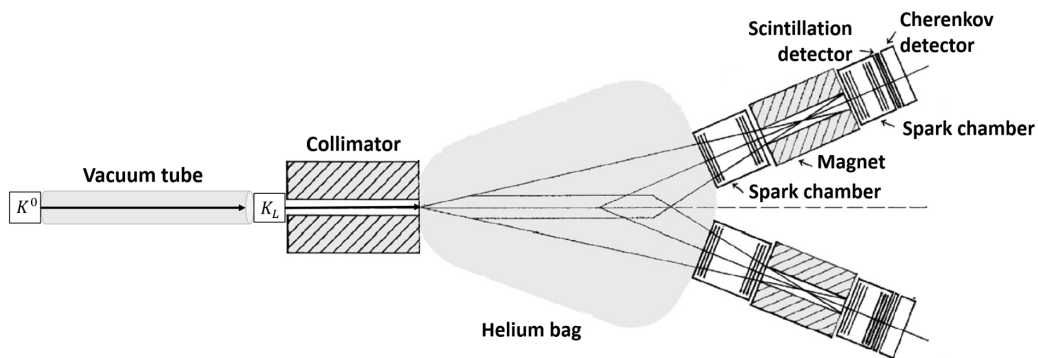


Figure 1.3

Representation of the experimental set up of the Cronin-Fitch experiment.

A pure  $K^0$  beam was injected into a vacuum tube at the end of which, thanks to the flavour oscillation phenomenon, a pure  $K_L$  beam was obtained. The  $K_L$  were collimated and sent into a helium bag where they were left decaying. The decay products were detected by a tracking structure which consisted of a magnet sandwiched between two sparks chambers, a scintillation detector and a Cherenkov detector.

The  $K_L$  should have decayed into  $3\pi$  only, but a few decays into  $\pi^+\pi^-$  were also observed with a branching ratio of  $2 \times 10^{-3}$ . This was the proof that the mass eigenstates do not coincide with the CP eigenstates but can be related to them by a small complex parameter  $\varepsilon$  which represents the degree of CP violation:

$$|K_S\rangle = \frac{|K_1\rangle + \varepsilon|K_2\rangle}{\sqrt{1+|\varepsilon|^2}} \quad (1.27)$$

$$|K_L\rangle = \frac{|K_2\rangle + \varepsilon|K_1\rangle}{\sqrt{1+|\varepsilon|^2}} \quad (1.28)$$

This was the first experimental evidence of CP violation in weak interactions.

Some years after, similar CP violation effects was observed in the other meson-antimeson doublets:

- $B^0$  system  $\rightarrow$  BaBar (SLAC) and Belle (KEK) experiments in 2001;
- $B_s^0$  system  $\rightarrow$  LHCb experiment (CERN) in 2013;
- $D^0$  system  $\rightarrow$  LHCb experiment (CERN) in 2019.

Once established that there were some sources of CP violation in the SM, it was necessary to understand where the CP violation is accounted.

To do this, the discussion about the universality of the weak coupling constant was considered. Differently from leptons, some experiments showed the non-universality of the weak coupling constant for quarks. The solution to this problem was proposed by Cabibbo in 1963 with the quark mixing phenomenon: the interaction eigenstates do not coincide with the mass eigenstates but are combinations of them. In particular, the down-type interaction eigenstates are related to the corresponding mass eigenstates by the Cabibbo matrix::

$$\begin{pmatrix} |d'\rangle \\ |u'\rangle \end{pmatrix} = V_C \begin{pmatrix} |d\rangle \\ |u\rangle \end{pmatrix} = \begin{pmatrix} \cos\theta_C & \sin\theta_C \\ -\sin\theta_C & \cos\theta_C \end{pmatrix} \begin{pmatrix} |d\rangle \\ |u\rangle \end{pmatrix} \quad (1.29)$$

where  $\theta_C \sim 13^\circ$  is the Cabibbo angle.

In 1963 only three quark flavours were known:  $u$ ,  $d$  and  $s$ .

After the discovery of the other flavours, in 1973 the Cabibbo matrix was extended to the CKM matrix:

$$\begin{pmatrix} |d'\rangle \\ |u'\rangle \\ |b'\rangle \end{pmatrix} = V_{CKM} \begin{pmatrix} |d\rangle \\ |u\rangle \\ |b\rangle \end{pmatrix} = \begin{pmatrix} V_{ud} & V_{us} & V_{ub} \\ V_{cd} & V_{cs} & V_{cb} \\ V_{td} & V_{ts} & V_{tb} \end{pmatrix} \begin{pmatrix} |d\rangle \\ |u\rangle \\ |b\rangle \end{pmatrix} \quad (1.30)$$

Its standard parametrization depends on three real parameters ( $\theta_{12}, \theta_{23}, \theta_{13}$ ) and one complex phase ( $\delta$ ):

$$V_{CKM} = \begin{pmatrix} c_{12}c_{13} & s_{12}c_{13} & s_{13}e^{-i\delta} \\ -s_{12}c_{23} - c_{12}s_{23}s_{13}e^{-i\delta} & c_{12}c_{23} - s_{12}s_{23}s_{13}e^{-i\delta} & s_{23}c_{13} \\ s_{12}s_{23} - c_{12}c_{23}s_{13}e^{-i\delta} & -c_{12}s_{23} - s_{12}c_{23}s_{13}e^{-i\delta} & c_{23}c_{13} \end{pmatrix} \quad (1.31)$$

where  $s_{ij} = \sin\theta_{ij}$ ,  $c_{ij} = \cos\theta_{ij}$ ,  $\theta_{12} = \theta_C \sim 13^\circ$ ,  $\theta_{23} \sim 2.3^\circ$  and  $\theta_{13} \sim 0.2^\circ$ .

CP violation is accounted in the SM through the complex phase.

An alternative parametrization is the Wolfenstein one in which the matrix is written as a function of the parameters  $\lambda$ ,  $A$ ,  $\rho$  and  $\eta$ :

$$V_{CKM} = \begin{pmatrix} 1 - \frac{1}{2}\lambda^2 & \lambda & A\lambda^3(\rho - i\eta) \\ -\lambda & 1 - \frac{1}{2}\lambda^2 & A\lambda^2 \\ A\lambda^3(1 - \rho - i\eta) & -A\lambda^2 & 1 \end{pmatrix} \quad (1.32)$$

where  $s_{12} = \lambda = 0.22$ ,  $s_{23} = A\lambda^2$  and  $s_{13}e^{-i\delta} = A\lambda^3(\rho - i\eta)$ .

CP violation requires  $\eta \neq 0$  and currently  $\eta = 0.353 \pm 0.014$ .

### 1.3.3 Other sources of CP violation

According to the current mathematical formulation of the Quantum Chromodynamics (QCD), there are no reasons for CP to be conserved in strong interactions. However, no evidences of CP violation have ever been seen in any experiment involving the strong force. This problem is known as the strong CP problem.

The most well-known solution is the Peccei–Quinn theory. The QCD has a complicated vacuum structure which gives rise to a CP violating  $\bar{\theta}$ -term in the Lagrangian density. The Peccei-Quinn idea is to introduce a new global anomalous symmetry to the SM along with a new scalar field which spontaneously breaks the symmetry at low energies giving rise to a pseudoscalar Goldstone boson called axion whose ground state dynamically forces the Lagrangian density to be CP-symmetric by setting  $\bar{\theta} = 0$ .

Very recently in April 2020 the T2K experiment provided the first evidence of the CP violation in the leptonic sector. The source of CP violation are neutrinos.

Similarly to what happens in the quark sector, the neutrino interaction eigenstates do not coincide with neutrino mass eigenstates but are combinations of them.

The interaction eigenstates and the mass eigenstates are related by the PMNS matrix:

$$V_{CKM} = \begin{pmatrix} c_{12}c_{13} & s_{12}c_{13} & s_{13}e^{-i\delta} \\ -s_{12}c_{23} - c_{12}s_{23}s_{13}e^{-i\delta} & c_{12}c_{23} - s_{12}s_{23}s_{13}e^{-i\delta} & s_{23}c_{13} \\ s_{12}s_{23} - c_{12}c_{23}s_{13}e^{-i\delta} & -c_{12}s_{23} - s_{12}c_{23}s_{13}e^{-i\delta} & c_{23}c_{13} \end{pmatrix} \quad (1.33)$$

where  $s_{ij} = \sin\theta_{ij}$ ,  $c_{ij} = \cos\theta_{ij}$ ,  $\theta_{12} \sim 35^\circ$ ,  $\theta_{23} \sim 45^\circ$  and  $\theta_{13} \sim 10^\circ$ .

Again, if the complex phase is different from zero, then CP is violated.

On the analysis of 9 years of data, the experimental results showed that the probability of  $(\bar{\nu}_\mu \rightarrow \bar{\nu}_e)$  was greater than the probability of  $(\nu_\mu \rightarrow \nu_e)$  with a significance of  $3\sigma$ .

This was the first sign of CP violation in the leptonic sector. Other measurements are needed to confirm this result.

In conclusion, all present results are consistent with the CKM matrix being the only source of CP violation in the SM. However, the SM predicted value for the asymmetry parameter is of the order of  $10^{-18}$ , but the measured one is of the order of  $10^{-10}$ : this means that the SM contributions to CP violation are too small to explain baryon asymmetry and new sources of CP violation beyond the SM are needed.

## 1.4 CP violation in the SUSY theory

The SM is the modern quantum field theory of elementary particles and their fundamental interactions. It has received very strong experimental confirmations and is able to describe with high precision almost all known phenomena in particle physics.

However, it cannot be considered the ultimate theory of particle physics since it leaves several fundamental questions unsolved; one of them is the above-mentioned baryon asymmetry in the Universe.

Since decades theoreticians have been working hard to develop new and more comprehensive and fundamental theories that include the SM as a low energy limit. One of these is the SuperSYmmetry (SUSY) theory. At least till now, it is the most plausible extensions of the SM and works at relatively low energy scale ( $\sim TeV$ ).

In the SUSY theory each SM particle has a super-partner called sparticle which is more massive and differs by half a unit of spin: the super-partner of each spin-1/2 fermion is a spin-0 boson called sfermion, while the super-partner of each spin-1 boson is a spin-1/2 fermion called gaugino. As a result, there exists a sort of symmetry between bosons and fermions: a bosonic state is transformed into a fermionic state and a fermionic state into a bosonic state.



However it is not possible to relate the SM fermions and bosons; the new family of sparticles is needed even if none of these has been observed so far.

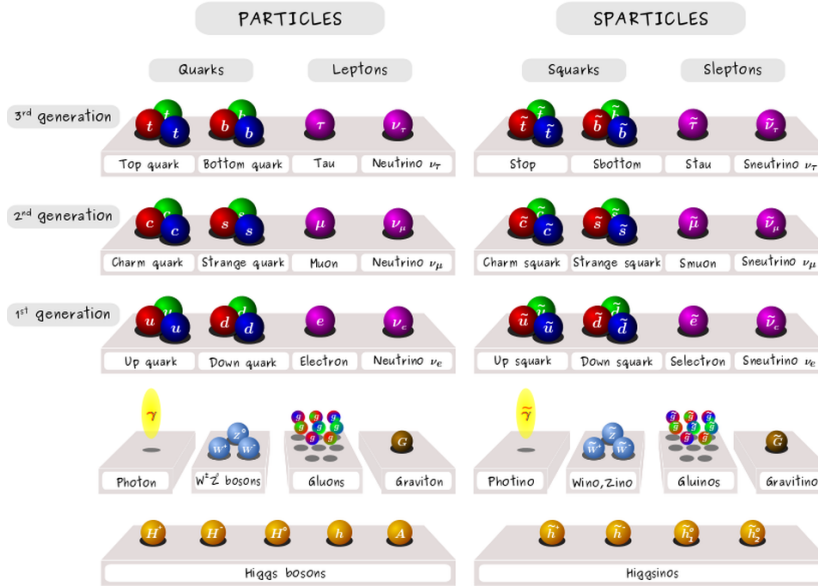


Figure 1.4

Representation of the SM particles and their supersymmetric partners.

The characteristic of interest of the SUSY theory is that the many particle-particle interactions provide more CP violation mechanisms and a non-zero Electric Dipole Moment (EDM) which can be experimentally accessed and thus considered a powerful probe of beyond the SM CP violation as explained in the next section.

Both the SM and the SUSY theory provide a non-zero EDM; the difference between the two is the order of magnitude of the predicted value.

As an example, the SM and SUSY theory predicted values for the neutron EDM are reported:

$$d_{SM}(n) \sim 10^{-32} e \cdot cm \quad (1.34)$$

$$d_{SUSY}(n) \sim 10^{-26} e \cdot cm \quad (1.35)$$

The SUSY predicted value is 6 orders of magnitude greater than the one of the SM and compatible with the experimental limits of the experiments performed in the last decades which makes it “measurable”.

It is important to highlight that in both cases the values are extremely small and this means that such an investigation requires very high-precision experiments. Many of them have been developed and have set important constraints on the upper limits even if no EDM has been measured yet.

## 1.5 EDM CP violation

The EDM is a permanent asymmetry in the distribution of positive and negative electric charges within a particle. Together with the Magnetic Dipole Moment (MDM), it is an intrinsic property of a particle and is defined as:

$$\vec{d} = \frac{\eta q}{2m} \vec{S} \quad (1.36)$$

where  $\eta$  is the gyro-electric factor which depends on the particle,  $q$  is the particle electric charge,  $m$  is the particle mass and  $\vec{S}$  is the particle spin.

It can be aligned either parallel or antiparallel to the spin.

In order to understand why the existence of a non-zero EDM would violate CP, a particle with the EDM parallel to the spin ( $\vec{d} \parallel \vec{S}$ ) is considered, as shown in Figure 1.5.

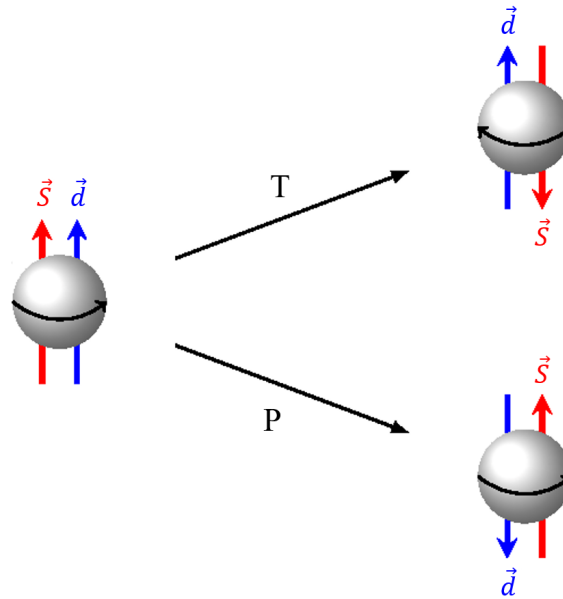


Figure 1.5

Representation of the effect of parity (P) and time reversal (T) transformations on a particle with the EDM ( $\vec{d}$ ) parallel to the spin ( $\vec{S}$ ).

A parity transformation would change the EDM sign leaving the spin unchanged, while in the case of a time reversal transformation the situation would be exactly the opposite: the spin would change sign and the EDM would remain unaltered. As a result, a non-vanishing EDM would violate both P and T and, by assuming the validity of the CPT theorem, the T violation would imply CP violation.

## 1.6 Past, present and future experiments

The idea to use the EDMs of particles as a high precision probe of CP violation is due to Purcell and Ramsey in 1951. Remarkably, it precedes not only the discovery of CP violation in the neutral kaon system (1964) but also the discovery of P violation in weak interactions (1957).

The Purcell-Ramsey method was applied only on neutral particles, especially neutrons, and consisted in five main steps shown in Figure 1.6:

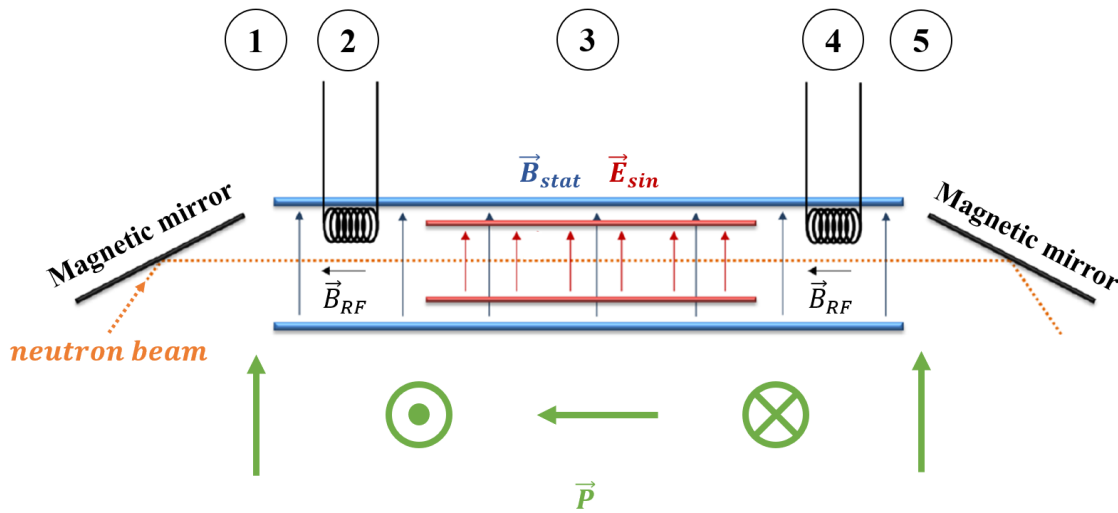


Figure 1.6

Representation of the steps of the Purcell-Ramsey experiment: the green arrows indicate the direction of the polarization of the neutron beam, the black arrows the direction of the solenoidal magnetic field, the blue arrows the direction of the static magnetic field and the red arrows the direction of the sinusoidal electric field.

1. the neutrons were sent onto a magnetic mirror to create a vertically polarized neutron beam.
2. the neutron beam entered the main apparatus where an RF magnetic field created by a coil moved the polarization to the plane perpendicular to the magnetic field completing the so-called  $\pi/2$ -pulse.
3. the neutron beam entered a region with a static magnetic field and a sinusoidal electric field which could be aligned or anti-aligned to the magnetic field and its orientation could be modified by switching the polarity of the plates that generated it.

The magnetic field and the electric field interact with the MDM and the EDM of the neutrons respectively and generated a precession of the polarization whose frequency  $\nu$  is given by:

$$\nu = \frac{2(\mu B \pm dE)}{h} \quad (1.37)$$

where  $\mu$  is the MDM,  $B$  is the magnetic field,  $d$  is the EDM,  $E$  is the electric field,  $h$  is Plank constant and the sign depends on the fact that the electric field was parallel (+) or antiparallel (-) to the magnetic field.

4. a second RF solenoidal magnetic field induced another  $\pi/2$ -pulse to the spins of the neutron. Only the perpendicular polarization component, being in phase with the magnetic field, flipped slowly to the vertical direction, while the other component was essentially unchanged. As a result, the vertical polarization served as a measure for the neutron EDM.
5. by considering the two different cases, i.e.  $\vec{E} \parallel \vec{B}$  and  $\vec{E} \nparallel \vec{B}$ , it was possible to obtain an expression to calculate the neutron EDM:

$$d = \frac{h\Delta\nu}{4E} \quad (1.38)$$

where  $\Delta\nu = \nu_+ - \nu_-$  is the difference between the precession frequency in the two cases.

The results allowed to set an upper bound on the neutron EDM:

$$d(n) \sim 5 \times 10^{-20} e \cdot cm \quad (1.39)$$

Soon after other methods were developed and allowed the measurement of the EDMs of heavy atoms which also led to the indirect estimate of the EDMs of fundamental particles such as the electron and the muon and of charged particles such as the proton.

Despite a constant increase in sensitivity during the last 60 years, these experiments only set upper bounds:

- $d(n) \leq 2.9 \times 10^{-26} e \cdot cm$  (90% C.L.)  $\rightarrow$  derived from ultra-cold neutrons;
- $d(e) \leq 8.7 \times 10^{-29} e \cdot cm$  (90% C.L.)  $\rightarrow$  derived from thorium monoxide molecules;
- $d(\mu) \leq 1.8 \times 10^{-19} e \cdot cm$  (90% C.L.);
- $d(p) \leq 7.9 \times 10^{-25} e \cdot cm$  (95% C.L.)  $\rightarrow$  derived from mercury atoms.

The SM predictions (e.g.,  $d_{SM}(n) \sim 10^{-32} e \cdot cm$ ) are completely out of the reach of the technology of these experiments; nevertheless, they have provided useful constraints on the beyond the SM theories, in particular on the SUSY theory being compatible to its predictions (e.g.,  $d_{SUSY}(n) \sim 10^{-26} e \cdot cm$ ). This fact can be appreciated in Figure 1.7.

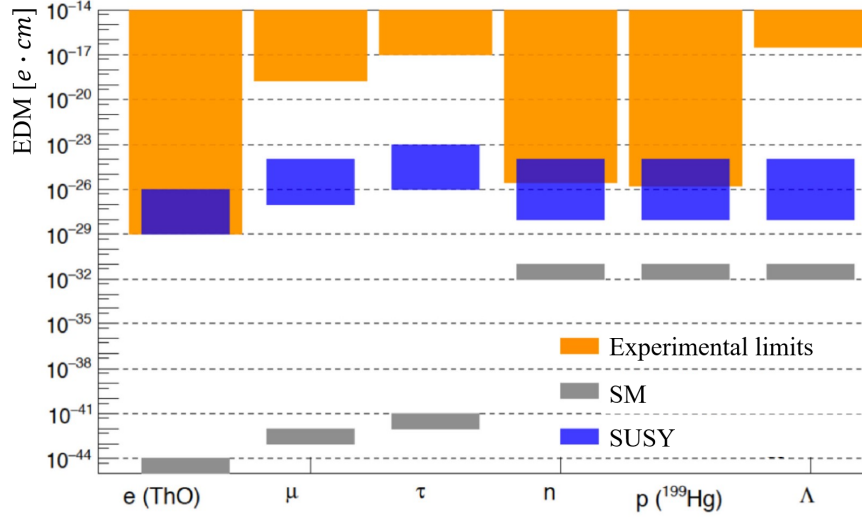


Figure 1.7

Plot of the present experimental limits (orange), the SM predictions (grey) and the SUSY predictions (blue) for the EDM as functions of different particles: electron, muon, tau particle, neutron, proton and lambda particle.

More recently a new class of experiments has been proposed to directly measure the EDMs of charged particles: the basic idea described for neutral particles would not work since charged particle would be lost in an electric field.

The EDM of charged particles can be investigated via storage rings. The basic idea is described as follows: beginning with a longitudinally polarized particle beam, the existence of a non-vanishing EDM can be detected as a rotation of the polarization vector from the longitudinal plane to the vertical axis due to its interaction with a radial electric field.

The use of storage rings can improve the sensitivity up to  $10^{-29} e \cdot cm$ .



## 2

## Storage ring concepts

As mentioned in the previous chapter, the proposed method to measure the EDMs of charged particles requires the use of a storage ring.

A storage ring is a particle accelerator. In particular, it is a confinement system used to accelerate and keep circulating particle beams in a fixed circular closed path.

The most obvious components are the systems that provide beam acceleration and beam guidance and focusing through specific electric and magnetic fields.

A schematic representation of a storage ring is shown in Figure 2.1.

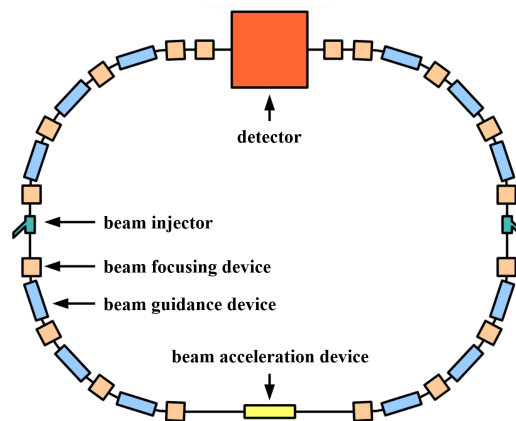


Figure 2.1

Schematic representation of a storage ring with the main components.

Ideally, a particle beam is expected by design to follow closely the prescribed circular closed trajectory called reference orbit. Actually, the majority of the particles are subjected to deviations from it. However, a particle is considered to follow exactly the reference orbit; it is called reference or synchronous particle.

The evolution of particle trajectories is called beam dynamics or beam optics. It can be distinguished into transverse and longitudinal depending on the direction of the fields applied.

The following sections will describe the main features of beam dynamics in a storage ring. In particular, the part designated for the transverse beam dynamics will give details about the transverse equations of motion together with their solutions in the matrix formalism, the transverse fields and the dedicated devices (dipole, quadrupole and sextupole magnets), the transverse phase space and the dispersion and chromaticity effects. On the other hand, the part designated for the longitudinal beam dynamics will give a description of the longitudinal equations of motion together with their solutions in the matrix formalism, the longitudinal fields and the dedicated devices (radio-frequency cavities) and the phase stability principle. In addition to beam dynamics, some information are given about spin dynamics concerning the principle of the EDM measurement, the Thomas-BMT equation, the frozen spin condition and the critical aspects.

However, before doing this, an appropriate coordinate system has to be defined.

## 2.1 Frenet-Serret coordinate system

Since the dimensions of the particle beam and the deviations of the particles from the reference orbit are very small in comparison to the dimensions of the storage ring, the coordinate system is usually defined in relation to the reference particle which represents its origin. In other words, the coordinate system is the rest frame of the reference particle. The choice falls on a curvilinear system called Frenet-Serret coordinate system and shown in Figure 2.2. In particular, the one considered is a left-handed coordinate system since the origin moves clockwise.

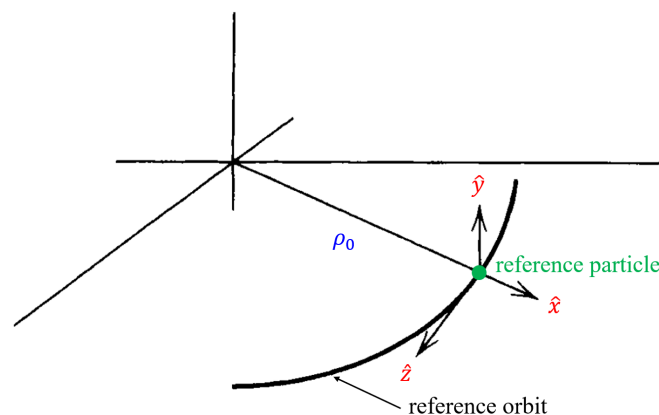


Figure 2.2  
Representation of the left-handed Frenet-Serret coordinate system.



The bending radius of the reference orbit is denoted with  $\rho_0$ . With the origin defined,  $\hat{x}$ ,  $\hat{y}$  and  $\hat{z}$  are the unit vectors respectively in the horizontal, vertical and longitudinal directions. According to these axes, the  $xy$  plane is referred to as the transverse plane, the  $yz$  plane as the vertical plane and the  $xz$  plane as the ring plane.

Any location on the circular closed path is specified by the parameter  $s$  which varies from zero to the total path length and can be considered as an independent variable.

## 2.2 Transverse beam dynamics

The transverse beam dynamics describes the evolution of particle trajectories under the influence of transverse fields.

The transverse deviations are called betatron oscillations. If  $\vec{r}_0(s)$  is the position vector of the reference particle, then the position vector  $\vec{r}(s)$  of a generic particle of the beam subjected to betatron oscillations can be expressed as:

$$\vec{r}(s) = \vec{r}_0(s) + x\hat{x}(s) + y\hat{y}(s) \quad (2.1)$$

where  $x$  and  $y$  are the coordinates defining the position of a generic particle of the beam in the horizontal and vertical directions are respectively.

A representation in the Frenet-Serret coordinate system is shown in Figure 2.3.

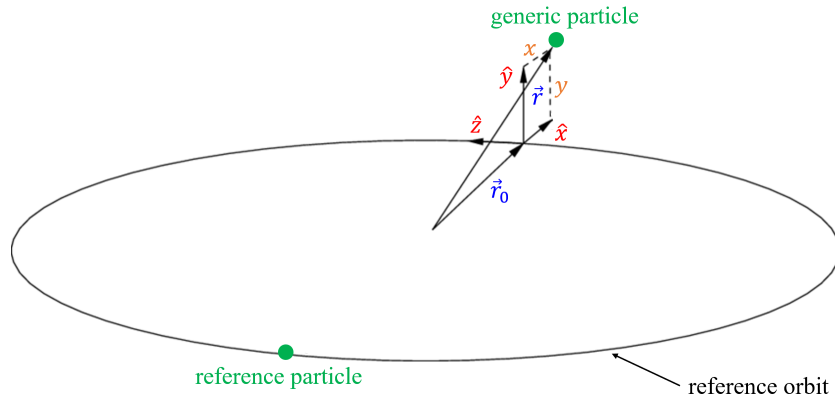


Figure 2.3  
Representation of the betatron oscillations in the Frenet-Serret coordinate system.

The peculiar characteristic of transverse fields is that they allow to bend and focus the particle beam providing beam guidance and focusing. In general, most beam guidance and focusing elements are based on magnetic fields and provided by different types of magnets.

The collection of bending and focusing magnets is called the magnet lattice, while the complete system also including the bending and focusing parameters is referred to be the beam transport system.

In the case of a storage ring, the magnet lattice consists in the succession of magnets and magnet free sections that draw the circular closed path.

### 2.2.1 Hill's differential equations

The force required to provide beam guidance and focusing is the Lorentz force  $\vec{F}_L$ :

$$\vec{F}_L = q(\vec{E} + \vec{v} \times \vec{B}) \quad (2.2)$$

where  $q$  is the particle electric charge,  $\vec{E}$  is the electric field,  $\vec{v}$  is the particle velocity and  $\vec{B}$  is the magnetic field.

For relativistic particles, the force from a magnetic field of 1 T is equivalent to that from an electric field of 300 MV/m. Since it is technically straightforward to generate magnetic fields of the order of 1 T, but rather difficult to establish the equivalent electric fields of 300 MV/m, most beam guidance and focusing elements are based on magnetic fields and the expression of the Lorentz force reduces to:

$$\vec{F}_L \sim q\vec{v} \times \vec{B} \quad (2.3)$$

The equation of motion must be derived for both the horizontal and vertical direction.

The first step is to consider the Lorentz force in the form of an equation of motion:

$$\frac{d\vec{p}}{dt} = q\vec{v} \times \vec{B} \quad (2.4)$$

where  $\vec{p}$  is the particle momentum.

Since the velocity of a generic particle is directed along the longitudinal direction ( $\vec{v} = v_z \hat{z}$ ) and the transverse magnetic field can have both a horizontal and a vertical component ( $\vec{B} = B_x \hat{x} + B_y \hat{y}$ ), the cross product on the right-hand side of equation (2.4) can be rewritten as:

$$\vec{v} \times \vec{B} = \begin{vmatrix} \hat{x} & \hat{y} & \hat{z} \\ 0 & 0 & v_z \\ B_x & B_y & 0 \end{vmatrix} = -v_z B_y \hat{x} + v_z B_x \hat{y} \quad (2.5)$$

Ignoring the radiation emitted by the particle, the left-hand side of equation (2.4) can be rewritten as:

$$\frac{d\vec{p}}{dt} = \frac{d}{dt}(m\gamma\dot{\vec{r}}) = m\gamma\ddot{\vec{r}} \quad (2.6)$$

where  $m$  is the particle mass and  $\gamma$  is the Lorentz factor.

Finally, equation (2.4) becomes:

$$m\gamma\ddot{\vec{r}} = q(v_z B_x \hat{y} - v_z B_y \hat{x}) \quad (2.7)$$

By rearranging equation (2.7), it is possible to derive an expression for  $\ddot{\vec{r}}$

$$\ddot{\vec{r}} = \frac{q(v_z B_x \hat{y} - v_z B_y \hat{x})}{m\gamma} \quad (2.8)$$

The next step is to evaluate  $\ddot{\vec{r}}$  in the Frenet-Serret coordinate system.

The expression of  $\vec{r}$ , neglecting the  $s$  dependence, is given by equation (2.1):

$$\vec{r} = \vec{r}_0 + x\hat{x} + y\hat{y} = \rho_0\hat{x} + x\hat{x} + y\hat{y} = r\hat{x} + y\hat{y} \quad (2.9)$$

where the relations  $\vec{r}_0 = \rho_0\hat{x}$  and  $r = \rho_0 + x$  have been used.

By differentiating equation (2.9), it is possible to derive an expression for  $\dot{\vec{r}}$ :

$$\dot{\vec{r}} = \dot{r}\hat{x} + r\dot{\hat{x}} + \dot{y}\hat{y} \quad (2.10)$$

From Figure 2.4 it is possible to write  $\dot{\hat{x}}$  in terms of  $\hat{z}$ :

$$\dot{\hat{x}} = \dot{\theta}\hat{z} \quad (2.11)$$

where  $\dot{\theta} = v_z/r$ .

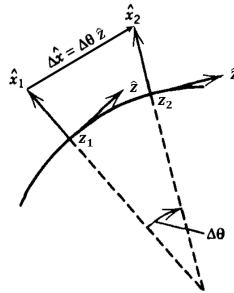


Figure 2.4

Scheme to evaluate the time rate of change of the horizontal unity vector.

Therefore, equation (2.10) becomes:

$$\dot{\vec{r}} = \dot{r}\hat{x} + r\dot{\theta}\hat{z} + \dot{y}\hat{y} \quad (2.12)$$

By differentiating equation (2.10), it is possible to derive an expression for  $\ddot{\vec{r}}$ :

$$\ddot{\vec{r}} = \ddot{r}\hat{x} + (r\ddot{\theta} + 2\dot{r}\dot{\theta})\hat{z} + r\ddot{\theta}\hat{z} + \ddot{y}\hat{y} = \ddot{r}\hat{x} + (r\ddot{\theta} + 2\dot{r}\dot{\theta})\hat{z} - r\dot{\theta}^2\hat{x} + \ddot{y}\hat{y} \quad (2.13)$$

where the relation  $\dot{\hat{z}} = -\dot{\theta}\hat{x}$  has been used. It has been obtained by the same argument as used for equation (2.11).

Finally, equation (2.8) becomes:

$$\ddot{r}\hat{x} + (r\ddot{\theta} + 2\dot{r}\dot{\theta})\hat{z} - r\dot{\theta}^2\hat{x} + \ddot{y}\hat{y} = \frac{q(v_z B_x \hat{y} - v_z B_y \hat{x})}{m\gamma} \quad (2.14)$$

The equations of motion in the horizontal and vertical directions are respectively:

$$\ddot{r} - r\dot{\theta}^2 = -\frac{qv_z^2 B_y}{p} \quad (2.15)$$

$$\ddot{y} = \frac{qv_z^2 B_x}{p} \quad (2.16)$$

By substituting the time derivatives with the derivatives with respect to the independent variable  $s$ , equations (2.15) and (2.16) become:

$$\frac{d^2x}{ds^2} - \frac{\rho_0 + x}{\rho_0^2} = -\frac{q}{p} B_y \left(1 + \frac{x}{\rho_0}\right)^2 \quad (2.17)$$

$$\frac{d^2y}{ds^2} = \frac{q}{p} B_x \left(1 + \frac{x}{\rho_0}\right)^2 \quad (2.18)$$

Since the betatron oscillations are small compared to the bending radius of the reference orbit, the magnetic field can be expanded resulting in:

$$\vec{B} = B_x \hat{x} + B_y \hat{y} \sim \left[ B_x(0,0) + \frac{\partial B_x}{\partial y} y + \frac{\partial B_x}{\partial x} x \right] \hat{x} + \left[ B_y(0,0) + \frac{\partial B_y}{\partial x} x + \frac{\partial B_y}{\partial y} y \right] \hat{y} \quad (2.19)$$

With this approach, the effects of the magnetic field are analysed as the superposition of different components.

Usually the assumptions of a planar storage ring, i.e.  $B_x(0,0) = 0$ , and decoupled transverse motions, i.e.  $(\partial B_x)/\partial x = (\partial B_y)/\partial y = 0$ , are considered to simplify the problem.

As a result, the betatron equations of motion are given by the Hill's differential equations whose expressions in the horizontal and vertical directions are respectively:

$$\frac{d^2x}{ds^2} + \left[ \frac{1}{\rho_0^2} + \frac{q}{p} \frac{\partial B_y(s)}{\partial x} \right] x = 0 \quad (2.20)$$

$$\frac{d^2y}{ds^2} - \frac{q}{p} \frac{\partial B_y(s)}{\partial x} y = 0 \quad (2.21)$$

It is important to be aware of the fact that they are not the most general equations of motion: since the expansion of the magnetic field given by equation (2.19) ends at the 1st order, only the dipole and quadrupole components have been considered. However, these components are sufficient to define the basic formulation of transverse beam dynamics because they guarantee the beam guidance and focusing through dipole and quadrupole magnets respectively.

The derivatives of the magnetic field in the Hill's differential equations can be related to the magnet strength parameter defined as:

$$s_n = \frac{q}{p} \frac{\partial^{n-1} B_y}{\partial x^{n-1}} \Big|_{x=y=0} \quad (2.22)$$

For dipole magnets  $n = 1$  and  $s_1 = \kappa$ , while for quadrupole magnets  $n = 2$  and  $s_2 = k$ .

Introducing the magnet strength parameter, the Hill's differential equations become:

$$x''(s) + [\kappa^2 + k(s)]x = 0 \quad (2.23)$$

$$y''(s) - k(s)y = 0 \quad (2.24)$$

It can be noticed that the equation in the horizontal direction contains both the dipole and the quadrupole components because the horizontal motion need to be both bent and focused. On the other hand, the equation in the vertical direction contains only the quadrupole component because the vertical motion need only to be focused due to the planar storage ring assumption. The transverse beam dynamics based on only the two lowest order magnet types is defined as linear because relies only on linear fields which are independent of or linearly dependent on the distance of a generic particle of the beam from the reference orbit. With this approach it is correct to consider the motions in the two transverse directions as independent.

Considering higher order components in the magnetic field expansion, the equations of motion would acquire a lot of other terms and other types of magnets would be added to the magnet lattice providing specific corrective effects.

The building of magnets with almost ideal field properties is of great importance to treat the higher order terms as small perturbations and mathematical perturbation methods can be employed to describe their effects.

From now on, the linear transverse beam dynamics approximation is considered.

## 2.2.2 Solutions to the Hill's differential equations

After the derivation of the Hill's differential equations, the discussion moves to the research for their solutions.

They are both of the form:

$$u''(s) + K(s)u(s) = 0 \quad (2.25)$$

where  $u$  is a transverse coordinate which stands for both  $x$  and  $y$  and  $K$  is the magnet strength parameter whose expression can be either  $K_x = \kappa^2 + k(s)$  or  $K_y = -k(s)$  depending on the coordinate considered.

In the attempt to solve it, the first step consists in considering the magnet strength parameter as constant:

$$u''(s) + Ku(s) = 0 \quad (2.26)$$

The principal solutions are defined for  $K > 0$  and  $K < 0$ :

$$K > 0: \begin{cases} C(s) = \cos(\sqrt{K}s) \\ S(s) = \frac{1}{\sqrt{K}}\sin(\sqrt{K}s) \end{cases} \quad K < 0: \begin{cases} C(s) = \cosh(\sqrt{|K|}s) \\ S(s) = \frac{1}{\sqrt{|K|}}\sinh(\sqrt{|K|}s) \end{cases} \quad (2.27)$$

These linearly independent solutions satisfy the following initial conditions:

$$K > 0: \begin{cases} C(0) = 1 \\ S(0) = 0 \\ C'(0) = \frac{dC}{ds}\Big|_0 = 0 \\ S'(0) = \frac{dS}{ds}\Big|_0 = 1 \end{cases} \quad (2.28)$$

Any arbitrary solution can be expressed as a linear combination of the principal solutions (2.27):

$$\begin{cases} u(s) = C(s)u_0 + S(s)u'_0 \\ u'(s) = C'(s)u_0 + S'(s)u'_0 \end{cases} \quad (2.29)$$

where  $u_0$  and  $u'_0$  are two arbitrary initial parameters of the trajectory.

However, in a real beam transport system, the magnet strength parameter is not constant and the equation (2.25) must be considered.

By inserting solutions (2.29) in equation (2.25), the following equation is obtained:

$$[S''(s) + K(s)S(s)]u_0 + [C''(s) + K(s)C(s)]u'_0 = 0 \quad (2.30)$$

This equation must be true for any pair of initial parameters  $(u_0, u'_0)$  and therefore the coefficients must vanish separately:

$$\begin{cases} S''(s) + K(s)S(s) = 0 \\ C''(s) + K(s)C(s) = 0 \end{cases} \quad (2.31)$$

The general solution of the equation of motion (2.25) can be expressed as a linear combination of a pair of solutions satisfying the differential equations (2.31) and the initial conditions (2.28). However, it is impossible to solve equation (2.25) analytically in a general way that would be correct for any arbitrary beam transport system. To do this, it is necessary to introduce a mathematical tool: the matrix formalism.

### 2.2.3 Matrix formalism

The matrix formalism allows to describe analytically the particle trajectories in any arbitrary beam transport system composed of dipole and quadrupole magnets.

The idea behind this method is the following: by cutting the beam transport system into smaller uniform pieces each of which is characterized by a constant magnet strength parameter, it is possible to follow the particle trajectories step by step through the whole beam transport system. This is feasible because the linear beam dynamics uses the hard-edge model for which the magnetic field is zero in magnet free sections and assumes a constant value within the magnets resulting in a step function distribution; therefore, the path is composed of a series of segments with constant curvatures and magnet strength parameters.

It is an approximation, although for practical purposes a rather good one. In a real beam transport line the field strength does not change suddenly from zero to full value but rather follows a smooth transition from zero to the maximum field. It is important to keep in mind that in some cases a correction is needed to consider the effects of a smooth field transition at the magnet edges.

Using this approach, equation (2.25) is reduced to (2.26) and the arbitrary solution given by equation (2.29) can be expressed in matrix form as:

$$\begin{pmatrix} u(s) \\ u'(s) \end{pmatrix} = \begin{pmatrix} C_z(s) & S_z(s) \\ C'_z(s) & S'_z(s) \end{pmatrix} \begin{pmatrix} u_0(s) \\ u'_0(s) \end{pmatrix} = M \begin{pmatrix} u_0(s) \\ u'_0(s) \end{pmatrix} \quad (2.32)$$

where  $M$  is the transformation matrix.

Such a transformation matrix is obtained for each individual element of the beam transport system and thanks to matrix formalism it is possible to follow particle trajectories along a complicated beam transport system by repeated matrix multiplications from element to element. With this method, the need to solve the differential equation (2.25) is completely eliminated.

The transformations matrices are derived for both dipole and quadrupole magnets.

A generic particle of the beam has initial coordinates  $(u, u')_{initial}$ . After having passed through either a dipole magnet or a quadrupole magnet of length  $L$  it will have coordinates  $(u, u')_{final}$ . The most general solution in matrix form is:

$$\begin{pmatrix} u(s) \\ u'(s) \end{pmatrix}_{final} = M \begin{pmatrix} u(s) \\ u'(s) \end{pmatrix}_{initial} \quad (2.33)$$

In the case of a dipole magnet, the magnet strength parameter is zero and the transformation matrix is:

$$M = \begin{pmatrix} 1 & L \\ 0 & 1 \end{pmatrix} \quad (2.34)$$

In the case of a quadrupole magnet, the magnet strength parameter can be either positive or negative indicating either a focusing or a defocusing effect respectively.

The transformation matrix for the focusing effect is:

$$M_{QF} = \begin{pmatrix} \cos(\sqrt{K}L) & \frac{1}{\sqrt{K}}\sin(\sqrt{K}L) \\ -\sqrt{K}\sin(\sqrt{K}L) & \cos(\sqrt{K}L) \end{pmatrix} \quad (2.35)$$

Similarly, the transformation matrix for the defocusing effect is:

$$M_{QD} = \begin{pmatrix} \cosh(\sqrt{|K|}L) & \frac{1}{\sqrt{|K|}}\sinh(\sqrt{|K|}L) \\ -\sqrt{|K|}\sinh(\sqrt{|K|}L) & \cosh(\sqrt{|K|}L) \end{pmatrix} \quad (2.36)$$

Any arbitrary sequence of dipole and quadrupole magnets can be represented by a series of transformation matrices  $M_i$ . The transformation matrix for the whole composite beam transport line is just equal to the product of the individual matrices.



## 2.2.4 Dipole and quadrupole magnets

As mentioned before, the peculiar characteristic of transverse fields is that they provide beam guidance and focusing through dipole and quadrupole magnets respectively.

To study more in details the magnetic field generated by dipole and quadrupole magnets, the starting point is the magnetic field expansion given by equation (2.19) together with the assumption of a planar storage ring.

The magnetic field in the horizontal and vertical directions are respectively:

$$B_x = \frac{\partial B_y}{\partial y} y \quad (2.37)$$

$$B_y = B_y(0,0) + \frac{\partial B_x}{\partial x} x \quad (2.38)$$

The dipole component is given by the  $0^{th}$  order term, while the quadrupole component by the  $1^{st}$  order term: this means that a dipole magnet generates a constant uniform magnetic field directed along the vertical axis, while a quadrupole magnet creates a magnetic field directed along both the horizontal and vertical axes whose magnitude grows linearly with the radial distance from the longitudinal axis. The dipole and quadrupole magnetic fields are shown in Figure 2.5.

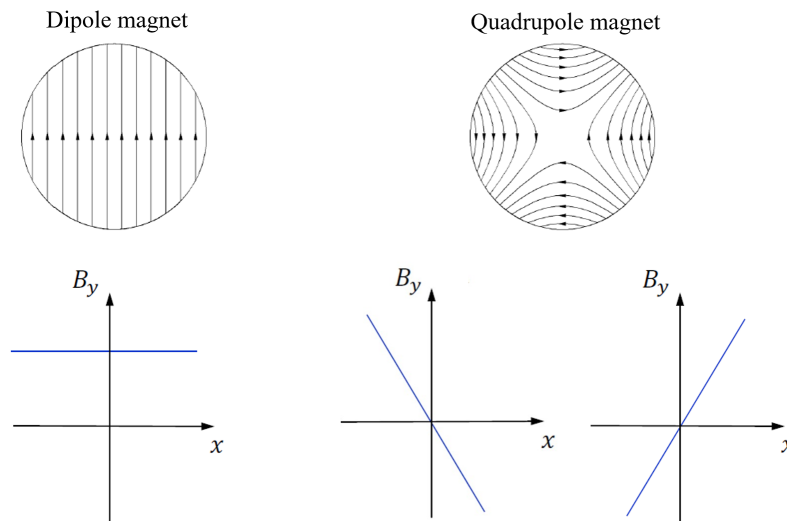


Figure 2.5

Representation of the dipole and quadrupole magnetic fields.

Due to the dipole magnetic field, the particle motion occurs in the ring plane, is collinear to the direction of particle velocity and free in the direction perpendicular to it. Thus, a particle injected into a storage ring travels a circular trajectory.

Normally the quadrupole magnetic field is arranged in such a way that the reference orbit passes through its centre: this means that a particle on the reference orbit feels a null magnetic field and the more the particle is distant from the reference orbit, the greater the effect of the magnetic field on it.

The reference orbit is defined geometrically by straight sections and dipole magnets only that are placed wherever the path needs to be deflected. Quadrupole magnets do not influence this path but provide the focusing necessary to keep all particles close to the reference orbit. They are both necessary to guarantee a basic stable transverse motion.

The condition which ensures beam guidance comes from setting the Lorentz force equal to the centrifugal force:

$$qvB = \frac{m\gamma v^2}{\rho} \quad (2.39)$$

where  $\rho$  is the bending radius of the trajectory of a generic particle of the beam.

From equation (2.39) it is possible to obtain the condition that describes how the dipole field influences the bending effect:

$$\frac{1}{\rho} = \frac{q}{p} B \quad (2.40)$$

Since the dipole field is constant, it is clear that if the particle velocity is constant, then the bending radius is constant too and turn by turn the particle moves on a specific circular closed path. However, if the particle velocity changes, then turn by turn the particle travels a different path whose bending radius varies according to the velocity and to maintain the particle on a specific path the magnetic field must change accordingly. For this reason the sole dipole magnets cannot provide a stable transverse motion and beam guidance is always associated with beam focusing provides by quadrupole magnets whose field changes with distance.

Furthermore, equation (2.40) gives the dipole field to set in order to maintain a particle on a circular closed path characterized by a certain bending radius and allows to define an expression for the beam rigidity:

$$B\rho = \frac{p}{q} \quad (2.41)$$

It refers to the fact that a higher momentum particle has a higher resistance to deflection by the dipole field.

The simplest example of a dipole magnet is a bar magnet. In a storage ring two bar magnets are arranged in such a way that the north pole of one faces the south pole of the other.

An example is shown in Figure 2.6.



Figure 2.6  
Image of a dipole magnet.

The simplest quadrupole magnet consists of two identical bar magnets parallel to each other such that the north pole of one is next to the south of the other and vice versa. In a storage ring the four poles are arranged along the diagonals on the plane transverse to the particle beam propagation axis, as shown in Figure 2.7.

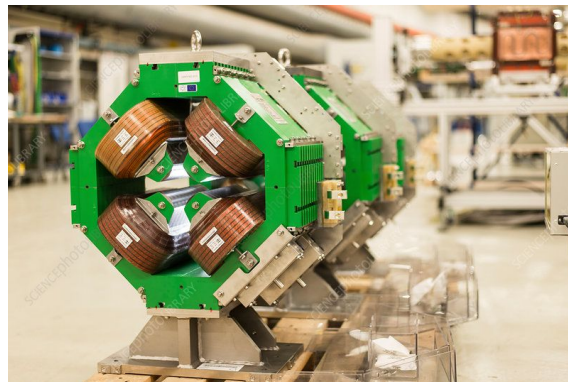


Figure 2.7  
Image of a quadrupole magnet.

Each quadrupole magnet has both a focusing and a defocusing effect. Typically a focusing quadrupole (QF) magnet is horizontally focusing but vertically defocusing, while a defocusing quadrupole (QD) magnet acts in the opposite way. Quadrupole magnets focus particles exploiting the strong focusing method based on alternating gradient field focusing.

An example is shown in Figure 2.8.

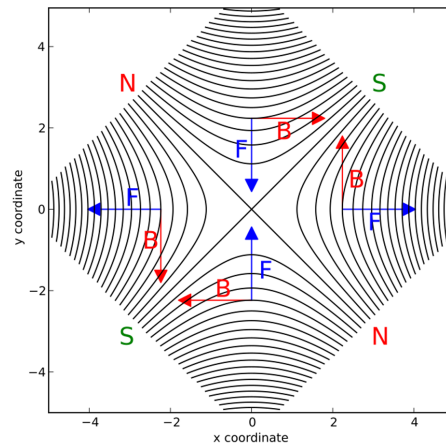


Figure 2.8

An example of a QD magnet, i.e. focusing in the vertical direction and defocusing in the horizontal direction for a positively charged particle going into the figure plane. If the poles were switched from north to south and vice-versa, then the horizontal axis would become the defocusing one and the vertical axis would become the focusing one obtaining a QF magnet.

A quadrupole magnet works for a particle exactly like a thin lens works for light.

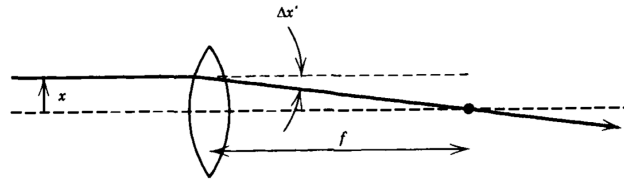


Figure 2.9

Scheme of how a ray initially parallel to the optical axis is bent by a convex lens.

The focal length of a quadrupole magnet can be obtained easily by considering a particle which is moving through the device at a distance  $x$  from the horizontal axis of symmetry, as shown in Figure 2.10.

The quadrupole field is directed along the vertical axis and its magnitude is:

$$B_y = \frac{\partial B_y}{\partial x} x \quad (2.42)$$

If the length of the quadrupole magnet  $l$  is short enough that the displacement  $x$  is unaltered as the particle passes through the device, then the magnetic field experienced by the particle is constant along the particle trajectory. In this approximation, the angle  $\theta$  is equal to the slope of the particle trajectory  $x'$ .

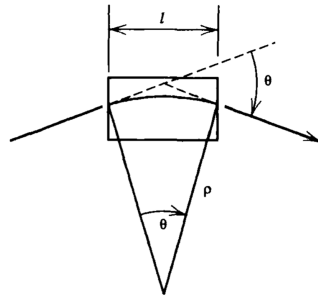


Figure 2.10

Scheme of how a particle is deflected by a quadrupole magnet.

As depicted in Figure 2.10, the slope of the particle trajectory is altered by an amount:

$$\Delta x' = -\frac{l}{\rho} = -l \frac{q}{p} B_y = -l \frac{q}{p} \frac{\partial B_y}{\partial x} x \quad (2.43)$$

where equations (2.40) and (2.42) have been used.

According to Figure 2.9, the change in slope is:

$$\Delta x' = -\frac{l}{f} \quad (2.44)$$

So, by equating equations (2.43) and (2.44):

$$\frac{1}{f} = l \frac{q}{p} \frac{\partial B_y}{\partial x} \quad (2.45)$$

Equation (2.43) can be written in a matrix form as:

$$\begin{pmatrix} x \\ x' \end{pmatrix}_{final} = \begin{pmatrix} 1 & 0 \\ -\frac{1}{f} & 0 \end{pmatrix} \begin{pmatrix} x \\ x' \end{pmatrix}_{initial} \quad (2.46)$$

A QF magnet behaves like a convex lens. On the other hand, in the case of a concave lens the focal length is of opposite sign and this well describes the behaviour of a QD magnet.

Just like how two lenses, one convex and one concave, can be placed at a certain distance from each other to have a net focusing effect, a similar approach can be adopted with quadrupole magnets.

If a QF magnet and a QD magnet are placed immediately next to each other, then their fields completely cancel out; but if there is a space between them whose length has been correctly chosen, then combining two quadrupole magnets with different focusing power in a proper way it is possible to obtain a total focusing effect in both horizontal and vertical directions.

Such a pair of quadrupole magnet forms the so-called FODO cell shown in Figure 2.11. Typically, the space between the two quadrupole magnets is occupied by a dipole magnet.

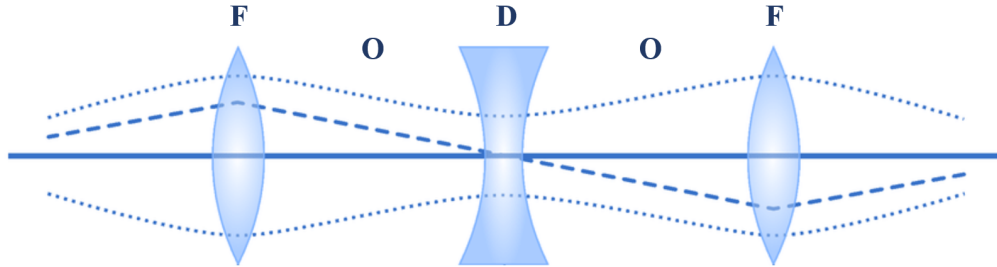


Figure 2.11

Schematic representation of a FODO cell: it consists of a QF magnet (F), a drift (O), a QD magnet (D) and a drift (O). The dotted lines represent the envelope, while the dashed line the particle trajectory.

### 2.2.5 Courant-Snyder phase space ellipse

The Hill's differential equations are summarized in equation (2.25).

A storage ring is characterized by the fact that the magnet strength parameter  $K(s)$  is periodic and the periodicity is given by:

$$K(s+L) = K(s) \quad (2.47)$$

where  $L$  is the storage ring circumference.

As a result, it is possible to write a general solution for equation (2.25):

$$u = \sqrt{\varepsilon} \sqrt{\beta_u(s)} \cos[\psi_u(s) + \phi] \quad (2.48)$$

where  $\varepsilon$  is the single-particle emittance,  $\beta(s)$  is the betatron function,  $\psi(s)$  is the phase function and  $\phi$  is an arbitrary phase offset.

It describes how a particle moves about the reference orbit, i.e. its betatron oscillations. This motion is called betatron motion.

The  $\beta$  function modulates the amplitude of betatron oscillations. It is positive and periodic with the same periodicity of the magnet strength parameter. It is solely determined from the structure of the magnetic lattice and describes the focusing power of quadrupole magnets: its maxima and minima correspond to focusing and defocusing quadrupole magnets respectively as shown in Figure 2.12.

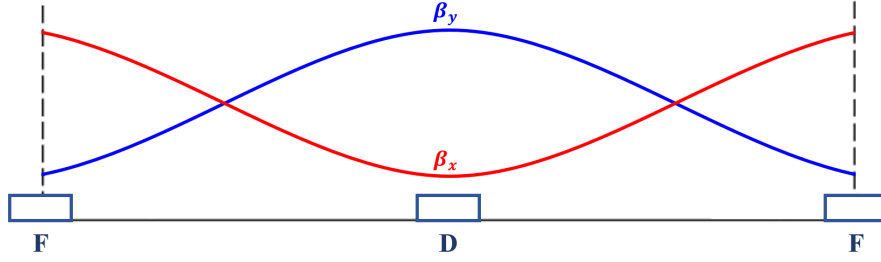


Figure 2.12

Representation of the behaviour of the  $\beta$  function within a FODO cell.

The  $\psi$  function is related to the  $\beta$  function through the following equation:

$$\psi_u(s) = \int \frac{1}{\beta_u(s)} ds \quad (2.49)$$

The number of betatron oscillations per turn is called betatron tune and is defined as:

$$Q_u = \frac{1}{2\pi} \psi_u(L) = \frac{1}{2\pi} \int \frac{1}{\beta_u(s)} ds \quad (2.50)$$

It is one of the most important parameter. It can be modified by changing the strength of the quadrupole magnets.

It is useful to define other two new variables that together with the  $\beta$  function compose the Courant-Snyder or Twiss parameters:

$$\alpha = -\frac{1}{2} \frac{d\beta}{ds} \quad (2.51)$$

$$\gamma = \frac{1 + \alpha^2}{\beta} \quad (2.52)$$

By using these parameters, it is possible to rewrite equation (2.25) as:

$$\gamma u^2 + 2\alpha u u' + \beta u'^2 = \varepsilon \quad (2.53)$$

This equation describes the so-called Courant-Snyder ellipse in the phase space. Its eccentricity and the tilt form and orientation depend on the Courant-Snyder parameters, while its area is constant and given by:

$$A = \pi \varepsilon \quad (2.54)$$

The emittance  $\varepsilon$  is also known as the Courant-Snyder invariant and it is used to characterize the cross-sectional size of the particle beam in the transverse and vertical planes.

For each position  $s$  along the circular closed path there is an ellipse in the phase space  $(u, u')$  that describes the motion of the particles of the beam.

A typical Courant-Snyder ellipse in the phase space is shown in Figure 2.13.

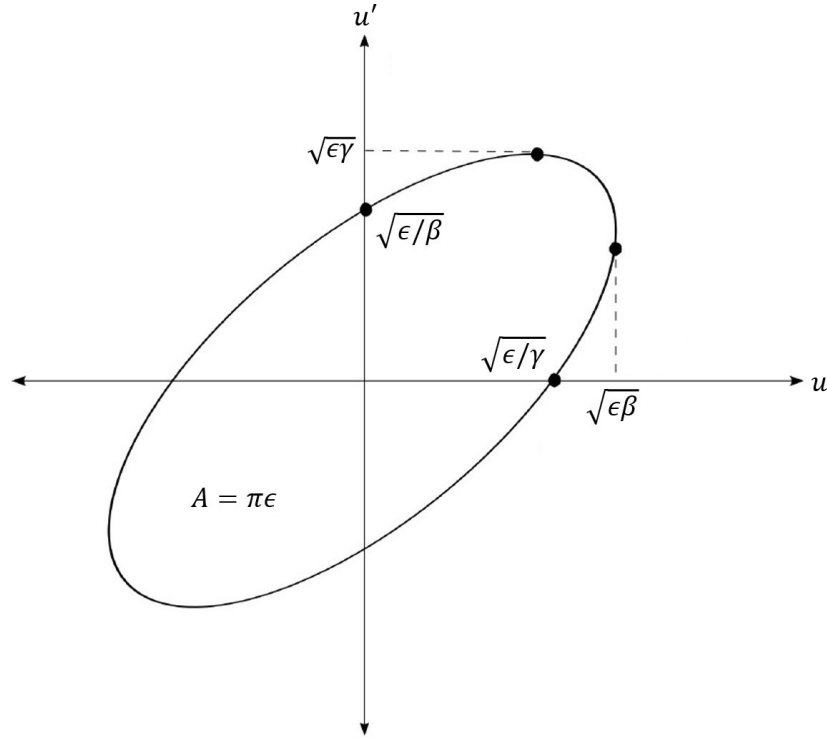


Figure 2.13

Representation of a typical Courant-Snyder ellipse in the phase space.

### 2.2.6 Off-momentum particles: dispersion e chromaticity effects

Up to now, particles with the same momentum  $p_0$  as the reference particle have been considered; actually, each particle is characterized by its own momentum  $p$  and, as a result, subjected to betatron oscillations.

An off-momentum particle is characterized by a momentum offset defined as:

$$\delta = \frac{p - p_0}{p_0} = \frac{\Delta p}{p_0} \quad (2.55)$$

The momentum spread results in a non-homogeneous Hill's differential equation:

$$u''(s) + K(s)u(s) = K(s)\delta u \quad (2.56)$$



whose solution is:

$$u = \sqrt{\varepsilon} \sqrt{\beta_u(s)} \cos[\psi_u(s) + \phi] + D_u(p, s) \delta \quad (2.57)$$

where  $D(p, s)$  is the dispersion function.

In addition, the quadrupole magnets have the property that their focusing strength depends on the particle momentum ( $B\rho \propto p$ ). As well as in optics rays with different wavelengths find a different refraction index in a lens and experience a different focal length, similarly in a storage ring particles with different momenta feel a different focusing strength in a quadrupole magnet and have a different betatron oscillation frequency.

The tendency for off-momentum particles to have different values for the betatron tunes is described by chromaticity. In other words, the dependence of focusing on momentum causes the dependence of the betatron tune on momentum too and chromaticity quantifies their relation:

$$\Delta Q_u = \xi_u \delta \quad (2.58)$$

where  $\Delta Q$  is the change in the betatron tune and  $\xi$  is the chromaticity.

In order to correct the chromaticity effects, a distribution of sextupole magnets is normally used.

### 2.2.7 Sextupole magnets

A sextupole magnet consists of six magnetic poles set out in an alternating fashion around the particle beam, as shown in Figure 2.14.



Figure 2.14  
Image of a sextupole magnet.

The chromaticity effects are seen at the ends of quadrupole magnets and cannot be corrected by the quadrupole magnets themselves. Typically they are controlled with the addition of sextupole magnets.

In the analysis of the effects of the magnetic field as the superposition of different components, to include the sextupole component the 2<sup>nd</sup> order terms in the magnetic field expansion given by equation (2.19) must be considered. The magnetic field in the horizontal and vertical directions become respectively:

$$B_x = \frac{\partial B_x}{\partial y}y + \frac{1}{2} \frac{\partial^2 B_x}{\partial y^2}y^2 + \frac{\partial^2 B_x}{\partial x \partial y}xy \quad (2.59)$$

$$B_y = B_y(0,0) + \frac{\partial B_y}{\partial x}x + \frac{1}{2} \frac{\partial^2 B_y}{\partial x^2}x^2 + \frac{\partial^2 B_y}{\partial x \partial y}xy \quad (2.60)$$

From these equations, it is clear that the sextupole field is non-linear and the motion in the horizontal and vertical directions are coupled. By assuming the horizontal and vertical motions as decoupled, the sextupole fields varies with the second order of the radial distance from the longitudinal axis, as shown in Figure 2.15.

By assuming the horizontal and vertical motions as decoupled, the sextupole fields varies with the second order of the radial distance from the longitudinal axis, as shown in Figure 2.15.

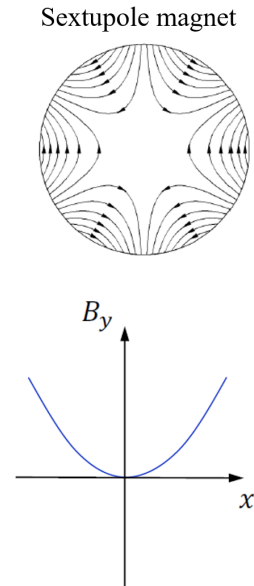


Figure 2.15  
Representation of the sextupole magnetic fields.

However, the quadrature dependence can lead to particles with a high position offset being kicked far from the beam axis and lost. As a result, the addition of sextupole magnets can limit acceptance of the accelerator.

## 2.3 Longitudinal beam dynamics

As studied in the previous sections, the peculiar characteristic of the transverse fields is that they allow to guide and focus the particle beam providing beam guidance and focusing. However, they do not contribute to the energy of the particles through acceleration.

For particle acceleration, fields with a non-vanishing component in the direction of the acceleration, i.e. the longitudinal direction, are needed; such fields are called longitudinal fields or accelerating fields.

The longitudinal beam dynamics describes the evolution of particle trajectories under the influence of longitudinal fields. The longitudinal deviations are called synchrotron oscillations. While magnetic fields are used to guide and focus the particles, the application of electric fields is to accelerate particles. The most common and efficient way to provide particle acceleration to high energies is to use high frequency oscillating electric fields.

### 2.3.1 Radiofrequency cavities

The accelerating structure involved in the acceleration of particles is the resonant cavity. The name *cavity* deals with the structure of the device: it consists of a series of cylindrical poles which act as electrodes held at a high voltage with cavities in between, as shown in Figure 2.16. This specific design allows to create a strong electric field in the longitudinal direction.

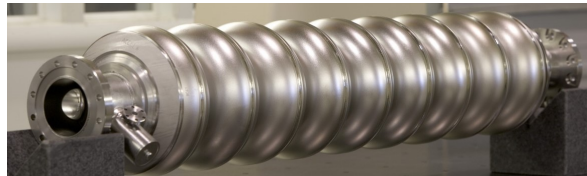


Figure 2.16  
Image of a RF cavity.

It is also called radiofrequency (RF) cavity because the voltage applied is a RF oscillating voltage:

$$V_{RF} = V_0 \sin(\omega_{RF} t) \quad (2.61)$$

where  $V_0$  is the voltage amplitude and  $\omega_{RF}$  is the voltage angular frequency.

As a result, an RF oscillating electric field is generated:

$$\vec{E}_{RF} = E_0 \sin(\omega_{RF} t) \hat{z} \quad (2.62)$$

where  $E_0$  is the electric field amplitude.

In the case of a storage ring, typically a single RF cavity is used, but the energy increases linearly with the number of passages through it.

### 2.3.2 Phase stability principle

The fact that each particle is characterized by its own momentum  $p$  induces effects not only in the horizontal and vertical directions, but also in the longitudinal one where off-momentum particles are subjected to synchrotron oscillations.

The reference particle, characterized by velocity  $v_0$  and momentum  $p_0$ , has exactly the right time of passage through the RF cavity and, so, does not gain or lose energy. However, a generic particle of the beam does and the energy gained/lost per passage through the RF cavity is given by:

$$\varepsilon = qV \sin\phi_n \quad (2.63)$$

where  $q$  is the particle electric charge,  $V$  is the effective potential felt by the particle and  $\phi_n$  is the phase angle.

The principle which ensures the stability of the longitudinal motion is the phase stability.

The revolution period of a generic particle is:

$$\tau = \frac{L}{v} \quad (2.64)$$

where  $L$  is the storage ring circumference and  $v$  is the particle velocity.

The fractional change in the revolution period associated with the fractional changes in the path length and in the velocity is:

$$\frac{\Delta\tau}{\tau} = \frac{\Delta L}{L} - \frac{\Delta v}{v_0} \quad (2.65)$$

The terms on the right-hand side of equation (2.65) can be expressed in terms of the momentum offset:

$$\frac{\Delta L}{L} = \alpha_c \delta \quad (2.66)$$

$$\frac{\Delta v}{v_0} = \frac{1}{\gamma^2} \delta \quad (2.67)$$

where in the first equation  $\alpha_c$  is the momentum compaction factor which gives information about the rate of change of the path length with momentum offset and whose value depends on the storage ring design and in the second one  $\gamma$  is the relativistic factor.

Finally, the fractional change in the revolution period can be expressed as:

$$\frac{\Delta\tau}{\tau} = \left( \alpha_c - \frac{1}{\gamma^2} \right) \delta = \eta \delta \quad (2.68)$$

where  $\eta$  is the slip factor which gives information about the rate of change of the travel time with momentum.

The slip factor changes sign at a particular energy called transition energy and defined as:

$$\varepsilon_t = \gamma_t m c^2 \quad (2.69)$$

where  $\gamma_t = (\alpha_c)^{-1/2}$  is the transition factor.

Typically, the operation mode is the normal regime, i.e. below the transition energy ( $\eta < 0$ ). Equivalently, the equation (2.69) can be written as:

$$\frac{\Delta f}{f_0} = \eta \delta \quad (2.70)$$

where  $f_0$  is the reference particle revolution frequency and  $\Delta f/f_0$  the fractional change in the revolution frequency.

Equation (2.70) is the key to understanding the concept of phase stability.

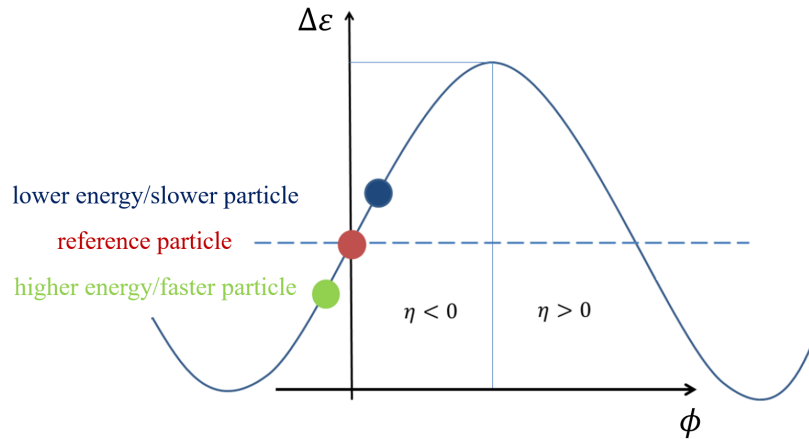


Figure 2.17

Visual representation of the phase stability principle.

In the normal regime, a higher energy/faster particle (the green particle in Figure 2.17) is characterized by  $\delta > 0$  and, as a result, has a higher revolution frequency and arrives at the RF cavity before the reference particle (the red particle in Figure 2.17) losing energy and slowing down; this the reason why in Figure 2.17 it is drawn behind the reference particle.

On the other hand, a lower energy/slower particle (the blue particle in Figure 2.17) is characterized by  $\delta < 0$ , has a lower revolution frequency, arrives at the RF cavity after the reference particle and gains energy undergoing an acceleration and overtaking the reference particle. This process provides the stability of the longitudinal motion.

Above the transition energy ( $\eta > 0$ ), the situation is inverted.

### 2.3.3 Synchrotron equations of motion

From the phase stability principle, the synchrotron equations of motion can be derived.

The motion of a generic particle of the beam with arbitrary energy  $\varepsilon$  and phase angle  $\phi$  with respect to the motion of the reference particle is described by two equations: the former for the energy, while the latter for the phase angle. By considering the situation in Figure 2.18, the synchrotron equations of motion are:

$$\Delta\varepsilon_{n+1} = \Delta\varepsilon_n + qV(\sin\phi_n - \sin\phi_r) \quad (2.71)$$

$$\phi_{n+1} = \phi_n + \frac{\omega_{RF} \tau \eta}{\beta^2 \varepsilon_r} \Delta\varepsilon_{n+1} \quad (2.72)$$

where the subscripts  $n$  and  $n + 1$  refer to the two consecutive passages of the particle through the RF cavity, the subscript  $r$  refers to the reference particle,  $\Delta\varepsilon = \varepsilon - \varepsilon_r$  and  $\beta$  is the particle velocity.

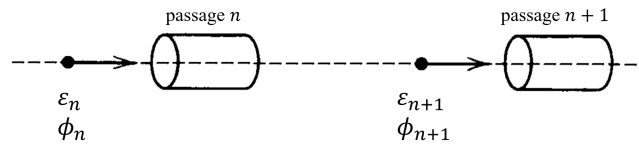


Figure 2.18

Schematic representation of two consecutive passages of a particle through the RF cavity.

Figure 2.19 shows three passages through the RF cavity in the  $\Delta\varepsilon - \phi$  phase space both in the case of zero (left plot) and non-zero acceleration (right plot).

In the left plot, the red particle is the reference particle. The closest particles to the reference particle, the yellow ones, are subjected to oscillations, but remain close to the reference particle turn by turn, revealing a stable oscillation pattern. Differently, the farthest particles, the purple ones, are departing the neighbourhood of the reference particle. The result is the existence of two regions: one is characterized by a stable motion and the other by an unstable motion. The boundary between the stable and unstable regions is called separatrix. The area within the separatrix is called bucket and the collection of particle sharing a bucket is called bunch.

In the case of no acceleration, the buckets are said to be stationary. On the other hand, the right plot shows three accelerating buckets.

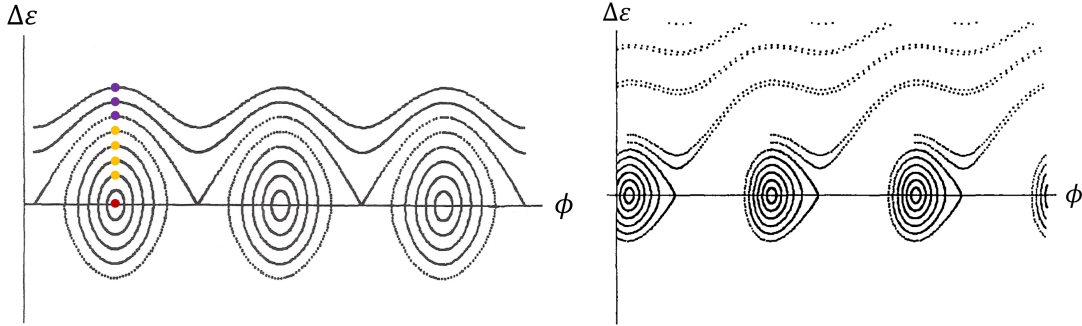


Figure 2.19

Representation of three passages through the RF cavity in the  $\Delta\epsilon - \phi$  phase space both in the case of zero (on the left) and non-zero acceleration (on the right).

The two synchrotron equations of motion can be turned into one differential equation of the second order provided that turn number  $n$  is an independent variable and  $\Delta\phi = \phi - \phi_r$  is small:

$$\frac{d^2\Delta\phi}{dn^2} + (2\pi\nu_s)^2\Delta\phi \quad (2.73)$$

where  $\nu_s$  is the synchrotron tune.

It is defined as the number of synchrotron oscillations per turn and is given by:

$$\nu_s = \sqrt{-\frac{\omega_{RF}\tau qV\eta\cos\phi_r}{4\pi^2\beta^2\epsilon_r}} \quad (2.74)$$

Typically, the frequency of synchrotron oscillations is much smaller than that of betatron oscillations.

The stability of the longitudinal motion is guaranteed when the synchrotron frequency is a real number and this can only occur if:

$$\eta\cos\phi_r < 0 \quad (2.75)$$

This is the stability condition.

In the case of no acceleration,  $\cos\phi_r = 0$  and the stability condition is satisfied when the slip factor is negative.

On the other hand, if the transition energy is crossed during the acceleration cycle, then the slip factor changes sign and the entire phase space must shift forward by an angle of  $\pi$  to maintain phase stability.

### 2.3.4 Matrix formalism

After the explanation of how the motion of the particles occurs in the longitudinal direction, also the solutions to the synchrotron equations of motion can be expressed using the matrix formalism:

$$\begin{pmatrix} z(s) \\ z'(s) \end{pmatrix} = M \begin{pmatrix} z_0(s) \\ z'_0(s) \end{pmatrix} = \begin{pmatrix} \cos(\omega_s t) & \frac{1}{\omega_s} \sin(\omega_s t) \\ -\omega_s \cos(\omega_s t) & \cos(\omega_s t) \end{pmatrix} \begin{pmatrix} z_0(s) \\ z'_0(s) \end{pmatrix} \quad (2.76)$$

where  $\omega_s$  is the synchrotron frequency.

Its unit of measure is  $[s^{-1}]$ . It is possible to express the synchrotron frequency in the more familiar unit of measure ( $[s^{-1}]$ ), dividing it by the factor  $k = \nu L \eta_0$ , where  $\nu$  ( $[s^{-1}]$ ) is the revolution frequency,  $L$  ( $[m]$ ) is the storage ring circumference and  $\eta_0$  is the 1<sup>st</sup> order slip factor (dimensionless).

## 2.4 Spin dynamics

After having explained the particle motion, the spin motion must also be understood because they are closely linked.

### 2.4.1 Principle of the EDM measurement

As mentioned in the previous sections, the motion of the particle beam is regulated by both magnetic and electric fields which provide beam guidance and focusing and beam acceleration respectively.

These fields also determine the evolution of the spins of the particles because they introduce a spin precession through their interactions with the MDM and EDM respectively.

Just as a reminder, the expressions of the MDM and EDM are respectively:

$$\vec{\mu} = \frac{g}{2} \frac{q}{m} \vec{S} \quad (2.77)$$

$$\vec{d} = \frac{\eta}{2} \frac{q}{m} \vec{S} \quad (2.78)$$

where  $q$  is the particle electric charge,  $m$  is the particle mass,  $\vec{S}$  is the particle spin,  $g$  is the gyro-magnetic or Lande factor and  $\eta$  is the gyro-electric factor.



The MDM of a particle at rest under the influence of an external magnetic field  $\vec{B}$  precesses around the field; in other words, the field applies a torque on the particle given by:

$$\frac{d\vec{S}}{dt} = \vec{\mu} \times \vec{B} \quad (2.79)$$

Since the MDM is aligned to the spin, as a result the spin rotates around the field axis. Similarly the EDM of a particle interacts with an external electric field  $\vec{E}$ :

$$\frac{d\vec{S}}{dt} = \vec{d} \times \vec{E} \quad (2.80)$$

By considering both the effects:

$$\frac{d\vec{S}}{dt} = \vec{\mu} \times \vec{B} + \vec{d} \times \vec{E} = \frac{q}{2m}(g\vec{B} + \eta\vec{E}) \times \vec{S} = (\vec{\Omega}_{MDM} + \vec{\Omega}_{EDM}) \times \vec{S} = \vec{\Omega} \times \vec{S} \quad (2.81)$$

where equations (2.77) and (2.78) have been used,  $\vec{\Omega}_{MDM}$  is the precession frequency which describes the contribution of the MDM and  $\vec{\Omega}_{EDM}$  is the precession frequency which describes the contribution of the EDM.

As a result, the MDM contribution to the spin precession is to rotate the particle spin in the ring plane, while the EDM contribution to the spin precession is to rotate the particle spin in the vertical plane. The axis about which the spin rotates due to effects of both the magnetic and electric fields is called invariant spin axis.

Through the horizontal rotation of the spin due to the MDM contribution, the magnetic and electric fields cause the spin to rotate upwards in one revolution and downwards in another and vice versa. Thus, on average, no signal is obtained from the vertical rotation of the spin due to EDM contribution.

A direct signal due to EDM contribution can be detected only if the rotation in the ring plane vanishes, i.e. if the precession frequency due to the MDM contribution vanishes:

$$\vec{\Omega}_{MDM} = 0 \quad \rightarrow \quad \frac{d\vec{S}}{dt} = \vec{\Omega}_{EDM} \times \vec{S} = \vec{d} \times \vec{E} \quad (2.82)$$

This condition is called frozen spin condition. To impose the frozen spin condition means to align the particle spin with its momentum freezing the spin precession in the ring plane.

The frozen spin condition can be achieved in different ways depending on the “nature” of the storage ring. This issue will be clarified in the next sections.

Up to now one single particle has been considered to simplify the considerations about the spin evolution. Actually a particle beam must be considered.

The measurable quantity connected to the spin orientation of a particle beam is the polarization. The polarization vector is defined as:

$$\vec{P} = \frac{1}{N} \sum_{i=1}^N \vec{S}_i \quad (2.83)$$

where  $N$  is the beam total number of particles and  $S_i$  is the spin of  $i$ th particle of the beam. Starting from a longitudinally polarized particle beam, the EDM signal can be detected as the rotation of the polarization vector under the frozen spin condition from the ring plane to the vertical axis due to its interaction with an external radial electric field according to:

$$\frac{d\vec{S}}{dt} = \vec{d} \times \vec{E} \quad (2.84)$$

This is the signature of the EDM signal and can be revealed with the help of a polarimeter, as shown in Figure 2.20.

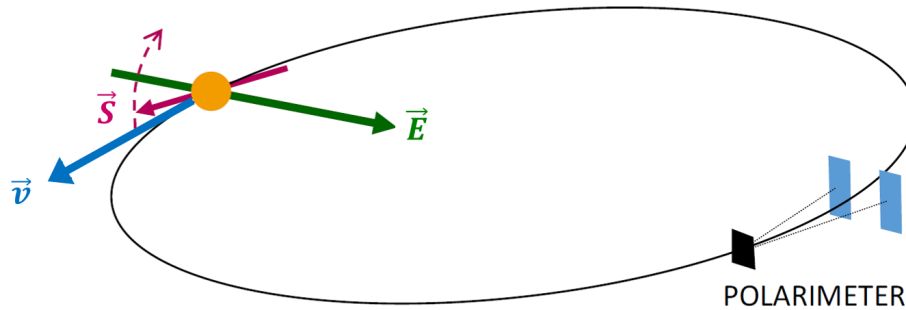


Figure 2.20  
Representation of the principle of the EDM measurement in a storage ring.

## 2.4.2 Thomas-BMT equation

Equation (2.81) describes the evolution of the spin in the centre of mass (CM) system but cannot be used in the case of a storage ring.

To derive the equation which describes the spin evolution in the laboratory frame a realistic case is considered: a particle with the velocity directed along the longitudinal axis is injected into a storage ring where the magnetic and electric fields are respectively vertically and horizontally orientated; in relation to Figure 2.2,  $\vec{B} = B\hat{y}$ ,  $\vec{E} = E\hat{x}$  and  $\vec{v} = v\hat{z}$ .

By using natural units ( $c = 1$ ), the appropriate transformations of the fields lead to the Thomas-Bergmann-Michel-Telegdi (BMT) equation:

$$\begin{aligned} \frac{d\vec{S}}{dt} = & -\frac{q}{m} \left[ \left( G + \frac{1}{\gamma} \right) \vec{B} - \frac{G\gamma}{\gamma+1} \left( \frac{\vec{v} \cdot \vec{B}}{c^2} \right) \vec{v} - \left( G + \frac{1}{\gamma+1} \right) \vec{v} \times \vec{E} + \right. \\ & \left. + \frac{\eta}{2} \left( \vec{E} - \frac{\gamma}{\gamma+1} \left( \frac{\vec{v} \cdot \vec{E}}{c^2} \right) \vec{v} + \vec{v} \times \vec{B} \right) \right] \times \vec{S} \end{aligned} \quad (2.85)$$

Since the magnetic and electric fields are perpendicular to the particle ( $\vec{v} \cdot \vec{B} = \vec{v} \cdot \vec{E} = 0$ ), equation (2.84) reduces to:

$$\frac{d\vec{S}}{dt} = -\frac{q}{m} \left[ \left( G + \frac{1}{\gamma} \right) \vec{B} - \left( G + \frac{1}{\gamma+1} \right) \vec{v} \times \vec{E} + \frac{\eta}{2} \left( \vec{E} + \vec{v} \times \vec{B} \right) \right] \times \vec{S} \quad (2.86)$$

From this equation, the precession frequencies due to the MDM and EDM contributions can be immediately derived:

$$\vec{\Omega}_{MDM} = -\frac{q}{m} \left[ \left( G + \frac{1}{\gamma} \right) \vec{B} - \left( G + \frac{1}{\gamma+1} \right) \vec{v} \times \vec{E} \right] \quad (2.87)$$

$$\vec{\Omega}_{EDM} = -\frac{q}{m} \frac{\eta}{2} \left( \vec{E} + \vec{v} \times \vec{B} \right) \quad (2.88)$$

where  $G$  is the gyro-magnetic anomaly.

It is defined as:

$$G = \frac{g-2}{2} \quad (2.89)$$

It is useful to express the precession frequency with respect to the particle momentum.

The frequency of rotation of the particle momentum is:

$$\vec{\Omega}_p = -\frac{q}{\gamma m} \left[ \vec{B} - \frac{\vec{v} \times \vec{E}}{v^2} \right] \quad (2.90)$$

This equation modifies the precession frequency due to the MDM contribution:

$$[\vec{\Omega}_{MDM}]_{rel} = \vec{\Omega}_{MDM} - \vec{\Omega}_p = -\frac{q}{m} \left[ G\vec{B} - \left( G - \frac{1}{\gamma^2 - 1} \right) \vec{v} \times \vec{E} \right] \quad (2.91)$$

As a result:

$$\begin{aligned}\frac{d\vec{S}}{dt} &= ([\vec{\Omega}_{MDM}]_{rel} + \vec{\Omega}_{EDM}) \times \vec{S} = \\ &= -\frac{q}{m} \left[ G\vec{B} - \left( G - \frac{1}{\gamma^2 - 1} \right) \vec{v} \times \vec{E} + \frac{\eta}{2} (\vec{E} + \vec{v} \times \vec{B}) \right] \times \vec{S}\end{aligned}\quad (2.92)$$

### 2.4.3 Frozen spin condition

As mentioned in the previous section, the criterion to fulfil for a direct measurement of the EDM is the frozen spin condition which is given by:

$$[\vec{\Omega}_{MDM}]_{rel} = -\frac{q}{m} \left[ G\vec{B} - \left( G - \frac{1}{\gamma^2 - 1} \right) \vec{v} \times \vec{E} \right] = 0 \quad (2.93)$$

Depending on the configuration of the storage ring fields, this condition can be differently achieved.

#### ■ PURE MAGNETIC STORAGE RING

A pure magnetic storage ring uses only magnetic fields to confine the particles.

In the absence of electric fields, the Thomas-BMT equation given by equation (2.92) reduces to:

$$\frac{d\vec{S}}{dt} = -\frac{q}{m} \left[ G\vec{B} + \frac{\eta}{2} \vec{v} \times \vec{B} \right] \times \vec{S} \quad (2.94)$$

It is not possible to satisfy the frozen spin condition in the presence of a pure magnetic confinement system because the frozen spin condition would reduce to:

$$[\vec{\Omega}_{MDM}]_{rel} = -\frac{q}{m} G\vec{B} = 0 \quad (2.95)$$

and would be satisfied only for a null magnetic field, but a magnetic field is always needed to keep particles inside the storage ring.

#### ■ COMBINED-FIELD STORAGE RING

A combined-field storage ring uses both magnetic fields for particle confinement.

In this case, the Thomas-BMT equation does not suffered any changes and it is exactly given by equation (2.92).

Differently from a pure magnetic storage ring, the presence of the electric fields allows the frozen spin condition to be satisfied: it can be achieved by combining appropriately the magnetic and electric fields such that equation (2.93) is fulfilled.

For frozen spin particles the Thomas-BMT equation becomes:

$$\frac{d\vec{S}}{dt} = \vec{\Omega}_{EDM} \times \vec{S} \quad (2.96)$$

#### ■ PURE ELECTRIC STORAGE RING

A pure electric storage ring uses only electric fields to confine the particles.

In the absence of magnetic fields, the Thomas-BMT equation reduces to:

$$\frac{d\vec{S}}{dt} = -\frac{q}{m} \left[ \left( G - \frac{1}{\gamma^2 - 1} \right) \vec{v} \times \vec{E} + \frac{\eta}{2} \vec{E} \right] \times \vec{S} \quad (2.97)$$

Differently from a pure magnetic storage ring where the only presence of magnetic fields limits the possibility to fulfil the frozen spin condition, the sole electric fields allows it for particle with positive gyro-magnetic anomalies (e.g., the proton) by setting the particle momentum at a specific value called magic momentum such that:

$$G = \frac{1}{\gamma^2 - 1} \quad (2.98)$$

With this condition, equation (2.93) is fulfilled.

For frozen spin particles the Thomas-BMT equation becomes:

$$\frac{d\vec{S}}{dt} = \vec{d} \times \vec{E} \quad (2.99)$$

### 2.4.4 Critical aspects

The change in the spin tune and the spin coherence time (SCT) are the critical and strictly connected parameters to consider when performing EDM experiments in storage rings.

The longitudinally polarized particle beam injected into the storage ring precedes in the ring plane with a frequency which depends on the experimental setup.

The spin tune is the number of spin precessions around the vertical axis during one turn around the storage ring for a single particle and is defined as:

$$\nu_s = G\gamma \quad (2.100)$$

where  $\gamma$  is the relativistic factor.

It is proportional to the particle velocity through the relativistic factor.

However, particles have different velocities and after some time the spins go out of phase and spread out; this is described by the change in the spin tune which is defined for a single particle as:

$$\Delta\nu_s = G\Delta\gamma \quad (2.101)$$

As a result, the initial longitudinal polarization is lost. The situation is shown in Figure 2.21.

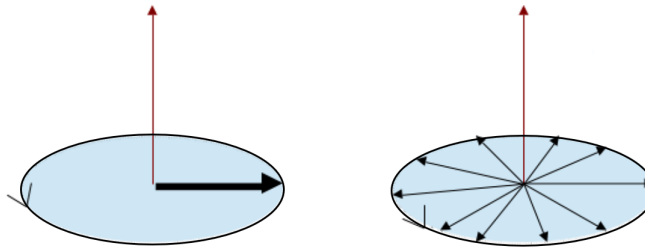


Figure 2.21

Representation of the change in the spin tune: initially all the spins are aligned along the same direction so and the beam is polarized (on the left); then the spins spread out due to different velocities and the polarization is lost.

The polarization lifetime, i.e. the time during which the spins precess coherently maintaining some fraction of their initial polarization, is the SCT. It must be as long as possible since it represents the time available to measure the EDM signal. Since it depends on the change in the spin tune, to obtain a long SCT it is necessary to minimize the change in the spin tune.

## 3

## The JEDI collaboration and experiment at FZ-Jülich

## 3.1 Project overview

The Jülich Electric Dipole moment Investigations (JEDI) collaboration was created in the end of 2011. The aim of this partnership is to carry out a long-term project for the measurement of the proton EDM (pEDM) in a pure electric storage ring.

To reach this goal, a three stages strategy has been proposed as shown in Figure 3.1.


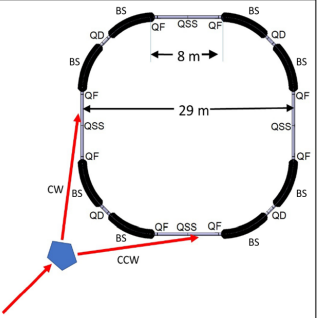
| Stage 1   | Stage 2   | Stage 3   |
|---|---|---|
| COSY  | PSR   | Pure electric storage ring  |
|                          |    | Different design proposals:<br>- all-electric storage ring;<br>- hybrid storage ring;<br>- ...  |
| <ul style="list-style-type: none"> <li>•Studies of feasibility</li> <li>•Measurement of the dEDM</li> </ul> | <ul style="list-style-type: none"> <li>•Study of the critical features</li> <li>•Development of the key technologies</li> <li>•First measurement of the pEDM</li> </ul> | <ul style="list-style-type: none"> <li>•Target precision of <math>10^{-29} e \cdot cm</math></li> <li>•Measurement of the pEDM</li> </ul> |

Figure 3.1

Table with some specifics of the staged approach pursued by the JEDI collaboration for the pEDM measurement.

The 1<sup>st</sup> stage consists in exploiting an already existing facility to demonstrate the feasibility of a pure electric storage ring. The chosen one was the COoler SYnchrotron (COSY).

For the 2<sup>nd</sup> stage a new facility must be designed, built and activated to study the critical features and to develop the key technologies required for the future measurements. This facility is called Prototype Storage Ring (PSR).

The 3<sup>rd</sup> and final stage is the construction and operation of a pure electric storage ring. It will be a larger version of the PSR ring. This ring will need all the technologies developed in the previous stages to allow the measurement of the pEDM.

The next sections will provide a short description of the three facilities.

## 3.2 Staged approach

### 3.2.1 Precursor stage: COSY

The COSY represented the ideal existing storage ring for the feasibility studies of the pure electric storage ring.

The COSY complex is located at the ForschungsZentrum-Jülich (FZ-Jülich) in Germany and consists into three main parts as shown in Figure 3.2: the ion source, the JULIC cyclotron and the COSY.

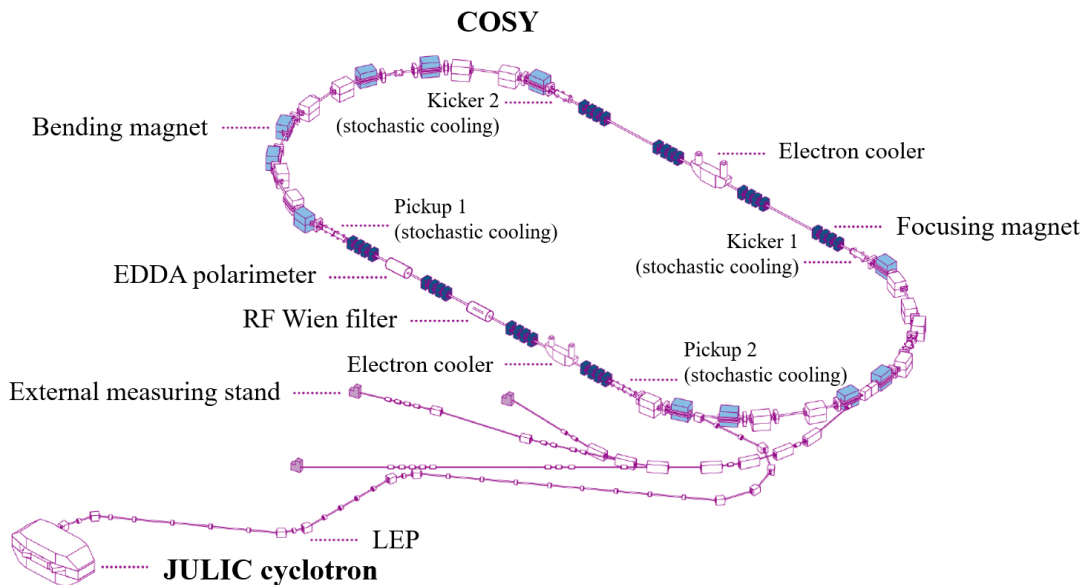


Figure 3.2  
Schematic representation of the COSY complex.

The ion source (not shown in Figure 3.2) provides negatively charged hydrogen ( $H^-$ ) and deuterium ( $D^-$ ) ions which can be either polarized or not.

The selected beam is guided to the JULIC cyclotron where it is accelerated to its injection kinetic energy which is 45 MeV for the  $H^-$  ions and 75 MeV for the  $D^-$  ions.



Once in the cyclotron, a first measurement of the beam polarization is provided by the Low Energy Polarimeter (LEP).

Then the beam is injected into the COSY via a charge-exchange injection system which strips two electrons from each ion resulting in a final beam of positively charged particles which can be either protons or deuterons.

Finally, the beam is accelerated in a momentum range from  $300 \text{ MeV}/c$  to  $3.7 \text{ GeV}/c$  using a single RF cavity located in the middle of one of the straight sections.

The COSY has a circumference of about  $183.4 \text{ m}$  and consists of 2 arcs and 8 straight sections each with a length of  $40 \text{ m}$ .

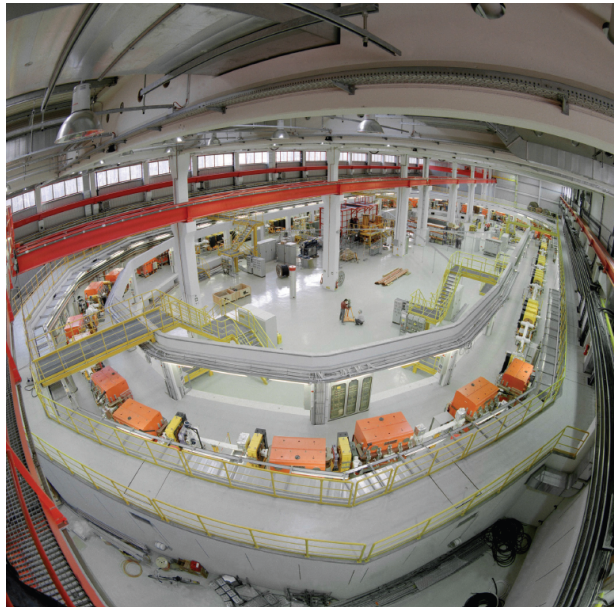


Figure 3.3  
Image of the COSY.

It is a pure magnetic storage ring with dipole and quadrupole magnets to bend and focus the particle beam respectively.

It has 24 dipole magnets characterized by a length of  $40 \text{ cm}$  and a maximum value of the magnetic field of  $1.67 \text{ T}$  and 56 quadrupole magnets which are grouped into families of 4. The quadrupole magnets within a family have the same dimensions and a common power supply. 8 of these families are located in the straight sections and the other 6 in the arcs. In addition, there are 17 sextupole magnets, of which 7 are in the straight sections and 10 in the arcs. For orbit measurements and corrections there are 59 beam position monitors and 41 "steering" dipole magnets.

The COSY partly owns its name to the phase space controlling which is achieved by the beam cooling. Electron and stochastic cooling are available to prepare a monochromatic beam and ensure the lowest possible emittance. There are two electron coolers for phase space cooling at particle momenta up to  $0.6 \text{ GeV}$  and two stochastic cooling mechanisms for those with momenta above  $1.5 \text{ GeV}$ . Furthermore, the installation of vertical and horizontal dampers provides the possibility to stack electron-cooled beams and thus increase the beam intensity up to about  $10^{10}$  stored particles.

Several devices for spin manipulation (e.g. RF Wien filter) are installed into the ring together with polarimeters (e.g. EDDA polarimeter) which were used to measure the vertical and the horizontal beam polarization components as a function of time and to recover an EDM signal.

The primary goal of this series of proof of capability tests was the determination of the deuteron EDM.

The choice of the deuteron instead of the proton was owed to the fact that it has a lower gyro-magnetic anomaly than the proton which can improve precision in the SCT as well as in the invariant spin axis measurement.

For this purpose, a vertically polarized deuteron beam was used. It was injected into the COSY and accelerated up to  $970 \text{ MeV}$ .

An RF solenoid located in one of the arcs was used to rotate the polarization from the vertical axis to the ring plane.

Since the COSY is a pure magnetic storage ring, the frozen spin condition cannot be achieved; as a result, the spins of the particles precess about the invariant spin axis with a frequency of about  $120 \text{ kHz}$  and after a while they spread out due to the different velocities resulting in a null spin coherence.

The impossibility to satisfy the frozen spin condition heavily affects the possibility to perform an EDM measurement.

As explained before, the EDM signal could be detected as the rotation of the polarization vector from the ring plane to the vertical axis due to its interaction with a radial electric field. The one considered was the radial electric field induced by the vertical magnetic field. However, even in the absence of the spin tune spread, the spin precession causes the spins of the particle to be both parallel and antiparallel to the velocities resulting in a vanishing vertical polarization.

A quasi-frozen spin condition was realized using an RF Wien filter which eliminated the spin precession, while a configuration of sextupole magnets was used to eliminate the spin tune spread obtaining a SCT of about  $1000 \text{ s}$ .

Even if in principle such an experiment can directly provide a measurement of the magnitude of the EDM, the concept at the base of these precursor experiments was the determination of the invariant spin axis from which the upper bound for the deuteron EDM can be derived. Among all the possible systematic effects, the chances of magnetic field misalignments were very high and required a careful investigation through simulations since they could affect the orientation of the invariant spin axis.

The experimental results showed a tilt of 1 *mrad* in the radial direction which is equivalent to an EDM of  $10^{-17} e \cdot cm$ .

This result represents the first-ever direct EDM measurement in a storage ring.

Since the pure magnetic storage rings have a lot of limitations, the next step is the planning of a new kind storage ring with a different kind confinement system which will allow to overcome many problems linked to the frozen spin condition and the undesired magnetic fields and tested some technologies which could improve the precision in the EDM measurements.

This is the case of the PSR ring.

### **3.2.2 Proof-of-concept stage: PSR ring**

The PSR ring is the storage ring which will play the role of the intermediate step in order to study the critical features and to develop the key technologies for the pure electric storage ring.

It will be held to account for the following challenges and open issues:

- storage of high intensity beams for a sufficiently long time;
- phase-space beam cooling via electron and stochastic cooling techniques before the injection;
- simultaneous circulation of clockwise (CW) and counter-clockwise (CCW) beams with multiple polarization states;
- polarization measurements for both CW and CCW beams using the same target;
- magnetic shielding to reduce the ambient radial magnetic field.

Since it is only an intermediate step, it is designed to be as inexpensive as possible while consistent with being capable of achieving its goals; this is the reason why it will be much smaller than most accelerators.

The basic layout of the PSR ring is shown in Figure 3.4.

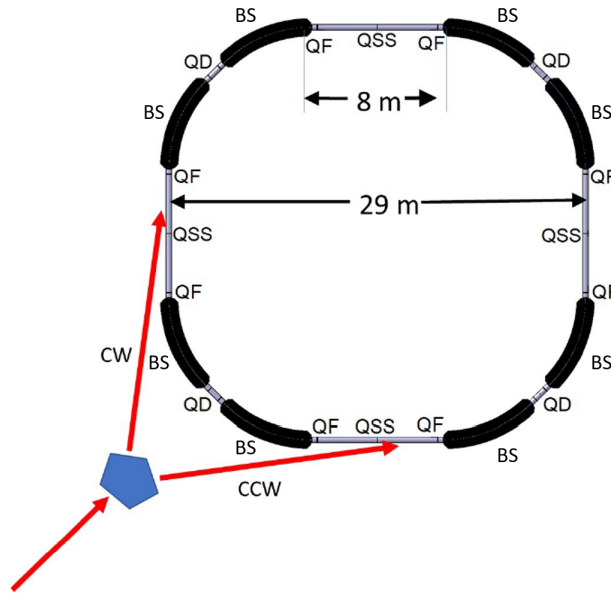


Figure 3.4  
Schematic representation of the PSR basic layout.

It is a 4-fold symmetric "squared" ring with a circumference of about 100 m and a bending radius of 8.861 m.

It consists of 4 arcs characterized by a length at  $45^\circ$  of 15.718 m and 4 straight sections characterized by a length of 8 m.

In each arc there is a unit cell bending  $90^\circ$ . Each unit cell has the following structure:

$$QF - BS - QD - BS - QF$$

where  $QF$  is a focusing quadrupole magnet,  $BS$  is a bending section and  $QD$  is a defocusing quadrupole magnet.

Summing up, there are 16 quadrupole magnets and 8 bending sections.

Actually, the quadrupole magnets can be structured into three families:

- $QD$  → it contains 4 quadrupole magnets which are placed in between the bending sections of each unit cell;
- $QF$  → it contains 8 quadrupole magnets which are placed around the bending sections of each unit cell;
- $QSS$  → it contains 4 quadrupole magnets which are placed in the straight sections in between the unit cells.

Each quadrupole magnet is characterized by a length of 40 *cm*.

A sextupole magnet is placed on top of each quadrupole to correct chromaticity effects right at the place of origin. Also the sextupole magnets form three families which correspond to the quadrupole magnets families and are named similar to the associated quadrupole magnets families they belong to: SXD, SXF and SXSS. They are not shown in Figure 3.4.

Each straight section has the following structure:

$$QF - QSS - QF$$

where *QSS* is a quadrupole which provides further flexibility to adjust the beam optics. The flexibility is one of the goal for the design.

The straight sections house two injection regions for the CW and CCW beams. The injection is done by using switching magnets.

The beams are protons with kinetic energy in the 30 – 45 *MeV* range, bunched into 2, 4, 6 or 8 bunches with vertical polarization, either up or down, in a cooled phase space of  $1 \pi \text{ mm} \cdot \text{mrad}$ .

Each bending section consists of both electric and magnetic elements and this fact allows the PSR ring can operate in two modes: the first one works with electric bending elements only and provides the required rigidity for 30 *MeV* protons, while the second one uses magnetic bends in addition and expands the protons energy up to 45 *MeV*. The electric bending section consists of two electrodes characterized by a length of 6.959 *m* and a spacing of 60 *mm*.

The two operation mode makes it a combined-field storage ring.

Figure 3.5 summarizes the geometry of the storage ring and the magic parameters of the beam.

At the moment the collaboration is performing simulations about the open issues.

### 3.2.3 Final stage: pure electric ring

The pure electric storage ring will be the final stage of the project of the JEDI collaboration with the aim to reach the target precision of  $10^{-29} e \cdot \text{cm}$ .

The main advantages in using a pure electric storage ring are the possibility to improve the statistics increasing the luminosity of the experiment, the simultaneous circulation of two counter-rotating particle beams to properly address and control different sources of systematic errors and the absence of magnetic fields which allows to maximize the precision of the measurement inhibiting one of the main sources of systematic errors.

One of the proposals for the final stage is the hybrid storage ring.

| Geometry of the storage ring   |               |        |                     |                    |
|--------------------------------|---------------|--------|---------------------|--------------------|
| element                        | value         |        |                     | units              |
| circumference                  | 100.473       |        |                     | m                  |
| bending radius                 | 8.861         |        |                     | m                  |
| arc length                     | 15.718        |        |                     | m                  |
| straight section length        | 8.000         |        |                     | m                  |
| quadrupole magnets length      | 40            |        |                     | cm                 |
| electrodes length              | 6.959         |        |                     | m                  |
| electrodes spacing             | 60            |        |                     | mm                 |
| “Magic” parameters of the beam |               |        |                     |                    |
| parameter                      | <i>only E</i> |        | <i>both E and B</i> | units              |
|                                | value         |        |                     |                    |
| G                              | 1.793         |        |                     | /                  |
| mass                           | 938           |        |                     | MeV/c <sup>2</sup> |
| kinetic energy                 | 30            | 30     | 45                  | MeV                |
| momentum                       | 239           | 239    | 294                 | MeV/c              |
| energy                         | 968           | 968    | 983                 | MeV                |
| $\gamma$                       | 1.032         | 1.032  | 1.048               | /                  |
| $\beta$                        | 0.247         | 0.247  | 0.299               | /                  |
| magnetic field strength        | /             | 0.0285 | 0.0327              | T                  |
| electric field strength        | 6.67          | 4.56   | 7.00                | MV/m               |

Figure 3.5  
Table with the geometry and beam parameters of the PSR.

*Hybrid* means that the storage ring features electric bending elements and magnetic focusing elements. Its layout is described in detail in the next section.

### 3.3 Hybrid storage ring

The basic layout of the hybrid storage ring is shown in Figure 3.6.

It is a 24-fold symmetric storage ring with a circumference of about 800 *m*.

It consists of 24 periods. Each period has the following structure:

$$SS - BS - SS - BS$$

where *SS* is a straight section and *BS* is a bending section.

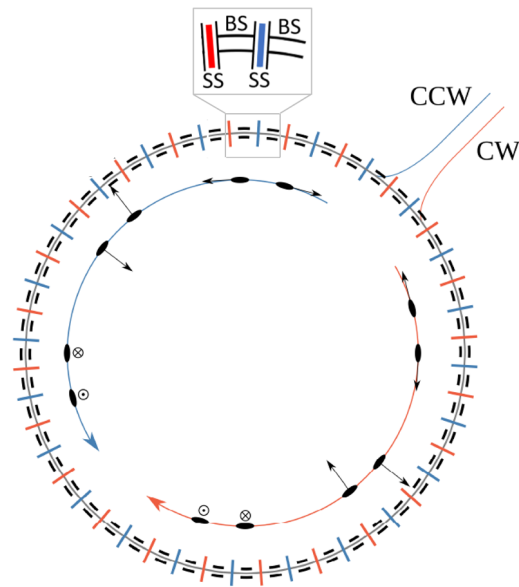


Figure 3.6

Schematic representation of the hybrid storage ring basic layout.

Summing up, there are 48 straight sections characterized by a length of  $4.16\text{ m}$  and 48 bending sections characterized by a length of  $12.5\text{ m}$ . The bending sections together have a circumference of  $600\text{ m}$  with a bending radius of  $95.49\text{ m}$ .

A detailed representation of a single period is shown in Figure 3.7.

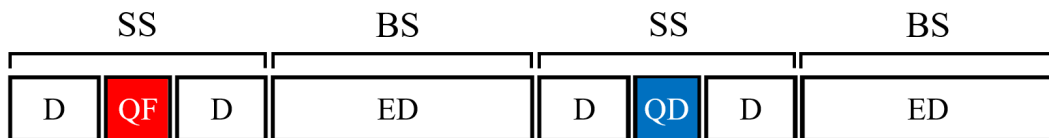


Figure 3.7

Schematic representation of the hybrid storage ring single period: *SS* stands for straight section, *BS* for bending section, *D* for drift, *QF* for focusing quadrupole magnet, *ED* for electric deflector and *QD* for defocusing quadrupole magnet.

In each straight section there is a quadrupole magnet for a total number of 48 quadrupole magnets characterized by a length of  $40\text{ cm}$  and a strength of  $\pm 0.21\text{ T/m}$ , where  $+$  stands for focusing and  $-$  stands for defocusing. The quadrupole magnets are alternated in sign.

On the top of each quadrupole magnet there is a sextupole magnet for a total number of 48 sextupole magnets of which 24 are characterized by a strength  $k_1$  and 24 are characterized by a strength  $k_2$ . Also the sextupole magnets are alternate in sign. They are not shown in Figure 3.6.

Each bending section consists of two electrodes characterized by a height of 20 *cm* and a spacing of 4 *cm* with a field strength of 4.4 *MV/m*.

The straight sections house two injection regions for the CW and CCW beams. The beams are protons with a kinetic energy of 233 MeV with  $1.17 \times 10^8$  particles per bunch.

Figure 3.8 summarizes the geometry of the storage ring and the magic parameters of the beam.

| Geometry of the storage ring   |            |                    |
|--------------------------------|------------|--------------------|
| element                        | value      | units              |
| circumference                  | 800        | m                  |
| bending radius                 | 95.49      | m                  |
| straight section length        | 4.16       | m                  |
| bending section length         | 12.5       | m                  |
| bending section circumference  | 600        | m                  |
| quadrupole magnets length      | 40         | cm                 |
| electrodes length              | 12.5       | m                  |
| electrodes height              | 20         | cm                 |
| electrodes spacing             | 4          | cm                 |
| “Magic” parameters of the beam |            |                    |
| parameter                      | value      | units              |
| G                              | 1.793      | /                  |
| mass                           | 930        | MeV/c <sup>2</sup> |
| momentum                       | 700        | MeV/c              |
| energy                         | 1170       | MeV                |
| $\gamma$                       | 1.248      | /                  |
| $\beta$                        | 0.598      | /                  |
| quadrupole magnets strength    | $\pm 0.21$ | T/m                |
| electric field strength        | 4.4        | MV/m               |

Figure 3.8

Table with the geometry and beam parameters of the hybrid storage ring.



# 4

## Hybrid storage ring beam dynamics simulations

The focus of this thesis is the hybrid storage ring. In particular, specific beam dynamics simulations have been performed on an idealized lattice whose design reflects the one described in the previous chapter.

In the first section the software used to build the lattice, perform the simulations and analyse the data coming from the simulations are described.

The second section illustrates the code used to build the lattice together with the plot of the Twiss parameters as functions of the distance along the storage ring.

The third section justifies the beam dynamics simulations performed, while the fourth and fifth sections contain the results: the first set of simulations concerns the 6D phase space and the  $6 \times 6$  transfer matrix, while the second one deals with the path lengthening.

### 4.1 Bmad and ROOT software

The software used to build the lattice and to perform the simulations is Bmad.

It has been developed at Cornell University's Laboratory for Elementary Particle Physics and has been in use since the middle of the 90s. It is a subroutine library for charged particle tracking in accelerators and storage rings which uses an object-oriented approach and is written in Fortran 2008. It includes dipole and quadrupole magnets and RF cavities which is everything needed to simulate the basic version of a storage ring lattice. In addition, elements can be defined to control the attributes of other elements and allowing for the creation of composite devices. It provides a wide range of routines to do many things and has various tracking algorithms including Runge-Kutta. It can be used to study the dynamics of both single particles and particle beams.

The software used to analyse the data coming from the simulations is ROOT.

Its development was initiated by René Brun and Fons Rademakers at CERN in 1994. It is an object-oriented library written in the C++ programming language. It was originally designed for particle physics data analysis but nowadays it is also used in other applications. It provides a lot of packages.

## 4.2 Lattice

The code used to build the hybrid storage ring lattice is shown in Figures 4.1, 4.2 and 4.3. This is the 1<sup>st</sup> version of the code; it has been implemented into the 2<sup>nd</sup> version to allow the study of the path lengthening.

```

!-----GEOMETRY-----
N.BS      = 48
L.BS      = 12.5

angle     = 2*pi/N.BS
radius    = L.BS/angle

!-----BEAM-----

G         = anom_moment_proton
mass      = m_proton
gamma     = sqrt(1+1/G)
beta      = sqrt(1-1/(gamma*gamma))
momentum  = mass*sqrt(gamma*gamma-1)
energy    = gamma*mass

Bfield    = angle*momentum/(c_light*L.BS)
Efield    = gamma*mass*beta*beta/(radius*((1/(gamma*gamma-1)-G)*(beta*beta/G)+1))
k.Q       = 0.20433

!-----

parameter[geometry]      = closed
parameter[particle]      = proton
parameter[absolute_time_tracking] = .false.
beginning[p0c]           = momentum

```

Figure 4.1

Illustration of the 1<sup>st</sup> block of the code used to build the lattice.

According to Figure 4.1, the 1<sup>st</sup> block of the code defines the geometry of the storage ring. Among all the parameters listed in Figure 3.8, the number of bending sections ( $N.BS$ ) and their length ( $L.BS$ ) are sufficient to fix the geometry since they define the bending angle ( $angle$ ) and radius ( $radius$ ).

The 2<sup>nd</sup> block of the code defines the parameters of the beam under the frozen spin condition in relation to the ones listed in Figure 3.8. Since the confinement system is pure electric, the sole electric field ( $Efield$ ) is used for the particle confinement. The magnetic field ( $Bfield$ ) ensures to have a closed orbit, while the quadrupole magnet strength ( $k.Q$ ) expresses the magnetic field necessary to the particle focusing and defines the working point which is  $(Q_x, Q_y) = (2.699, 2.245)$ .

The 3<sup>rd</sup> block specifies that the orbit is closed, the circulating particles are protons, the time tracking is relative and the initial momentum coincide with the magic one.

```

!-----DEVICES-----
ED: sbend
ED[fringe_type]      = basic_bend
ED[l]                = 1.85
ED[b_field]          = Bfield
ED[b_field_err]      = -Efield/(beta*c_light)
ED[b0_elec]          = -Efield
ED[exact_multipoles] = vertically_pure

D_Q: drift
D_Q[L]               = 1.9

QF: quadrupole
QF[L]                = 0.4
QF[b1_gradient]      = +k.Q

QD: quadrupole
QD[L]                = 0.4
QD[b1_gradient]      = -k.Q

D_RF: drift
D_RF[L]              = 0.45

RF: rfcavity
RF[l]                = 1.0
RF[harmon]           = 1
RF[voltage]          = 1.89e3
RF[phi0]             = 0.5

```

Figure 4.2

Illustration of the 2<sup>nd</sup> block of the code used to build the lattice.

In Figure 4.2 the electric deflectors, the quadrupole magnets and the RF cavity are defined with all their attributes. They are the necessary devices to define the basic layout of a storage ring.

```

!-----LATTICE-----
bending:      line = (ED)
focusing:     line = (D_Q, QF, D_Q)
defocusing:   line = (D_Q, QD, D_Q)
period:       line = (focusing, bending, defocusing, bending)
rf_cavity:    line = (D_RF, RF, D_RF)
focusing_rf:  line = (QF, D_Q)
period_rf:    line = (rf_cavity, focusing_rf, bending, defocusing, bending)
lattice:      line = (period_rf, period, period, period, period, period, period, period, &
                    period, period, period, period, period, period, period, period, &
                    period, period, period, period, period, period, period, period)

!-----
*[tracking_method] = runge_kutta
*[mat6_calc_method] = tracking
RF[tracking_method] = bmad_standard

use, lattice

```

Figure 4.3

Illustration of the 3<sup>rd</sup> block of the code used to build the lattice.

In the 1<sup>st</sup> block of Figure 4.3 the lattice is built according to the layout shown in Figure 3.6, while the 2<sup>nd</sup> block defines the tracking method.

Once built the lattice, Tao is used for its visualization. It is a general purpose simulation program built using Bmad libraries. The lattice is shown in Figure 4.4.

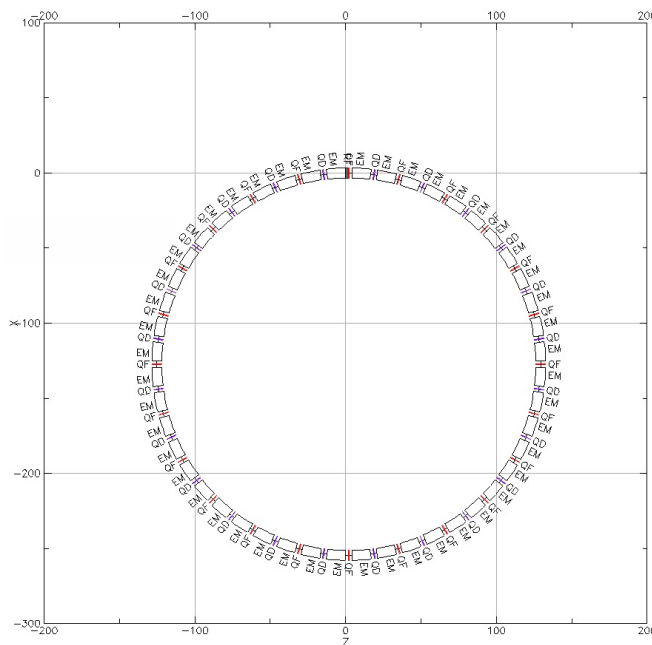


Figure 4.4  
Illustration of the lattice through Tao program.

The Twiss parameters can be measured directly via a dedicated routine in Bmad which produces a file including the Twiss parameters as well as the dispersion function.

Figure 4.5 shows the horizontal and vertical  $\beta$  function and the horizontal dispersion function as functions of the distance along the storage ring.

This plot gives an idea of how the motion of a particle occurs within the storage ring.

### 4.3 Motivation

Objective of the beam dynamics simulations performed is the need to verify whether the current theoretical knowledge about storage rings, which is known to be valid in the case of pure magnetic ones, can also be applied in the case of other types of storage rings, in particular the hybrid storage ring which is characterized by an electric confinement system.

For all the simulations performed the single particle tracking has been considered.

Two aspects have been taken into account: the couplings strengths between different phase spaces through the study of the  $6 \times 6$  transfer matrix and the path lengthening phenomenon.

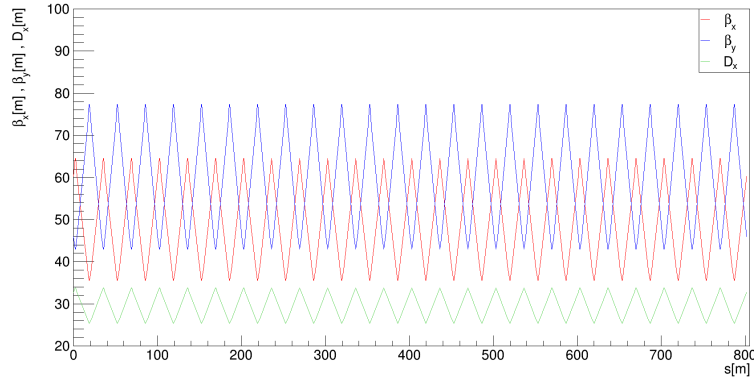


Figure 4.5

Plot of the horizontal (red) and vertical (blue)  $\beta$  function and the horizontal dispersion function (green) as functions of the distance along the storage ring.

## 4.4 6D phase space and $6 \times 6$ transfer matrix

Inside a storage ring a generic particle of the beam is described by a 6-dimensional state vector given by:

$$\begin{pmatrix} x \\ x' \\ y \\ y' \\ z \\ z' \end{pmatrix} \quad (4.1)$$

where, according to Figure 2.2,  $x$ ,  $y$  and  $z$  are the positions in the horizontal, vertical and longitudinal directions respectively and  $x'$ ,  $y'$  and  $z'$  are the corresponding velocities.

As mentioned in chapter 2, the majority of the particles are subjected to betatron and synchrotron oscillations and as a result the 6-dimensional state vector transforms as:

$$\begin{pmatrix} x \\ x' \\ y \\ y' \\ z \\ z' \end{pmatrix}_f = M_{6 \times 6} \begin{pmatrix} x \\ x' \\ y \\ y' \\ z \\ z' \end{pmatrix}_i = \begin{pmatrix} m_{11} & m_{12} & m_{13} & m_{14} & m_{15} & m_{16} \\ m_{21} & m_{22} & m_{23} & m_{24} & m_{25} & m_{26} \\ m_{31} & m_{32} & m_{33} & m_{34} & m_{35} & m_{36} \\ m_{41} & m_{42} & m_{43} & m_{44} & m_{45} & m_{46} \\ m_{51} & m_{52} & m_{53} & m_{54} & m_{55} & m_{56} \\ m_{61} & m_{62} & m_{63} & m_{64} & m_{65} & m_{66} \end{pmatrix} \begin{pmatrix} x \\ x' \\ y \\ y' \\ z \\ z' \end{pmatrix}_i \quad (4.2)$$

where  $M_{6 \times 6}$  is the transfer matrix.

By considering the ideal case of a pure magnetic planar storage ring, the transfer matrix reduces to:

$$M_{6 \times 6} = \begin{pmatrix} m_{11} & m_{12} & 0 & 0 & 0 & m_{16} \\ m_{21} & m_{22} & 0 & 0 & 0 & m_{26} \\ 0 & 0 & m_{33} & m_{34} & 0 & 0 \\ 0 & 0 & m_{43} & m_{44} & 0 & 0 \\ m_{51} & m_{52} & 0 & 0 & m_{55} & m_{56} \\ 0 & 0 & 0 & 0 & m_{65} & m_{66} \end{pmatrix} \quad (4.3)$$

The coloured blocks on the main diagonal are the  $2 \times 2$  transfer matrices for the **horizontal**, **vertical** and **longitudinal** phase spaces respectively. The other two coloured blocks represent the coupling among the different phase spaces.

Explicitly:

$$\begin{cases} x_f = m_{11}x_i + m_{12}x'_i + m_{16}z'_i & (4.4) \end{cases}$$

$$\begin{cases} x'_f = m_{21}x_i + m_{22}x'_i + m_{26}z'_i & (4.5) \end{cases}$$

$$\begin{cases} y_f = m_{33}y_i + m_{34}y'_i & (4.6) \end{cases}$$

$$\begin{cases} y'_f = m_{43}y_i + m_{44}y'_i & (4.7) \end{cases}$$

$$\begin{cases} z_f = m_{51}x_i + m_{52}x'_i + m_{55}z_i + m_{56}z'_i & (4.8) \end{cases}$$

$$\begin{cases} z'_f = m_{65}z_i + m_{66}z'_i & (4.9) \end{cases}$$

The information which can be kept out from this system of equations is the following:

- since the storage ring considered is planar, the horizontal and vertical motions are decoupled and they cannot influence each other; this is the reason why in equations (4.4) and (4.5) there are no vertical terms and in equations (4.6) and (4.7) there are no horizontal terms;
- the xz coupling is stronger than the yz coupling.

A set of beam dynamics simulations has been performed to test if the transfer matrix reduces to the form given by equation (4.3) also in the case of the hybrid storage ring.

In order to understand which elements of the transfer matrix can be neglected, it is necessary to compare the order of magnitude of the coefficients  $m_{ij}$  with  $i \neq j$  which represent the coupling strengths among the different phase spaces with the coefficients  $m_{ii}$  whose order of magnitude is obviously 1: only the coefficients whose order of magnitude is comparable to or greater than 1 are non-vanishing.

For all the simulations performed the RF cavity is ON, the number of turns is 10000 and the chromaticity values are zero.

A single particle subjected to both position and momentum deviations in all the directions has been considered. For each deviation introduced, the plots of the position and momentum components as a function of the number of turns are shown.

The comparison among the coefficients is preceded by a brief description of the plots.

Before proceeding, it is necessary to make a point. As mentioned in the previous section, the lattice has been built only considering the basic devices: the electric deflectors, the quadrupole magnets and the RF cavity. The designated devices for the correction of the betatron and synchrotron oscillations are the quadrupole magnets and the RF cavity respectively. It is important to remember that the RF cavity changes the velocity of a particle in the direction of its motion, i.e. it can act on the longitudinal momentum, while what the quadrupole magnets do is to change the transverse direction of a particle, i.e. they can act on the horizontal and vertical coordinates.

Keeping in mind this information, for each panel corresponding to a different deviation the description will be focused on the plots of the horizontal and vertical coordinates and of the longitudinal momentum.

#### ■ Longitudinal position offset

A particle with an initial longitudinal position offset of  $0.0001\text{ m}$  has been considered: this means that, according to Figure 2.2, the particle is ahead of the reference particle.

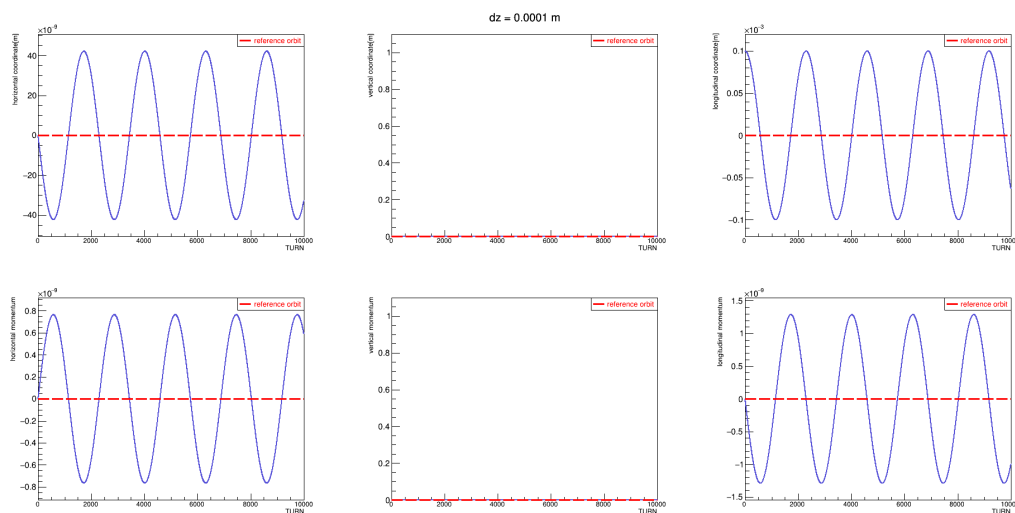


Figure 4.6

Plots of the position and momentum components as a function of the number of turns in the case of  $dz = 0.0001\text{ m}$ .

Referring to Figure 4.6, the plot of the longitudinal momentum shows the synchrotron oscillations due to the action of the RF cavity: since initially the particle is ahead of the reference particle, the RF cavity brings it back to the reference orbit decreasing its velocity, and, as a result, the particle oscillates back and forth.

The oscillations manifesting in the plot of the horizontal coordinate are due to a geometric effect which apparently couples the  $x$  and  $z$  motions: since initially the particle velocity decreases, the bending radius decreases too ( $\rho \propto v$ ) and the particle position also oscillates in the horizontal direction. The plot of the horizontal coordinate is in phase with the one of the longitudinal momentum.

There are no oscillations in the vertical direction.

### ■ Horizontal position offset

A particle with an initial horizontal position offset of  $0.0001\text{ m}$  has been considered: this means that, according to Figure 2.2, the particle is on the left of the reference particle.

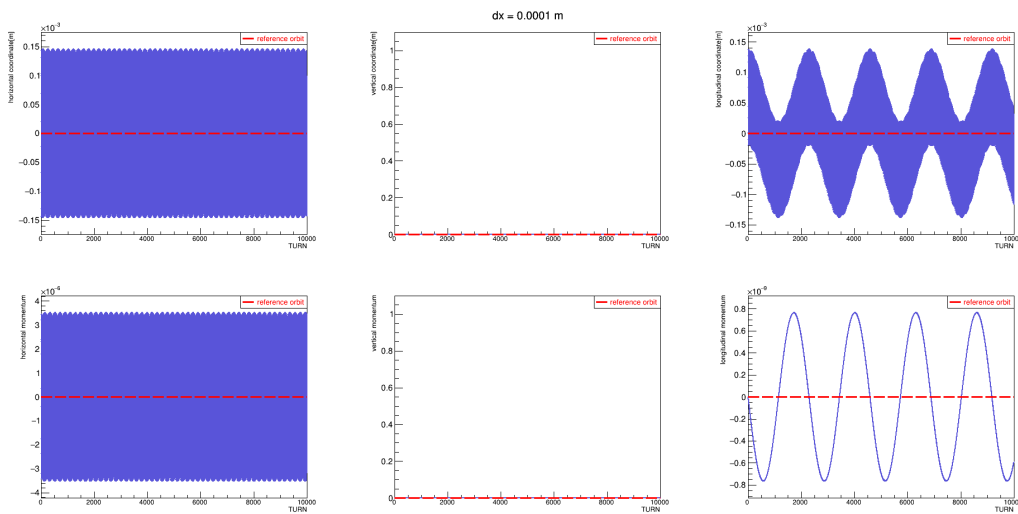


Figure 4.7

Plots of the position and momentum components as a function of the number of turns in the case of  $dx = 0.0001\text{ m}$ .

Referring to Figure 4.7, the plot of the horizontal coordinate shows the betatron oscillations due to the action of the quadrupole magnets: since initially the particle is on the left of the reference particle, the quadrupole magnets bring it back to the reference orbit decreasing its bending radius and, as a result, the particle oscillates to the right and to the left of the reference orbit.



Figure 4.8 shows in detail the corrective effect of the quadrupole magnets: they are at the corners and between one quadrupole magnet and another the particle travels straight.

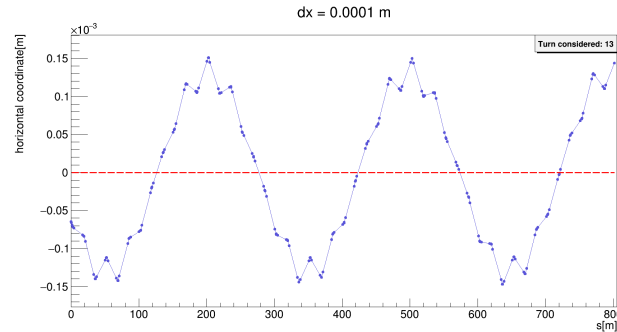


Figure 4.8

Plot of the horizontal coordinate within one turn in the case of  $dx = 0.0001 m$ .

Due to the transverse decoupling, there are no oscillations manifesting in the vertical direction, but there are in the longitudinal one and the reason is again the geometric  $xz$  coupling effect: since the bending radius decreases, the velocity decreases too ( $\rho \propto v$ ) as shown in the plot of the longitudinal momentum.

#### ■ Vertical position offset

A particle with an initial vertical position offset of  $0.0001 m$  has been considered: this means that, according to Figure 2.2, the particle is above the reference particle.

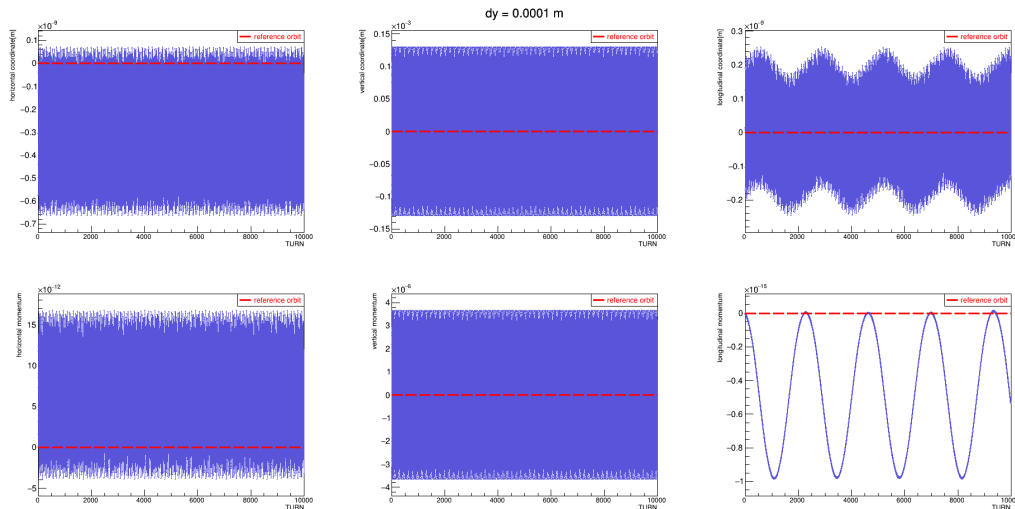


Figure 4.9

Plots of the position and momentum components as a function of the number of turns in the case of  $dy = 0.0001 m$ .

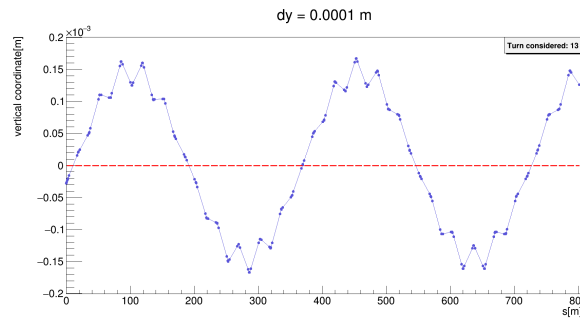


Figure 4.10

Plot of the vertical coordinate within one turn in the case of  $dy = 0.0001 \text{ m}$ .

Referring to Figure 4.9, the nature of betatron oscillations shown in the plot of the vertical coordinate is the same described for the previous case, as well as the existence of the geometric  $yz$  coupling effect with the difference that it seems to be very tiny compared to the geometric  $xz$  coupling effect of the previous case.

The presence of an asymmetry in the plot of the longitudinal momentum is due to the fact that the average longitudinal momentum must compensate the change in the path length. This phenomenon will be explained in detail in the next section.

The oscillations manifesting in the horizontal coordinate are due to the geometric  $xz$  coupling effect and reflect the ones of the longitudinal momentum.

■ Longitudinal momentum offset

A particle with an initial longitudinal momentum offset of 0.0001 has been considered.

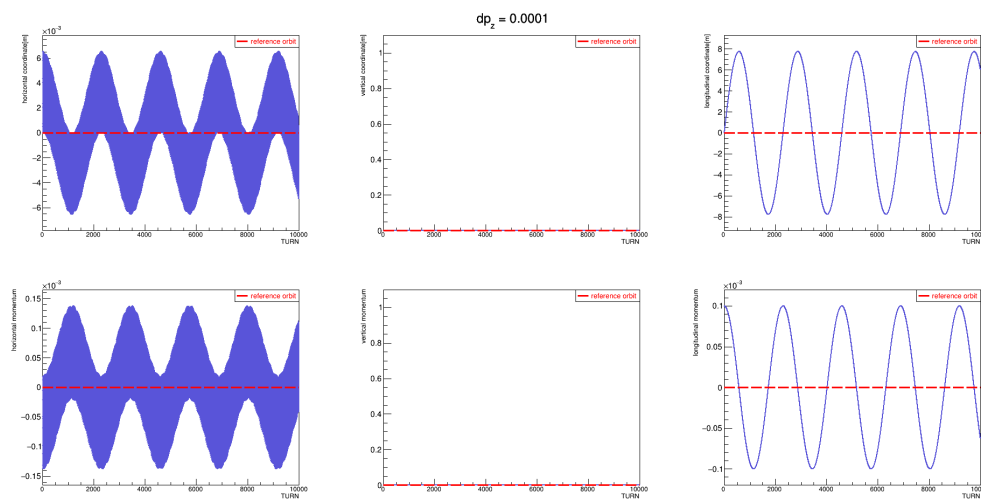


Figure 4.11

Plots of the position and momentum components as a function of the number of turns in the case of  $dp_z = 0.0001$ .

Referring to Figure 4.11, also in this case there is the geometric  $xz$  coupling effect: initially the particle is faster than the reference particle and, as a result, it is on the left of the reference particle ( $\rho \propto v$ ); then, due to the action of the RF cavity, the velocity decreases as shown in the plot of the longitudinal momentum and the radius decreases too as shown in the plot of the horizontal coordinate.

There are no oscillations in the vertical coordinate.

#### ■ Horizontal momentum offset

A particle with an initial horizontal momentum offset of 0.0001 has been considered.

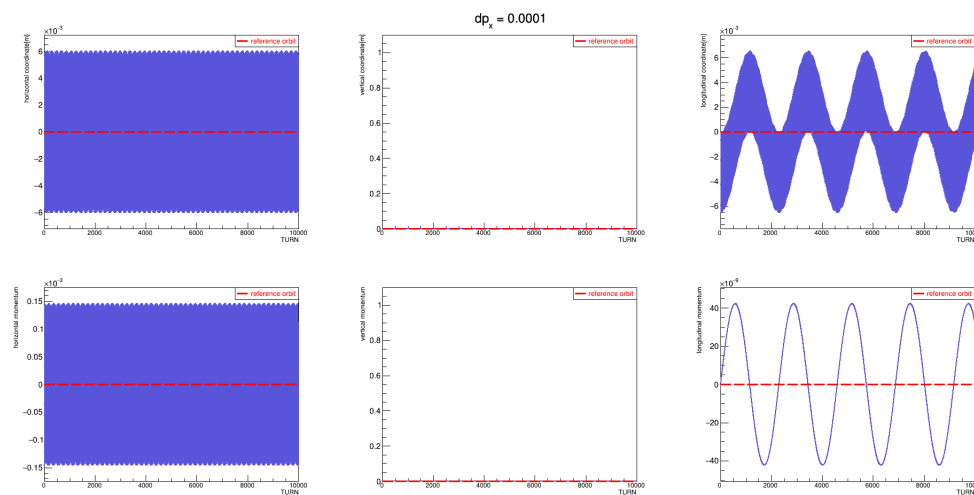


Figure 4.12

Plots of the position and momentum components as a function of the number of turns in the case of  $dp_x = 0.0001$ .

Referring to Figure 4.12, once again a deviation in the horizontal direction affects the motion in the longitudinal direction due to the geometric  $xz$  coupling effect, while the vertical direction remains untouched because of the transverse decoupling.

#### ■ Vertical momentum offset

A particle with an initial vertical momentum offset of 0.0001 has been considered.

Referring to Figure 4.13, this plots display the same information shown in Figure 4.9: the existence of the geometric  $yz$  coupling effect, the presence of an asymmetry in the plot of the longitudinal momentum due to the path lengthening phenomenon and the appearance of the  $xz$  coupling.

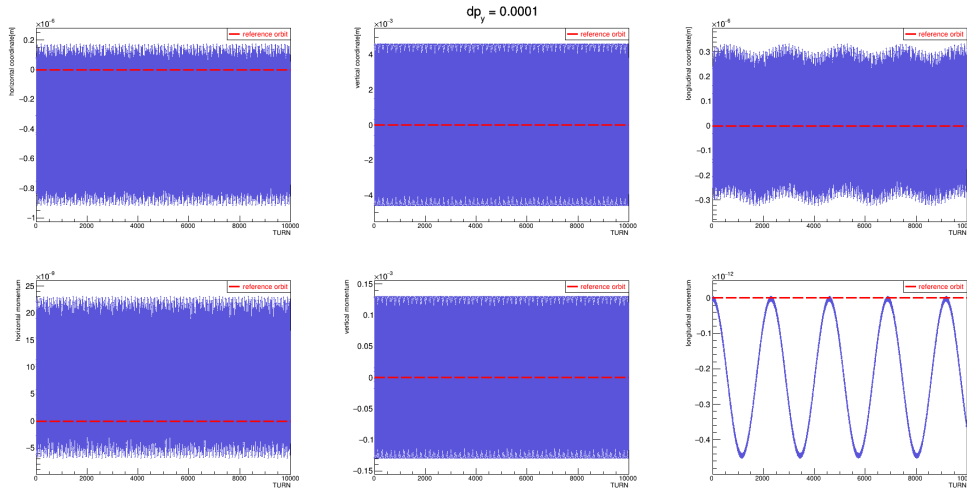


Figure 4.13

Plots of the position and momentum components as a function of the number of turns in the case of  $dp_y = 0.0001$ .

According to Figures 4.6, 4.7, 4.9, 4.11, 4.12 and 4.13, the orders of magnitude of the elements of the transfer matrix are reported in Figure 4.14.

|                       |                       |                        |                       |                       |                    |
|-----------------------|-----------------------|------------------------|-----------------------|-----------------------|--------------------|
| $m_{11} = 1$          | $m_{12} \sim 10$      | $m_{13} \sim 10^{-6}$  | $m_{14} \sim 10^{-3}$ | $m_{15} \sim 10^{-5}$ | $m_{16} \sim 10$   |
| $m_{21} \sim 10^{-2}$ | $m_{22} = 1$          | $m_{23} \sim 10^{-8}$  | $m_{24} \sim 10^{-5}$ | $m_{25} \sim 10^{-6}$ | $m_{26} \sim 1$    |
| $m_{31} = 0$          | $m_{32} = 0$          | $m_{33} = 1$           | $m_{34} \sim 10$      | $m_{35} = 0$          | $m_{36} = 0$       |
| $m_{41} = 0$          | $m_{42} = 0$          | $m_{43} \sim 10^{-2}$  | $m_{44} = 1$          | $m_{45} = 0$          | $m_{46} = 0$       |
| $m_{51} \sim 1$       | $m_{52} \sim 10$      | $m_{53} \sim 10^{-6}$  | $m_{54} \sim 10^{-3}$ | $m_{55} = 1$          | $m_{56} \sim 10^4$ |
| $m_{61} \sim 10^{-6}$ | $m_{62} \sim 10^{-5}$ | $m_{63} \sim 10^{-12}$ | $m_{64} \sim 10^{-9}$ | $m_{65} \sim 10^{-5}$ | $m_{66} = 1$       |

Figure 4.14

Table with the transfer matrix coefficients.

Among the non-vanishing coefficients, there are two “anomalous” ones:  $m_{56}$  and  $m_{65}$ ; they are defined as “anomalous” because they are much smaller and much greater than 1 respectively. They appear in equations (4.8) and (4.9): the first one expresses how the longitudinal momentum affects the longitudinal coordinate, while the second one expresses how the longitudinal coordinate affects the longitudinal momentum.

In order to understand why they are not rejected even if their strange values, the explicit form of equation (2.76) must be considered:

$$\begin{cases} z(s) = \cos(\omega_s t) z_0(s) + \frac{1}{\omega_s} \sin(\omega_s t) z'_0(s) \\ z'(s) = -\omega_s \sin(\omega_s t) z_0(s) + \cos(\omega_s t) z'_0(s) \end{cases} \quad (4.10)$$

The two interesting terms are the one highlighted in blue. In particular:

$$m_{56} = \frac{1}{\omega_s} \sin(\omega_s t) \quad (4.11)$$

$$m_{65} = -\omega_s \sin(\omega_s t) \quad (4.12)$$

This means the values of  $m_{56}$  and  $m_{65}$  reported in Figure 4.14 must be divided and multiplied respectively by the synchrotron frequency whose value is typically  $\omega_s \sim 10^{-4}$ . As a result:

$$m_{56} \sim 1 \quad (4.13)$$

$$m_{65} \sim 10^{-1} \quad (4.14)$$

In conclusion, the transfer matrix given by equation (4.3) appears to be also valid in the case of the hybrid storage ring.

## 4.5 Path lengthening

With *path lengthening* one means the change in the path length. It is due to both betatron and synchrotron oscillations.

The reason why the study of the path lengthening is very important is that it directly influences the change in the spin tune: since the spin tune depends on particle velocities as described by equation (2.100), each mechanism that changes particle velocities contributes to it; one of them is the path lengthening which manifests as the apparent change in particle velocities.

In general, the path lengthening can be written as the sum of two components:

$$\frac{\Delta L}{L} = \left( \frac{\Delta L}{L} \right)_l + \left( \frac{\Delta L}{L} \right)_t \quad (4.15)$$

where the subscripts  $l$  and  $t$  stand for *longitudinal* and *transverse* respectively.

The first component is due to longitudinal motion and contributes when a particle has a longitudinal momentum offset, while the second one is due to transverse motion and contributes when a particle has a transverse position offset.

The specific expressions of the two components have been studied separately.

According to equation (2.66), the longitudinal motion contributes as:

$$\left( \frac{\Delta L}{L} \right)_l = \alpha_c \delta \quad (4.16)$$

where  $\alpha_c$  is the momentum compaction factor which gives information about the rate of the path lengthening with the longitudinal momentum offset  $\delta$ .

At larger longitudinal momentum offsets the relation is not strictly linear:

$$\left(\frac{\Delta L}{L}\right)_l = \alpha_0 \delta + \alpha_1 \delta^2 \quad (4.17)$$

where  $\alpha_0$  is the 1<sup>st</sup> order momentum compaction factor,  $\alpha_1$  is the 2<sup>nd</sup> order momentum compaction factor and so on.

Based on what is known about pure magnetic storage rings, the contribution due to the transverse motion is:

$$\left(\frac{\Delta L}{L}\right)_t = -\frac{\pi}{L}(\varepsilon_x \xi_x + \varepsilon_y \xi_y) \quad (4.18)$$

where  $L$  is the storage ring circumference,  $\varepsilon$  is the emittance and  $\xi$  is chromaticity.

Finally, equation (4.15) becomes:

$$\frac{\Delta L}{L} = \alpha_0 \delta + \alpha_1 \delta^2 - \frac{\pi}{L}(\varepsilon_x \xi_x + \varepsilon_y \xi_y) \quad (4.19)$$

It can be referred as the laboratory formula for the path lengthening per turn.

The goal of this thesis is to verify equation (4.19) which is known to be valid for pure magnetic storage rings. The verification distinguishes between RF cavity OFF and ON.

In the case of RF cavity OFF, equation (4.19) has been tested by comparing its path lengthening values with the ones obtained from a formula derived from Bmad and for this reason referred as the simulator formula for the path lengthening.

In the case of RF cavity ON, equation (4.19) has been tested through the derivation of a formula for the longitudinal momentum amplitude.

Initially the case with the RF cavity OFF is considered.

Bmad does not provide a routine to directly measure the path lengthening; however, it provides an expression for the longitudinal coordinate of a particle subjected to a longitudinal momentum offset as a function of the location around the storage ring which is given by:

$$z(s) = -v^*(s)[t^*(s) - t(s)] \quad (4.20)$$

where  $v^*$  and  $t^*$  are the velocity and the travel time of the offset particle respectively and  $t$  is the travel time of the reference particle.

A customized expression for the path lengthening has been derived from equation (4.20).

If the longitudinal momentum offset is fixed, then the velocity of the offset particle is constant, the longitudinal coordinate builds up linearly generating a longitudinal position offset per turn which is given by:

$$\Delta z(s) = z(s) - z(s-L) = -v^*[t^*(s) - t(s) - t^*(s-L) + t(s-L)] = -v^*\Delta t \quad (4.21)$$

where  $\Delta t$  is the difference between the times taken by the offset particle and reference one to travel one turn.

Basically,  $\Delta z$  represents how much the offset particle moves away with respect to the reference particle in the same travel time.

In general, the path length for the offset particle is given by:

$$L^* = v^*t^* \rightarrow L + \Delta L = (v + \Delta v)(t + \Delta t) \quad (4.22)$$

where the relations  $L^* = L + \Delta L$ ,  $v^* = v + \Delta v$  and  $t^* = t + \Delta t$  have been used.

Dividing by  $L$  equation (4.22):

$$\begin{aligned} 1 + \frac{\Delta L}{L} &= \frac{(v + \Delta v)(t + \Delta t)}{L} = \left(1 + \frac{\Delta v}{v}\right) \left(1 + \frac{\Delta t}{t}\right) = 1 + \frac{\Delta v}{v} + \left(1 + \frac{\Delta v}{v}\right) \frac{\Delta t}{t} \rightarrow \\ &\rightarrow \frac{\Delta L}{L} = \frac{\Delta v}{v} + \left(1 + \frac{\Delta v}{v}\right) \frac{\Delta t}{t} \end{aligned} \quad (4.23)$$

where the relation  $L = vt$  has been used.

Using equation (4.21):

$$\frac{\Delta L}{L} = \frac{\Delta v}{v} + \left(1 + \frac{\Delta v}{v}\right) \left(-\frac{\Delta z}{v^*t}\right) = \frac{\Delta v}{v} - \frac{\Delta z}{t} \left[\frac{v + \Delta v}{v(v + \Delta v)}\right] = \frac{\Delta v}{v} - \frac{\Delta z}{vt} = \frac{\Delta v}{v} - \frac{\Delta z}{L} \quad (4.24)$$

where the relations  $v^* = v + \Delta v$  and  $L = vt$  have been used.

According to equation (2.67) and considering up to the 2<sup>nd</sup> order of  $\delta$ , the fractional change in the velocity can be written as:

$$\frac{\Delta v}{v} = \frac{\delta}{\gamma^2} - \frac{3\beta^2\delta^2}{2\gamma^2} + \dots \quad (4.25)$$

where  $\beta$  is the particle velocity and  $\gamma$  is the relativistic factor.

Finally, equation (4.24) becomes:

$$\frac{\Delta L}{L} = \frac{\delta}{\gamma^2} - \frac{3\beta^2\delta^2}{2\gamma^2} - \frac{\Delta z}{L} \quad (4.26)$$

To verify equation (4.19) in the case of RF cavity OFF it is necessary to check if the calculated values of the path lengthening through equation (4.19) are equal to the measured ones obtained through equation (4.26).

The next step is to verify equation (4.19) also in the case of RF cavity ON.

The starting point is the general expression for the path length of an offset particle:

$$L^* = v^* t^* \rightarrow L + \Delta L = (v + \Delta v)(t + \Delta t) \quad (4.27)$$

where the relations  $L^* = L + \Delta L$ ,  $v^* = v + \Delta v$  and  $t^* = t + \Delta t$  have been used.

Dividing by  $L$  equation (4.27):

$$1 + \frac{\Delta L}{L} = \frac{(v + \Delta v)(t + \Delta t)}{L} = \left(1 + \frac{\Delta v}{v}\right) \left(1 + \frac{\Delta t}{t}\right) \quad (4.28)$$

where the relation  $L = vt$  has been used.

Rearranging equation (4.28) and performing a Taylor expansion up to the 2<sup>nd</sup> order of the term at the denominator:

$$\begin{aligned} 1 + \frac{\Delta t}{t} &= \frac{1 + \frac{\Delta L}{L}}{1 + \frac{\Delta v}{v}} \sim 1 + \frac{\Delta L}{L} - \frac{\Delta v}{v} - \frac{\Delta v}{v} \frac{\Delta L}{L} + \left(\frac{\Delta v}{v}\right)^2 \rightarrow \\ &\rightarrow \frac{\Delta t}{t} = \frac{\Delta L}{L} - \frac{\Delta v}{v} - \frac{\Delta v}{v} \frac{\Delta L}{L} + \left(\frac{\Delta v}{v}\right)^2 \end{aligned} \quad (4.29)$$

Using equations (4.19) and (4.25):

$$\begin{aligned} \frac{\Delta t}{t} &= \alpha_0 \delta + \alpha_1 \delta^2 - \frac{\pi}{L} (\epsilon_x \xi_x + \epsilon_y \xi_y) - \frac{\delta}{\gamma^2} + \frac{3\beta^2 \delta^2}{2\gamma^2} - \\ &- \left(\frac{\delta}{\gamma^2} - \frac{3\beta^2 \delta^2}{2\gamma^2}\right) \left[\alpha_0 \delta + \alpha_1 \delta^2 - \frac{\pi}{L} (\epsilon_x \xi_x + \epsilon_y \xi_y)\right] + \left(\frac{\delta}{\gamma^2} - \frac{3\beta^2 \delta^2}{2\gamma^2}\right)^2 \end{aligned} \quad (4.30)$$

Performing all the calculations and considering the terms up to the 2<sup>nd</sup> order of  $\delta$ :

$$\begin{aligned} \frac{\Delta t}{t} &= -\frac{\pi}{L} (\epsilon_x \xi_x + \epsilon_y \xi_y) + \left[\alpha_0 - \frac{1}{\gamma^2} + \frac{1}{\gamma^2} \frac{\pi}{L} (\epsilon_x \xi_x + \epsilon_y \xi_y)\right] \delta + \\ &+ \left[\alpha_1 + \frac{3\beta^2}{2\gamma^2} - \frac{\alpha_0}{\gamma^2} - \frac{3\beta^2}{2\gamma^2} \frac{\pi}{L} (\epsilon_x \xi_x + \epsilon_y \xi_y) + \frac{1}{\gamma^4}\right] \delta^2 = \\ &= -\frac{\pi}{L} (\epsilon_x \xi_x + \epsilon_y \xi_y) + t_0 \delta + t_1 \delta^2 \end{aligned} \quad (4.31)$$



where:

$$t_0 = \alpha_0 - \frac{1}{\gamma^2} + \frac{1}{\gamma^2} \frac{\pi}{L} (\varepsilon_x \xi_x + \varepsilon_y \xi_y) \quad (4.32)$$

$$t_1 = \alpha_1 + \frac{3\beta^2}{2\gamma^2} - \frac{\alpha_0}{\gamma^2} - \frac{3\beta^2}{2\gamma^2} \frac{\pi}{L} (\varepsilon_x \xi_x + \varepsilon_y \xi_y) + \frac{1}{\gamma^4} \quad (4.33)$$

The function used to model the longitudinal momentum offset is:

$$\delta = \delta_m + \delta_a \cos(\omega n) \quad (4.34)$$

where the subscripts  $m$  and  $a$  stand for *mean* and *amplitude* respectively and  $n$  is the turn number.

Substituting equation (4.34) in equation (4.31):

$$\frac{\Delta t}{t} = -\frac{\pi}{L} (\varepsilon_x \xi_x + \varepsilon_y \xi_y) + t_0 \delta_m + t_0 \delta_a \cos(\omega n) + t_1 \delta_m^2 + t_1 \delta_a^2 \cos^2(\omega n) + t_1 \delta_m \delta_a \cos(\omega n) \quad (4.35)$$

Using the trigonometric formula for the  $\cos^2(\omega r)$  term:

$$\frac{\Delta t}{t} = -\frac{\pi}{L} (\varepsilon_x \xi_x + \varepsilon_y \xi_y) + t_0 \delta_m + t_0 \delta_a \cos(\omega n) + t_1 \delta_m^2 + \frac{t_1 \delta_a^2}{2} + \frac{t_1 \cos(2\omega n)}{2} + t_1 \delta_m \delta_a \cos(\omega n) \quad (4.36)$$

Since the RF cavity is ON, the average revolution time must be considered:

$$\left\langle \frac{\Delta t}{t} \right\rangle = \frac{1}{N} \int_0^N \frac{\Delta t}{t} dn \quad (4.37)$$

where  $N$  is the total number of turns considered.

Calculating the average of the single terms in equation (4.36) and assuming that  $N \gg 1/\omega$ :

$$\left\langle \frac{\Delta t}{t} \right\rangle = -\frac{\pi}{L} (\varepsilon_x \xi_x + \varepsilon_y \xi_y) + t_0 \delta_m + t_1 \left( \delta_m^2 + \frac{t_1 \delta_a^2}{2} \right) = -\frac{\pi}{L} (\varepsilon_x \xi_x + \varepsilon_y \xi_y) + t_0 \langle \delta \rangle + t_1 \langle \delta^2 \rangle \quad (4.38)$$

where:

$$\langle \delta \rangle = \delta_m \quad (4.39)$$

$$\langle \delta^2 \rangle = \langle \delta \rangle^2 + \frac{\delta_a^2}{2} \quad (4.40)$$

At this point an assumption is introduced.

Since the RF cavity is ON, by definition the particle beam is bunched resulting in a null average revolution time:

$$\left\langle \frac{\Delta t}{t} \right\rangle = 0 \rightarrow \frac{\pi}{L}(\varepsilon_x \xi_x + \varepsilon_y \xi_y) + t_0 \langle \delta \rangle + t_1 \langle \delta \rangle^2 = 0 \quad (4.41)$$

Finally, an equation which expresses the dependence of the longitudinal momentum amplitude on the average longitudinal momentum offset is obtained:

$$\delta_a^2 = \frac{2}{t_1} \left[ \frac{\pi}{L}(\varepsilon_x \xi_x + \varepsilon_y \xi_y) - t_0 \langle \delta \rangle - t_1 \langle \delta \rangle^2 \right] \quad (4.42)$$

To verify equation (4.19) in the case of RF cavity ON it is necessary to check equation (4.42) since its derivation is exactly based on equation (4.19).

### 4.5.1 Lattice

To allow the path lengthening studies, the initial code has been improved with the introduction of the sextupole magnets. Only the part concerning the devices has been modified as shown in Figure 4.15.

It is necessary to include the sextupole magnets because they control the chromaticity effects and the path lengthening must be studied as a function of different chromaticity values.

```

!-----DEVICES-----
ED: sbend
ED[fringe_type]      = basic_bend
ED[l]                = 1.85
ED[b_field]          = Bfield
ED[b_field_err]      = -Efield/(beta*c_light)
ED[b0_elec]          = -Efield
ED[exact_multipoles] = vertically_pure

D_Q: drift
D_Q[L]               = 1.9

QF: quadrupole
QF[L]                = 0.4
QF[b1_gradient]      = +k.Q

QD: quadrupole
QD[L]                = 0.4
QD[b1_gradient]      = -k.Q

D_RF: drift
D_RF[L]              = 0.45

RF: rfcavity
RF[l]                = 1.0
RF[harmon]           = 1
RF[voltage]          = 1.89e3
RF[phi0]             = 0.5

```

```

SXQF: sextupole
SXQF[1]          = 0.4
SXQF[k2]         = 0.1
SXQF[superimpose] = True
SXQF[ref]        = QF

SXQD: sextupole
SXQD[1]          = 0.4
SXQD[k2]         = 0.1
SXQD[superimpose] = True
SXQD[ref]        = QD

```

Figure 4.15

Illustration of the 2<sup>nd</sup> block of the code used to build the lattice with the introduction of the sextupole magnets.

## 4.6 Simulations and data analysis results: RF cavity OFF

To test equation (4.19), it is necessary to check if the calculated values of the path lengthening through equation (4.19) are equal to the measured ones obtained through equation (4.26). Before doing this, the longitudinal and transverse components must be tested separately.

Prior to proceeding, it is necessary to make a statement concerning the data analysis and the error propagation.

The quantities coming from Bmad do not have an attached error; they are  $L$ ,  $\delta$ ,  $\epsilon_x$ ,  $\epsilon_y$ ,  $\xi_x$  and  $\xi_y$ . On the other hand, all the quantities estimated from the raw data have errors which have been appropriately propagated. However, the errors are pretty small and the error bars cannot be appreciated in the majority of the plots.

### 4.6.1 Transverse motion contribution

The transverse motion contribution to the path lengthening is given by:

$$\frac{\Delta L}{L} = -\frac{\pi}{L}(\epsilon_x \xi_x + \epsilon_y \xi_y) \quad (4.43)$$

Since equation (4.43) is known to be valid only for pure magnetic storage rings, to test the transverse component in the case of the hybrid storage ring it is necessary to study the dependence of the path lengthening on the product between transverse emittance and chromaticity.

The simulations are characterized by the sole introduction of a transverse position offset. The two transverse directions have been studied separately.

Several sets of simulations have been performed which share the same chromaticity intervals and differ in the transverse position offset. The specifics are reported in Figure 4.16.

| HORIZONTAL  | VERTICAL  |
|---|---|
| (A) $\begin{cases} dx = 1 \times 10^{-4} m \\ \xi_x = \{-4, -3, -2, -1, 0, +1, +2, +3, +4\}, \xi_y = 0 \\ \xi_x = 0, \xi_y = \{-4, -3, -2, -1, 0, +1, +2, +3, +4\} \end{cases}$ | (J) $\begin{cases} dy = 1 \times 10^{-4} m \\ \xi_x = \{-4, -3, -2, -1, 0, +1, +2, +3, +4\}, \xi_y = 0 \\ \xi_x = 0, \xi_y = \{-4, -3, -2, -1, 0, +1, +2, +3, +4\} \end{cases}$ |
| (B) $\begin{cases} dx = 2 \times 10^{-4} m \\ \xi_x = \{-4, -3, -2, -1, 0, +1, +2, +3, +4\}, \xi_y = 0 \\ \xi_x = 0, \xi_y = \{-4, -3, -2, -1, 0, +1, +2, +3, +4\} \end{cases}$ | (K) $\begin{cases} dy = 2 \times 10^{-4} m \\ \xi_x = \{-4, -3, -2, -1, 0, +1, +2, +3, +4\}, \xi_y = 0 \\ \xi_x = 0, \xi_y = \{-4, -3, -2, -1, 0, +1, +2, +3, +4\} \end{cases}$ |
| (C) $\begin{cases} dx = 3 \times 10^{-4} m \\ \xi_x = \{-4, -3, -2, -1, 0, +1, +2, +3, +4\}, \xi_y = 0 \\ \xi_x = 0, \xi_y = \{-4, -3, -2, -1, 0, +1, +2, +3, +4\} \end{cases}$ | (L) $\begin{cases} dy = 3 \times 10^{-4} m \\ \xi_x = \{-4, -3, -2, -1, 0, +1, +2, +3, +4\}, \xi_y = 0 \\ \xi_x = 0, \xi_y = \{-4, -3, -2, -1, 0, +1, +2, +3, +4\} \end{cases}$ |
| (D) $\begin{cases} dx = 4 \times 10^{-4} m \\ \xi_x = \{-4, -3, -2, -1, 0, +1, +2, +3, +4\}, \xi_y = 0 \\ \xi_x = 0, \xi_y = \{-4, -3, -2, -1, 0, +1, +2, +3, +4\} \end{cases}$ | (M) $\begin{cases} dy = 4 \times 10^{-4} m \\ \xi_x = \{-4, -3, -2, -1, 0, +1, +2, +3, +4\}, \xi_y = 0 \\ \xi_x = 0, \xi_y = \{-4, -3, -2, -1, 0, +1, +2, +3, +4\} \end{cases}$ |
| (E) $\begin{cases} dx = 5 \times 10^{-4} m \\ \xi_x = \{-4, -3, -2, -1, 0, +1, +2, +3, +4\}, \xi_y = 0 \\ \xi_x = 0, \xi_y = \{-4, -3, -2, -1, 0, +1, +2, +3, +4\} \end{cases}$ | (N) $\begin{cases} dy = 5 \times 10^{-4} m \\ \xi_x = \{-4, -3, -2, -1, 0, +1, +2, +3, +4\}, \xi_y = 0 \\ \xi_x = 0, \xi_y = \{-4, -3, -2, -1, 0, +1, +2, +3, +4\} \end{cases}$ |
| (F) $\begin{cases} dx = 6 \times 10^{-4} m \\ \xi_x = \{-4, -3, -2, -1, 0, +1, +2, +3, +4\}, \xi_y = 0 \\ \xi_x = 0, \xi_y = \{-4, -3, -2, -1, 0, +1, +2, +3, +4\} \end{cases}$ | (O) $\begin{cases} dy = 6 \times 10^{-4} m \\ \xi_x = \{-4, -3, -2, -1, 0, +1, +2, +3, +4\}, \xi_y = 0 \\ \xi_x = 0, \xi_y = \{-4, -3, -2, -1, 0, +1, +2, +3, +4\} \end{cases}$ |
| (G) $\begin{cases} dx = 7 \times 10^{-4} m \\ \xi_x = \{-4, -3, -2, -1, 0, +1, +2, +3, +4\}, \xi_y = 0 \\ \xi_x = 0, \xi_y = \{-4, -3, -2, -1, 0, +1, +2, +3, +4\} \end{cases}$ | (P) $\begin{cases} dy = 7 \times 10^{-4} m \\ \xi_x = \{-4, -3, -2, -1, 0, +1, +2, +3, +4\}, \xi_y = 0 \\ \xi_x = 0, \xi_y = \{-4, -3, -2, -1, 0, +1, +2, +3, +4\} \end{cases}$ |
| (H) $\begin{cases} dx = 8 \times 10^{-4} m \\ \xi_x = \{-4, -3, -2, -1, 0, +1, +2, +3, +4\}, \xi_y = 0 \\ \xi_x = 0, \xi_y = \{-4, -3, -2, -1, 0, +1, +2, +3, +4\} \end{cases}$ | (Q) $\begin{cases} dy = 8 \times 10^{-4} m \\ \xi_x = \{-4, -3, -2, -1, 0, +1, +2, +3, +4\}, \xi_y = 0 \\ \xi_x = 0, \xi_y = \{-4, -3, -2, -1, 0, +1, +2, +3, +4\} \end{cases}$ |
| (I) $\begin{cases} dx = 9 \times 10^{-4} m \\ \xi_x = \{-4, -3, -2, -1, 0, +1, +2, +3, +4\}, \xi_y = 0 \\ \xi_x = 0, \xi_y = \{-4, -3, -2, -1, 0, +1, +2, +3, +4\} \end{cases}$ | (R) $\begin{cases} dy = 9 \times 10^{-4} m \\ \xi_x = \{-4, -3, -2, -1, 0, +1, +2, +3, +4\}, \xi_y = 0 \\ \xi_x = 0, \xi_y = \{-4, -3, -2, -1, 0, +1, +2, +3, +4\} \end{cases}$ |

Figure 4.16

Table with the specifics of the sets of simulations performed.

The adopted procedure is described as follows:

1. measurement of the path lengthening through equation (4.26);

Equation (4.26) reduces to:

$$\frac{\Delta L}{L} = -\frac{\Delta z}{L} \quad (4.44)$$

because there is no longitudinal momentum offset.

$\Delta z$  has been evaluated as the slope of the straight line which better fits the points of the plot of the longitudinal coordinate as a function of the number of turns.

A model plot from the set of simulations denoted with A is shown in Figure 4.17.

The error on the path lengthening has been evaluated through the general formula of error propagation:

$$err\left(\frac{\Delta L}{L}\right) = \frac{err(\Delta z)}{L} \quad (4.45)$$

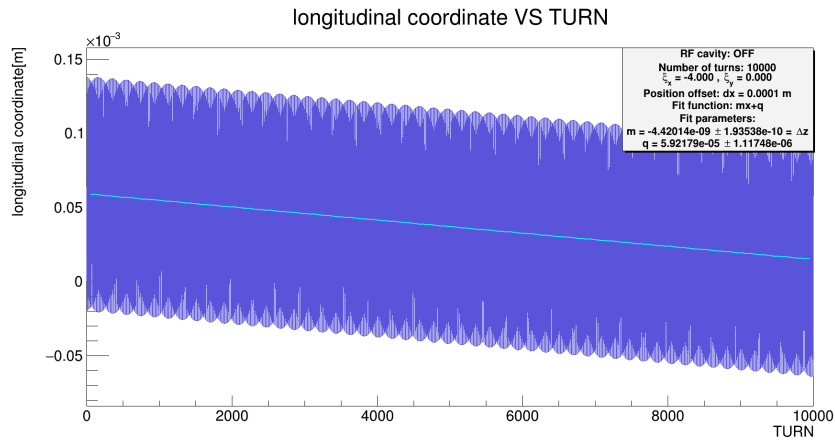


Figure 4.17

Model plot of longitudinal coordinate VS number of turns from the set of simulations denoted with A.

This step has been repeated for each pair of chromaticity values corresponding to a specific transverse position offset and for each transverse position offset.

2. study of the dependence of the path lengthening on chromaticity;

Figure 4.18 and 4.19 show the plots of the path lengthening as a function of horizontal and vertical chromaticity respectively for the set of simulations denoted with A.

It is clear that since the position offset is in the horizontal direction, the variation of the vertical chromaticity affects the path lengthening in a negligible way ( $10^{-15}$ ) with respect to what the variation of the horizontal chromaticity does ( $10^{-12}$ ).

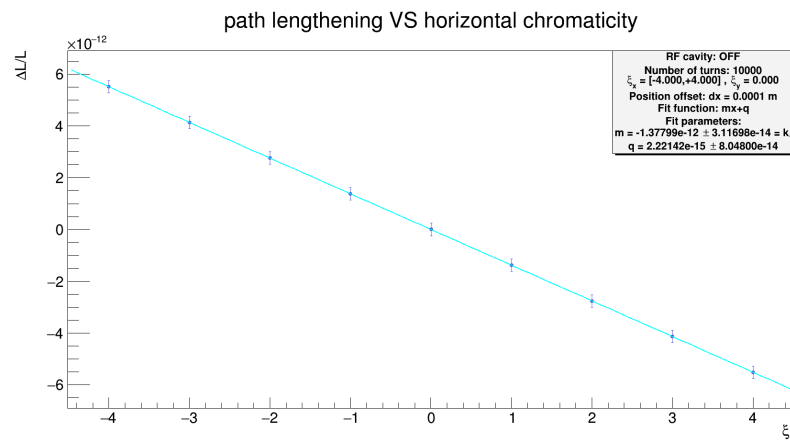


Figure 4.18

Plot of path lengthening VS horizontal chromaticity for the set of simulations denoted with A.

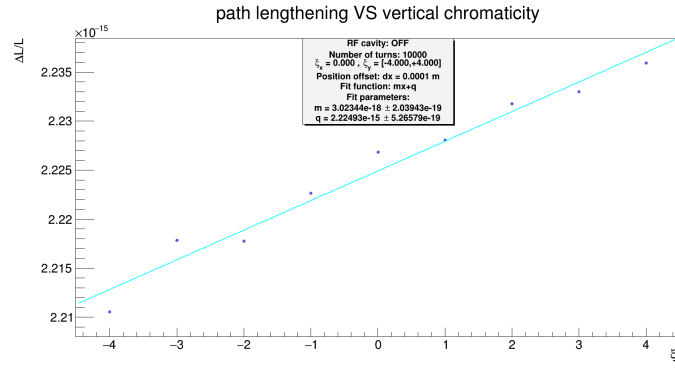


Figure 4.19

Plot of path lengthening VS vertical chromaticity for the set of simulations denoted with *A*.

The equivalent situation occurs when considering a vertical position offset as shown in Figures 4.20 and 4.21 which refer to the set of simulations denoted with *J*.

Summarizing, the horizontal chromaticity affects the path lengthening when a horizontal position offset is introduced, while the vertical chromaticity affects the path lengthening when a vertical position offset is introduced.

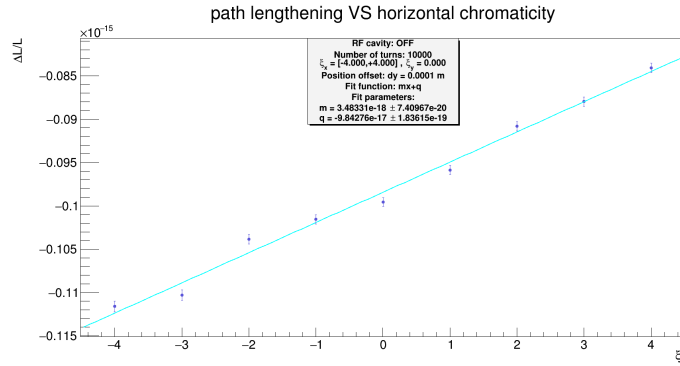


Figure 4.20

Plot of path lengthening VS horizontal chromaticity for the set of simulations denoted with *J*.

Figures 4.18 and 4.20 show that there is a linear dependence between the path lengthening and chromaticity:

$$\left(\frac{\Delta L}{L}\right)_x = k_1 \xi_x \quad (4.46)$$

$$\left(\frac{\Delta L}{L}\right)_y = k_2 \xi_y \quad (4.47)$$

where  $k_1$  and  $k_2$  are the proportionality constants.

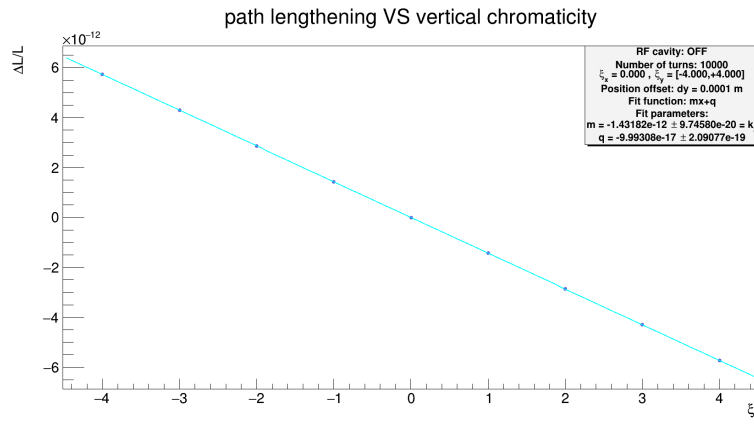


Figure 4.21

Plot of path lengthening VS vertical chromaticity for the set of simulations denoted with  $J$ .

This step has been repeated for each transverse position offset.

### 3. calculation of the transverse emittance;

According to Figure 2.13, the transverse emittance has been evaluated as:

$$\begin{cases} u_0 = \sqrt{\frac{\epsilon_u}{\gamma_u}} \\ p_{u,max} = \sqrt{\epsilon_u \gamma_u} \end{cases} \rightarrow \epsilon_u = u_0 \cdot p_{u,max} \quad (4.48)$$

This step has been repeated for each transverse position offset.

### 4. study of the dependence of $k_1$ and $k_2$ on the transverse emittance;

Figures 4.22 shows the plot of  $k_1$  (one value for each horizontal position offset) as a function of the horizontal emittance.

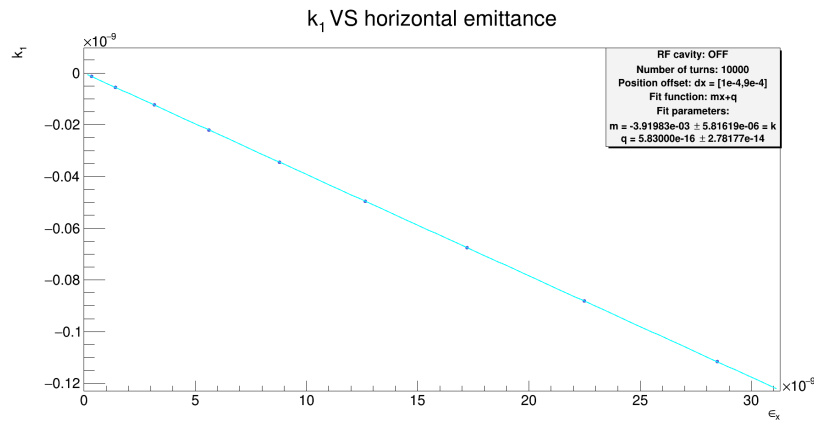


Figure 4.22

Plot of  $k_1$  VS horizontal emittance.

Considering a horizontal position offset, there is a linear dependence between  $k_1$  and the horizontal emittance.

The slope of the straight line which better fits the points corresponds to the proportionality constant  $k$  between the path lengthening and the product between horizontal emittance and horizontal chromaticity:

$$\left(\frac{\Delta L}{L}\right)_x = k \varepsilon_x \xi_x \rightarrow k = m = -0.00391983 \sim \frac{\pi}{L} \rightarrow \left(\frac{\Delta L}{L}\right)_x = -\frac{\pi}{L} \varepsilon_x \xi_x \quad (4.49)$$

The value of  $k$  is exactly given by the ratio between the  $\pi$  constant and the storage ring circumference.

The same result is obtained when considering a vertical position offset:

$$\left(\frac{\Delta L}{L}\right)_y = k \varepsilon_y \xi_y \rightarrow k = m = -0.00391914 \sim \frac{\pi}{L} \rightarrow \left(\frac{\Delta L}{L}\right)_y = -\frac{\pi}{L} \varepsilon_y \xi_y \quad (4.50)$$

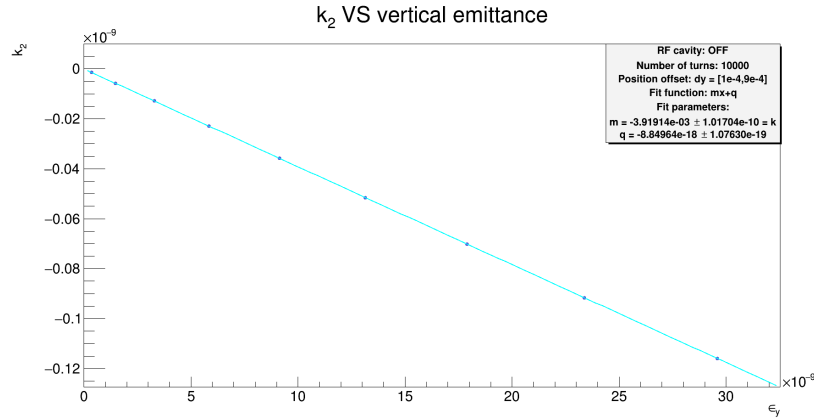


Figure 4.23  
Plot of  $k_2$  VS vertical emittance.

Considering the two transverse directions together:

$$\begin{cases} \left(\frac{\Delta L}{L}\right)_x = -\frac{\pi}{L} \varepsilon_x \xi_x \\ \left(\frac{\Delta L}{L}\right)_y = -\frac{\pi}{L} \varepsilon_y \xi_y \end{cases} \rightarrow \frac{\Delta L}{L} = -\frac{\pi}{L} (\varepsilon_x \xi_x + \varepsilon_y \xi_y) \quad (4.51)$$

In conclusion, equation (4.43) appears to also apply in the case of the hybrid storage ring.

The plots for the other non-mentioned sets of simulations are reported in the Appendix A1 for the horizontal position offset and in the Appendix A2 for the vertical position offset.



## 4.6.2 Longitudinal motion contribution

The longitudinal motion contribution to the path lengthening is given by:

$$\frac{\Delta L}{L} = \alpha_0 \delta_0 + \alpha_1 \delta_0^2 \quad (4.52)$$

where the subscripts 0 indicates the fact that in the case of the RF cavity OFF the longitudinal momentum offset is initially set and remains constant turn by turn.

To test the longitudinal component in the case of the hybrid storage ring, it is necessary to study the dependence of the path lengthening on the momentum offset.

The simulations are characterized by the sole introduction of a longitudinal momentum offset. Several sets of simulations have been performed which share the same longitudinal momentum offset interval and differ in the chromaticity values. The specifics are reported in Figure 4.24.

| $\xi_x = -4$   | $\xi_x = +4$   |
|--|--|
| (A) $\left\{ \begin{array}{l} \delta_0 = \{1,2,3,4,5,6,7,8,9\} \times 10^{-4} \\ \xi_x = -4, \xi_y = -4 \end{array} \right.$ | (J) $\left\{ \begin{array}{l} \delta_0 = \{1,2,3,4,5,6,7,8,9\} \times 10^{-4} \\ \xi_x = +4, \xi_y = -4 \end{array} \right.$ |
| (B) $\left\{ \begin{array}{l} \delta_0 = \{1,2,3,4,5,6,7,8,9\} \times 10^{-4} \\ \xi_x = -4, \xi_y = -3 \end{array} \right.$ | (K) $\left\{ \begin{array}{l} \delta_0 = \{1,2,3,4,5,6,7,8,9\} \times 10^{-4} \\ \xi_x = +4, \xi_y = -3 \end{array} \right.$ |
| (C) $\left\{ \begin{array}{l} \delta_0 = \{1,2,3,4,5,6,7,8,9\} \times 10^{-4} \\ \xi_x = -4, \xi_y = -2 \end{array} \right.$ | (L) $\left\{ \begin{array}{l} \delta_0 = \{1,2,3,4,5,6,7,8,9\} \times 10^{-4} \\ \xi_x = +4, \xi_y = -2 \end{array} \right.$ |
| (D) $\left\{ \begin{array}{l} \delta_0 = \{1,2,3,4,5,6,7,8,9\} \times 10^{-4} \\ \xi_x = -4, \xi_y = -1 \end{array} \right.$ | (M) $\left\{ \begin{array}{l} \delta_0 = \{1,2,3,4,5,6,7,8,9\} \times 10^{-4} \\ \xi_x = +4, \xi_y = -1 \end{array} \right.$ |
| (E) $\left\{ \begin{array}{l} \delta_0 = \{1,2,3,4,5,6,7,8,9\} \times 10^{-4} \\ \xi_x = -4, \xi_y = 0 \end{array} \right.$  | (N) $\left\{ \begin{array}{l} \delta_0 = \{1,2,3,4,5,6,7,8,9\} \times 10^{-4} \\ \xi_x = +4, \xi_y = 0 \end{array} \right.$  |
| (F) $\left\{ \begin{array}{l} \delta_0 = \{1,2,3,4,5,6,7,8,9\} \times 10^{-4} \\ \xi_x = -4, \xi_y = +1 \end{array} \right.$ | (O) $\left\{ \begin{array}{l} \delta_0 = \{1,2,3,4,5,6,7,8,9\} \times 10^{-4} \\ \xi_x = +4, \xi_y = +1 \end{array} \right.$ |
| (G) $\left\{ \begin{array}{l} \delta_0 = \{1,2,3,4,5,6,7,8,9\} \times 10^{-4} \\ \xi_x = -4, \xi_y = +2 \end{array} \right.$ | (P) $\left\{ \begin{array}{l} \delta_0 = \{1,2,3,4,5,6,7,8,9\} \times 10^{-4} \\ \xi_x = +4, \xi_y = +2 \end{array} \right.$ |
| (H) $\left\{ \begin{array}{l} \delta_0 = \{1,2,3,4,5,6,7,8,9\} \times 10^{-4} \\ \xi_x = -4, \xi_y = +3 \end{array} \right.$ | (Q) $\left\{ \begin{array}{l} \delta_0 = \{1,2,3,4,5,6,7,8,9\} \times 10^{-4} \\ \xi_x = +4, \xi_y = +3 \end{array} \right.$ |
| (I) $\left\{ \begin{array}{l} \delta_0 = \{1,2,3,4,5,6,7,8,9\} \times 10^{-4} \\ \xi_x = -4, \xi_y = +4 \end{array} \right.$ | (R) $\left\{ \begin{array}{l} \delta_0 = \{1,2,3,4,5,6,7,8,9\} \times 10^{-4} \\ \xi_x = +4, \xi_y = +4 \end{array} \right.$ |

Figure 4.24

Table with the specifics of the sets of simulations performed.

The path lengthening has been measured through equation (4.26) and plotted as a function of the momentum offset.

Figure 4.25 shows the plot for the set of simulations denoted with A.

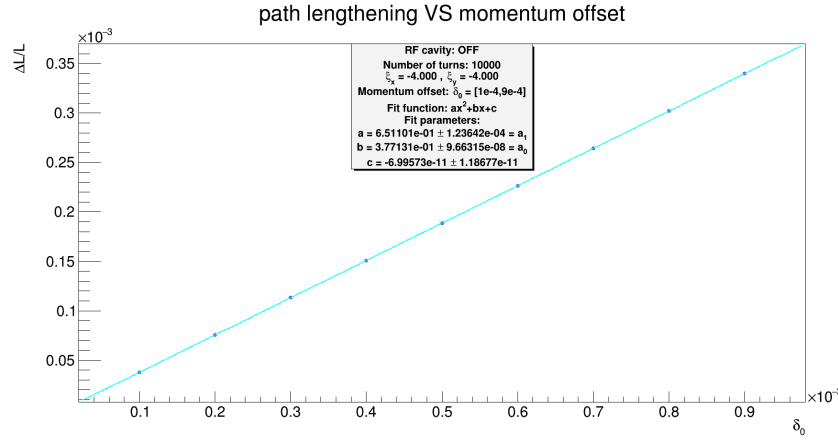


Figure 4.25

Plot of path lengthening VS momentum offset for the set of simulations denoted with A.

The plot of the path lengthening as a function of the momentum offset is a distribution which is well fitted by a polynomial of the second order. The values of the compaction factors can be extracted from the fit function as shown in the legend of Figure 4.25.

However, these are not the correct values of the compaction factors because they do not take into account also the transverse contribution.

As described previously in relation to Figure 4.6, a non-vanishing longitudinal momentum offset generates an  $xz$  coupling, while the  $yz$  coupling is negligible. Taking into account the horizontal contribution, equation (4.52) becomes:

$$\frac{\Delta L}{L} = \left(\alpha_0 - \frac{\pi}{L}x_0\xi_x\right)\delta_0 + \left(\alpha_1 - \frac{\pi}{L}x_1\xi_x\right)\delta_0^2 = a_0\delta_0 + a_1\delta_0^2 \quad (4.53)$$

where:

$$a_0 = \alpha_0 - \frac{\pi}{L}x_0\xi_x \quad (4.54)$$

$$a_1 = \alpha_1 - \frac{\pi}{L}x_1\xi_x \quad (4.55)$$

According to the legend of Figure 4.25, the values of the factors  $a_0$  and  $a_1$  have been derived. To get the correct values of the compaction factors, it is necessary to derive the factors  $x_0$  and  $x_1$ . They can be evaluated from the plot of the horizontal emittance as a function of the momentum offset.

According to Figure 2.13, the horizontal emittance, which is non-zero due to the xz coupling, has been evaluated as:

$$\begin{cases} x_{max} = \sqrt{\epsilon_x \beta_x} \\ p_{x,max} = \sqrt{\epsilon_x \gamma_x} \end{cases} \rightarrow \epsilon_x = \frac{x_{max} \cdot p_{x,max}}{\sqrt{\beta_x \gamma_x}} \quad (4.56)$$

Figure 4.26 shows the plot of the horizontal emittance as a function of the momentum offset for the set of simulations denoted with A.

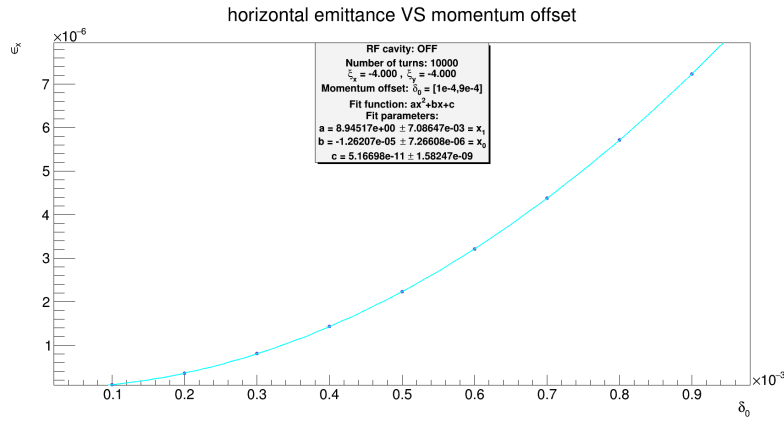


Figure 4.26

Plot of horizontal emittance VS momentum offset for the set of simulations denoted with A.

The points are well fitted by a polynomial of the second order and the values of the factors  $x_0$  and  $x_1$  can be extracted from the fit function as shown in the legend of Figure 4.26.

Finally, using equations (4.54) and (4.55), it is possible to derive the correct values of the compaction factors which are reported in Figure 4.27.

The errors on the compaction factors have been evaluated through the general formula of error propagation:

$$err(\alpha_{\#}) = \sqrt{\left(\frac{\partial \alpha_{\#}}{\partial a_{\#}} err(a_{\#})\right)^2 + \left(\frac{\partial \alpha_{\#}}{\partial x_{\#}} err(x_{\#})\right)^2} \quad (4.57)$$

where  $\# = 0, 1$  according to the compaction factor considered.

|            |                                       |
|------------|---------------------------------------|
| $\alpha_0$ | $0.377131 \pm 1.49374 \times 10^{-7}$ |
| $\alpha_1$ | $0.510871 \pm 1.66219 \times 10^{-4}$ |

Figure 4.27

Table with the compaction factors values and errors.

The plots for the other non-mentioned sets of simulations are reported in the Appendix B1 for  $\xi_x = -4$  and in the Appendix B2 for  $\xi_x = +4$ .

### 4.6.3 Full formula

To test the full formula given by equation (4.19), the calculated values of the path lengthening obtained through equation (4.19) must be compared with the measured ones obtained through equation (4.26).

The simulations are characterized by the introduction of a longitudinal momentum offset and horizontal and vertical position offsets.

Several sets of simulations have been performed which share the same longitudinal momentum offset interval and the same transverse position offsets and differ in the chromaticity values.

The specifics are reported in Figure 4.28.

| $\xi_x = -4$  | $\xi_x = +4$  |
|---|---|
| (A) $\begin{cases} \delta_0 = \{1,2,3,4,5,6,7,8,9\} \times 10^{-4} \\ dx = 1 \times 10^{-2} \rightarrow \epsilon_x = 3.51547 \times 10^{-6} \\ dy = 1 \times 10^{-2} \rightarrow \epsilon_y = 3.65338 \times 10^{-6} \\ \xi_x = -4, \xi_y = -4 \end{cases}$ | (J) $\begin{cases} \delta_0 = \{1,2,3,4,5,6,7,8,9\} \times 10^{-4} \\ dx = 1 \times 10^{-2} \rightarrow \epsilon_x = 3.51547 \times 10^{-6} \\ dy = 1 \times 10^{-2} \rightarrow \epsilon_y = 3.65338 \times 10^{-6} \\ \xi_x = +4, \xi_y = -4 \end{cases}$ |
| (B) $\begin{cases} \delta_0 = \{1,2,3,4,5,6,7,8,9\} \times 10^{-4} \\ dx = 1 \times 10^{-2} \rightarrow \epsilon_x = 3.51547 \times 10^{-6} \\ dy = 1 \times 10^{-2} \rightarrow \epsilon_y = 3.65338 \times 10^{-6} \\ \xi_x = -4, \xi_y = -3 \end{cases}$ | (K) $\begin{cases} \delta_0 = \{1,2,3,4,5,6,7,8,9\} \times 10^{-4} \\ dx = 1 \times 10^{-2} \rightarrow \epsilon_x = 3.51547 \times 10^{-6} \\ dy = 1 \times 10^{-2} \rightarrow \epsilon_y = 3.65338 \times 10^{-6} \\ \xi_x = +4, \xi_y = -3 \end{cases}$ |
| (C) $\begin{cases} \delta_0 = \{1,2,3,4,5,6,7,8,9\} \times 10^{-4} \\ dx = 1 \times 10^{-2} \rightarrow \epsilon_x = 3.51547 \times 10^{-6} \\ dy = 1 \times 10^{-2} \rightarrow \epsilon_y = 3.65338 \times 10^{-6} \\ \xi_x = -4, \xi_y = -2 \end{cases}$ | (L) $\begin{cases} \delta_0 = \{1,2,3,4,5,6,7,8,9\} \times 10^{-4} \\ dx = 1 \times 10^{-2} \rightarrow \epsilon_x = 3.51547 \times 10^{-6} \\ dy = 1 \times 10^{-2} \rightarrow \epsilon_y = 3.65338 \times 10^{-6} \\ \xi_x = +4, \xi_y = -2 \end{cases}$ |
| (D) $\begin{cases} \delta_0 = \{1,2,3,4,5,6,7,8,9\} \times 10^{-4} \\ dx = 1 \times 10^{-2} \rightarrow \epsilon_x = 3.51547 \times 10^{-6} \\ dy = 1 \times 10^{-2} \rightarrow \epsilon_y = 3.65338 \times 10^{-6} \\ \xi_x = -4, \xi_y = -1 \end{cases}$ | (M) $\begin{cases} \delta_0 = \{1,2,3,4,5,6,7,8,9\} \times 10^{-4} \\ dx = 1 \times 10^{-2} \rightarrow \epsilon_x = 3.51547 \times 10^{-6} \\ dy = 1 \times 10^{-2} \rightarrow \epsilon_y = 3.65338 \times 10^{-6} \\ \xi_x = +4, \xi_y = -1 \end{cases}$ |
| (E) $\begin{cases} \delta_0 = \{1,2,3,4,5,6,7,8,9\} \times 10^{-4} \\ dx = 1 \times 10^{-2} \rightarrow \epsilon_x = 3.51547 \times 10^{-6} \\ dy = 1 \times 10^{-2} \rightarrow \epsilon_y = 3.65338 \times 10^{-6} \\ \xi_x = -4, \xi_y = 0 \end{cases}$  | (N) $\begin{cases} \delta_0 = \{1,2,3,4,5,6,7,8,9\} \times 10^{-4} \\ dx = 1 \times 10^{-2} \rightarrow \epsilon_x = 3.51547 \times 10^{-6} \\ dy = 1 \times 10^{-2} \rightarrow \epsilon_y = 3.65338 \times 10^{-6} \\ \xi_x = +4, \xi_y = 0 \end{cases}$  |
| (F) $\begin{cases} \delta_0 = \{1,2,3,4,5,6,7,8,9\} \times 10^{-4} \\ dx = 1 \times 10^{-2} \rightarrow \epsilon_x = 3.51547 \times 10^{-6} \\ dy = 1 \times 10^{-2} \rightarrow \epsilon_y = 3.65338 \times 10^{-6} \\ \xi_x = -4, \xi_y = +1 \end{cases}$ | (O) $\begin{cases} \delta_0 = \{1,2,3,4,5,6,7,8,9\} \times 10^{-4} \\ dx = 1 \times 10^{-2} \rightarrow \epsilon_x = 3.51547 \times 10^{-6} \\ dy = 1 \times 10^{-2} \rightarrow \epsilon_y = 3.65338 \times 10^{-6} \\ \xi_x = +4, \xi_y = +1 \end{cases}$ |
| (G) $\begin{cases} \delta_0 = \{1,2,3,4,5,6,7,8,9\} \times 10^{-4} \\ dx = 1 \times 10^{-2} \rightarrow \epsilon_x = 3.51547 \times 10^{-6} \\ dy = 1 \times 10^{-2} \rightarrow \epsilon_y = 3.65338 \times 10^{-6} \\ \xi_x = -4, \xi_y = +2 \end{cases}$ | (P) $\begin{cases} \delta_0 = \{1,2,3,4,5,6,7,8,9\} \times 10^{-4} \\ dx = 1 \times 10^{-2} \rightarrow \epsilon_x = 3.51547 \times 10^{-6} \\ dy = 1 \times 10^{-2} \rightarrow \epsilon_y = 3.65338 \times 10^{-6} \\ \xi_x = +4, \xi_y = +2 \end{cases}$ |

|   |   |
|---|---|
| (H) $\begin{cases} \delta_0 = \{1,2,3,4,5,6,7,8,9\} \times 10^{-4} \\ dx = 1 \times 10^{-2} \rightarrow \epsilon_x = 3.51547 \times 10^{-6} \\ dy = 1 \times 10^{-2} \rightarrow \epsilon_y = 3.65338 \times 10^{-6} \\ \xi_x = -4, \xi_y = +3 \end{cases}$ | (Q) $\begin{cases} \delta_0 = \{1,2,3,4,5,6,7,8,9\} \times 10^{-4} \\ dx = 1 \times 10^{-2} \rightarrow \epsilon_x = 3.51547 \times 10^{-6} \\ dy = 1 \times 10^{-2} \rightarrow \epsilon_y = 3.65338 \times 10^{-6} \\ \xi_x = +4, \xi_y = +3 \end{cases}$ |
| (I) $\begin{cases} \delta_0 = \{1,2,3,4,5,6,7,8,9\} \times 10^{-4} \\ dx = 1 \times 10^{-2} \rightarrow \epsilon_x = 3.51547 \times 10^{-6} \\ dy = 1 \times 10^{-2} \rightarrow \epsilon_y = 3.65338 \times 10^{-6} \\ \xi_x = -4, \xi_y = +4 \end{cases}$ | (R) $\begin{cases} \delta_0 = \{1,2,3,4,5,6,7,8,9\} \times 10^{-4} \\ dx = 1 \times 10^{-2} \rightarrow \epsilon_x = 3.51547 \times 10^{-6} \\ dy = 1 \times 10^{-2} \rightarrow \epsilon_y = 3.65338 \times 10^{-6} \\ \xi_x = +4, \xi_y = +4 \end{cases}$ |

Figure 4.28

Table with the specifics of the sets of simulations performed.

The values of the compaction factors used in equation (4.19) are the ones derived from the study of the longitudinal motion contribution.

The errors on the calculated values of the path lengthening have been evaluated through the general formula of error propagation:

$$err\left(\frac{\Delta L}{L}\right) = \sqrt{\left[\frac{\partial\left(\frac{\Delta L}{L}\right)}{\partial\alpha_0}err(\alpha_0)\right]^2 + \left[\frac{\partial\left(\frac{\Delta L}{L}\right)}{\partial\alpha_1}err(\alpha_1)\right]^2} \quad (4.58)$$

Figure 4.29 shows the plot of both the measured and calculated values of the path lengthening as a function of the momentum offset for the set of simulations denoted with A.

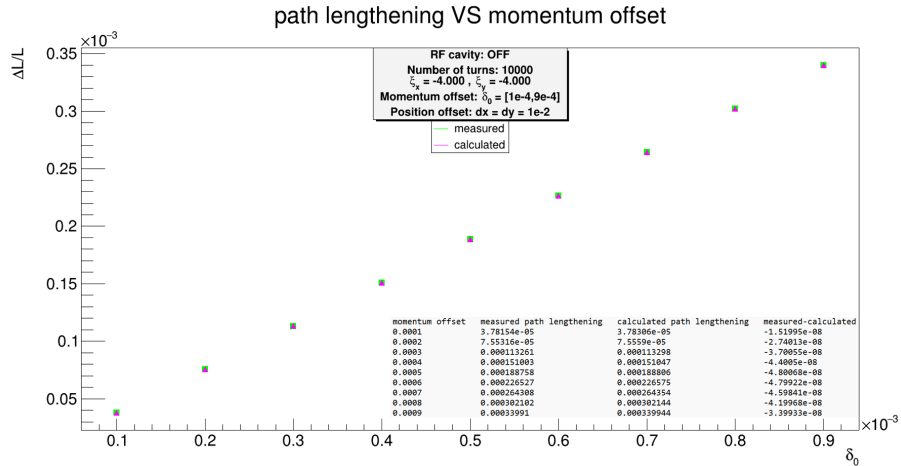


Figure 4.29

Plot of measured and calculated path lengthening VS momentum offset for the set of simulations denoted with A.

The measured and calculated values are comparable suggesting the validity of equation (4.19) for the hybrid storage ring in the case of RF cavity OFF.

The plots for the other non-mentioned sets of simulations are reported in the Appendix C1 for  $\xi_x = -4$  and in the Appendix C2 for  $\xi_x = +4$ .

## 4.7 Simulations and data analysis results: RF cavity ON

To test equation (4.19), the calculated values of the longitudinal momentum amplitude obtained through equation (4.42) must be compared with the measured ones which can be easily derived from the raw data.

The simulations are characterized by the introduction of a longitudinal momentum offset and horizontal and vertical position offsets.

Several sets of simulations have been performed which share the same longitudinal momentum offset interval and the same transverse position offsets and differ in the chromaticity values. The specifics are reported in Figure 4.30.

| $\xi_x = -4$   | $\xi_x = +4$   |
|--|--|
| (A) $\left\{ \begin{array}{l} \delta_0 = \{1,2,3,4,5,6,7,8,9\} \times 10^{-4} \\ dx = 1 \times 10^{-2} \rightarrow \epsilon_x = 3.51547 \times 10^{-6} \\ dy = 1 \times 10^{-2} \rightarrow \epsilon_y = 3.65338 \times 10^{-6} \\ \xi_x = -4, \xi_y = -4 \end{array} \right.$ | (C) $\left\{ \begin{array}{l} \delta_0 = \{1,2,3,4,5,6,7,8,9\} \times 10^{-4} \\ dx = 1 \times 10^{-2} \rightarrow \epsilon_x = 3.51547 \times 10^{-6} \\ dy = 1 \times 10^{-2} \rightarrow \epsilon_y = 3.65338 \times 10^{-6} \\ \xi_x = +4, \xi_y = -4 \end{array} \right.$ |
| (B) $\left\{ \begin{array}{l} \delta_0 = \{1,2,3,4,5,6,7,8,9\} \times 10^{-4} \\ dx = 1 \times 10^{-2} \rightarrow \epsilon_x = 3.51547 \times 10^{-6} \\ dy = 1 \times 10^{-2} \rightarrow \epsilon_y = 3.65338 \times 10^{-6} \\ \xi_x = -4, \xi_y = +4 \end{array} \right.$ | (D) $\left\{ \begin{array}{l} \delta_0 = \{1,2,3,4,5,6,7,8,9\} \times 10^{-4} \\ dx = 1 \times 10^{-2} \rightarrow \epsilon_x = 3.51547 \times 10^{-6} \\ dy = 1 \times 10^{-2} \rightarrow \epsilon_y = 3.65338 \times 10^{-6} \\ \xi_x = +4, \xi_y = +4 \end{array} \right.$ |

Figure 4.30

Table with the specifics of the sets of simulations performed.

The values of the measured momentum amplitude have been evaluated from the plot of the longitudinal momentum as a function of the number of turns through this formula:

$$\delta_a = \frac{\delta_{a,max} - \delta_{a,min}}{2} \quad (4.59)$$

A model plot from the set of simulations denoted with A is shown in Figure 4.31.

The values of the calculated momentum amplitude squared have been derived from equation (4.19) where the values of  $t_0$  and  $t_1$  have been evaluated from equations (4.32) and (4.33), while the average momentum offset has been evaluated from the plot of the longitudinal momentum as a function of the number of turns as the measured momentum amplitude.

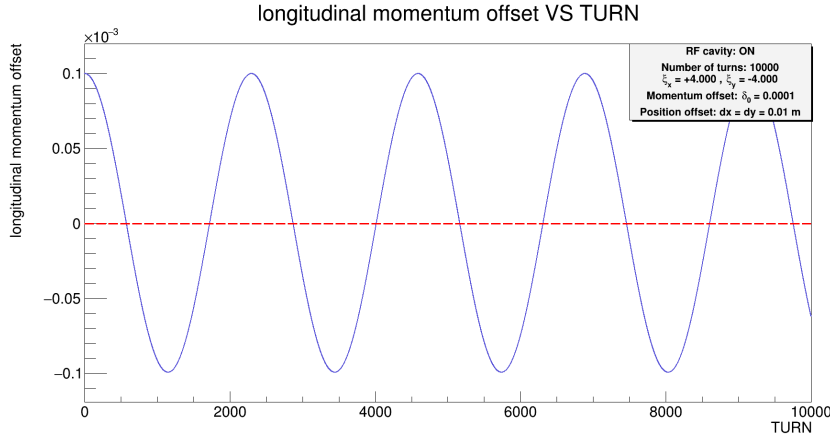


Figure 4.31

Model plot of momentum offset VS number of turns from the set of simulations denoted with A.

The compaction factors used in equations (4.32) and (4.33) are the ones derived from the study of the longitudinal motion contribution in the case of the RF cavity OFF.

The errors on the calculated values of the momentum amplitude squared have been evaluated through the general formula of error propagation:

$$err(\delta_a^2) = \sqrt{\left(\frac{\partial(\delta_a^2)}{\partial t_0} err(t_0)\right)^2 + \left(\frac{\partial(\delta_a^2)}{\partial t_1} err(t_1)\right)^2} \quad (4.60)$$

where:

$$err(t_0) = err(\alpha_0) \quad (4.61)$$

$$err(t_1) = \sqrt{\left(\frac{\partial(t_1)}{\partial \alpha_0} err(\alpha_0)\right)^2 + \left(\frac{\partial(t_1)}{\partial \alpha_1} err(\alpha_1)\right)^2} \quad (4.62)$$

Figure 4.32 shows the plot of both the measured and calculated values of the momentum amplitude squared as a function of the momentum offset for the set of simulations denoted with A.

The match between the measured and calculated values is not so accurate as in the case of the RF cavity OFF because there are higher order effects which have been neglected and which probably play an important role in the derivation of the calculated momentum amplitude squared formula and, as a consequence, also in the error propagation.

However, Figure 4.32 suggests the validity of equation (4.19) for the hybrid storage ring in the case of the RF cavity ON.

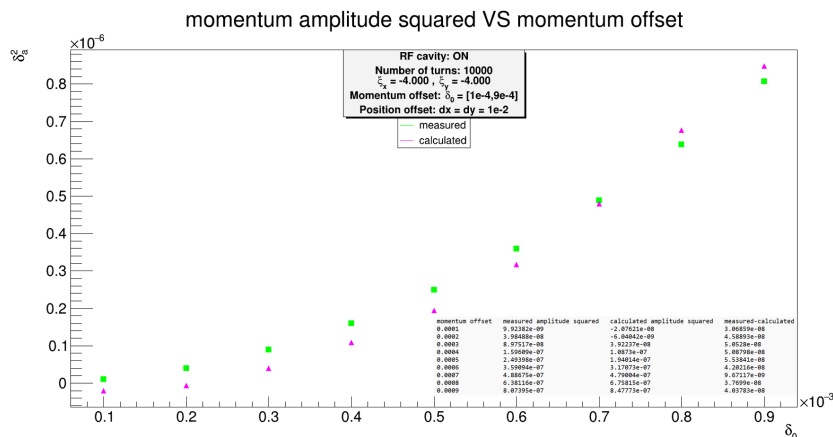


Figure 4.32

Plot of measured and calculated momentum amplitude squared VS momentum offset for the set of simulations denoted with A.

The plots for the other non-mentioned sets of simulations are reported in the Appendix D.



# Conclusions

The second half of the last century was marked by many important insights and discoveries in the field of particle physics, first and foremost the development of the Standard Model (SM). However, there are many open questions this model cannot answer; one of them is the baryon asymmetry, i.e. the dominance of matter over antimatter in the Universe.

According to the most accredited theory, the responsible mechanism, called baryogenesis, required the fulfilment of certain necessary conditions within the first moments of the Universe following the Big Bang; the most significant one is the violation of the charge conjugation-parity (CP) symmetry.

The SM predicted value for the asymmetry parameter, which quantifies the baryon asymmetry, is 8 orders of magnitude smaller than the measured one: this means that the SM contributions to CP violation are too weak to explain baryon asymmetry and new sources of CP violation beyond the SM are needed.

The SM is not the ultimate theory of particle physics and among all those developed by theoreticians one of the most plausible extensions, at least till now, is the SuperSymmetry (SUSY) theory. Concerning the baryon asymmetry problem, its characteristic of interest is that the many particle-particle interactions provide more CP violation mechanisms and a non-zero Electric Dipole Moment (EDM) which can be experimentally accessed.

The observation of non-zero EDMs would represent a possible answer to the unsolved problem of baryon asymmetry as well as a clear sign of New Physics beyond the SM.

Very recently a new class of experiments has been proposed to directly measure the EDMs of charged particles via storage rings. In particular, an experimental staged program is presently pursued by the JEDI collaboration at the Forschungszentrum-Jülich in Germany.

The first stage consists in exploiting the Cooler Synchrotron (COSY) to perform feasibility studies on a stored beam of polarized deuterons, the second one deals with construction of a Prototype Storage Ring (PSR) to study the critical features and to develop the key technologies and the last one plans to the construction of the pure electric storage ring to provide the first ever proton EDM (pEDM) measurement.

---

The main advantages in using a pure electric storage ring are the possibility to improve the statistics increasing the luminosity of the experiment, the simultaneous circulation of two counter-rotating particle beams to properly address and control different sources of systematic errors and the absence of magnetic fields which allows to maximize the precision of the measurement inhibiting one of the main sources of systematic errors.

Aim of this thesis was to perform beam dynamics simulations at the hybrid storage ring which is one the proposed lattices for the last stage of the JEDI experiment.

Objected of the beam dynamics simulations performed was the need to verify whether the current theoretical knowledge about storage rings, which is known to be valid in the case of pure magnetic ones, could also be applied in the case of other types of storage rings, in particular the hybrid storage ring which is characterized by an electric confinement system. For all the simulations performed the single particle tracking has been considered.

Two aspects have been studied: the  $6 \times 6$  transfer matrix and the path lengthening.

The study of the 6D phase space through the  $6 \times 6$  transfer matrix is important because it allows to study the couplings strengths between different phase spaces.

The reason why the study of the path lengthening is very important is that it directly influences the spin tune spread through the change in particle velocities and in turn the spin tune spread directly influences the spin coherence time (SCT) which is related to the beam polarization lifetime of the particle beam and represents the time available to measure the EDM signal.

The experimental results coming from the data analysis on the sets of simulations performed have confirmed that the couplings strengths between different phase spaces in the case of the hybrid storage ring are the same as the ones for pure magnetic storage rings, as well as the formula for the path lengthening which is known to be valid for pure magnetic storage rings appears to be valid also in the case of the hybrid storage ring both in the case of the RF cavity OFF and ON with some regards in the second case.

This thesis work paves the way for additional deepening on the following aspects:

- the introduction of higher order effects to better study the path lengthening in the case of the RF ON;
- the realization of new sets of beam dynamics simulations to test other aspects which for the moment are known to be valid only for pure magnetic storage rings and thus increasing the knowledge about the behaviour of the hybrid storage ring;

- the realization of spin dynamics simulations to study the strictly connected quantities to the EDM measurement (e.g., change in the spin tune, spin resonances, and spin decoherence);
- the realization of beam tracking to study the behaviour of the entire particle beam;
- the study of the most significant systematic error sources.

The hybrid storage ring aims to be the foundational basis for the pEDM experiment.



# Appendix A1

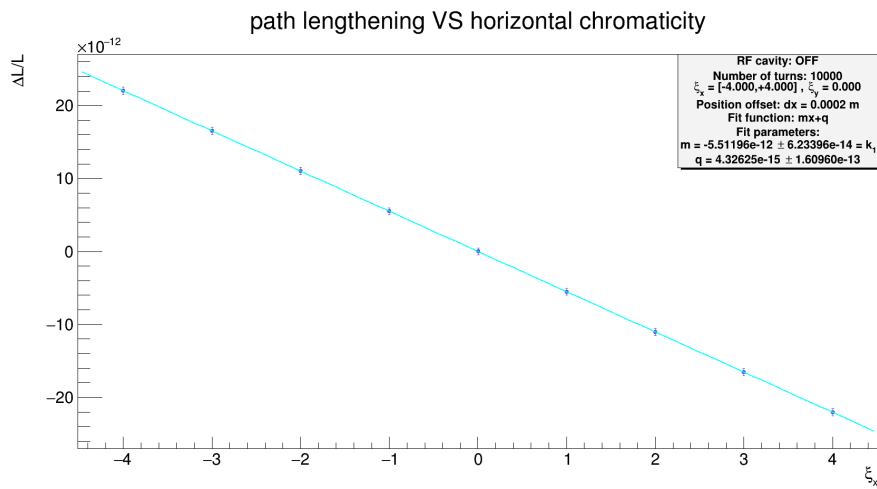


Figure A1

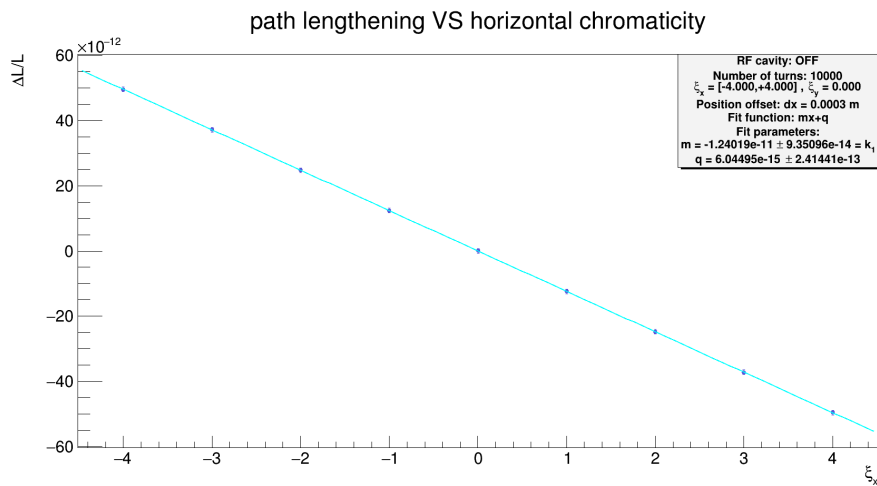


Figure A2

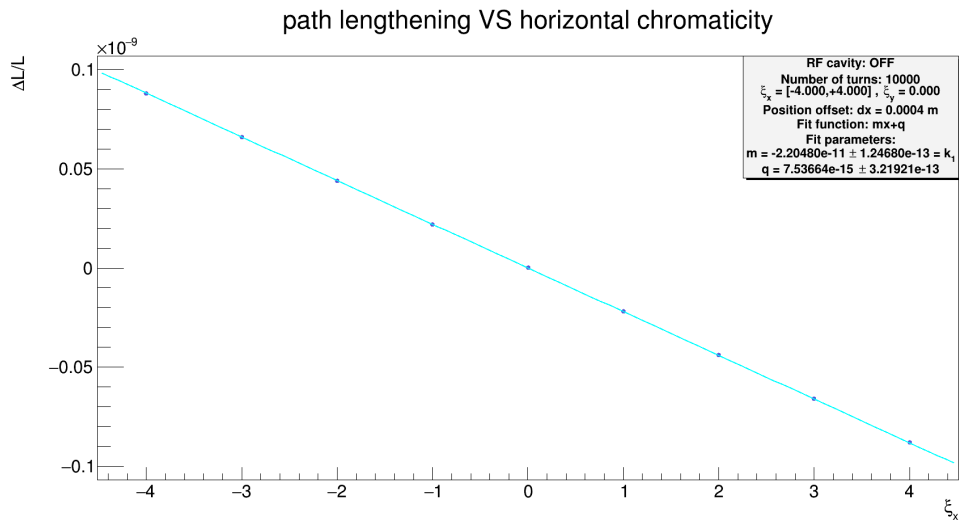


Figure A3

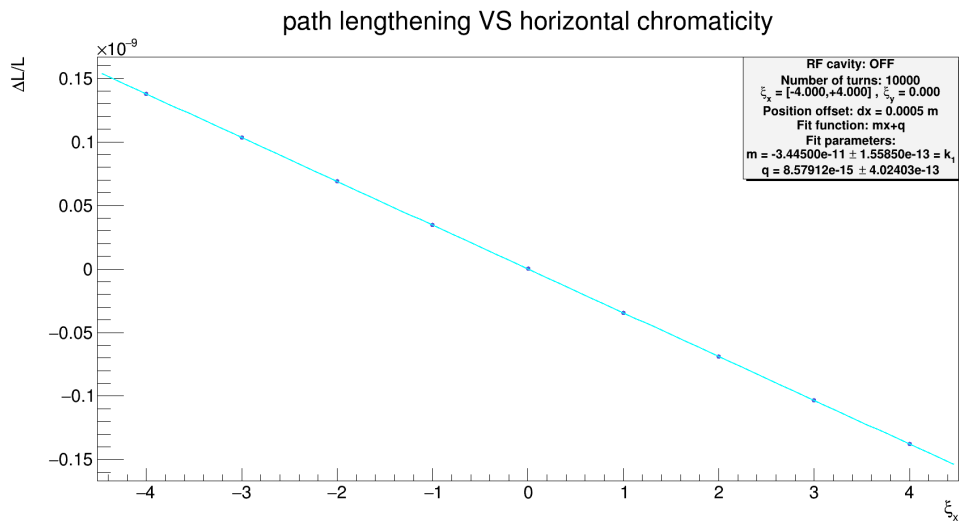


Figure A4

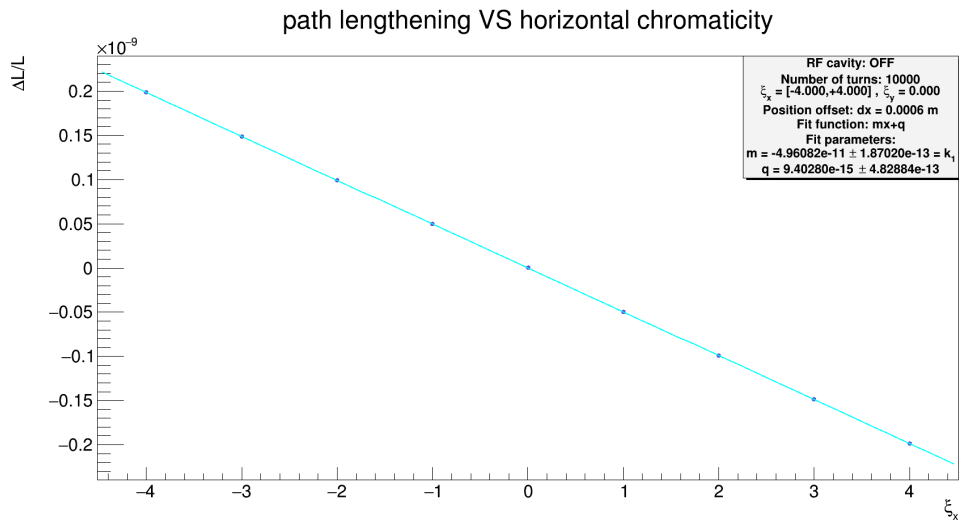


Figure A5

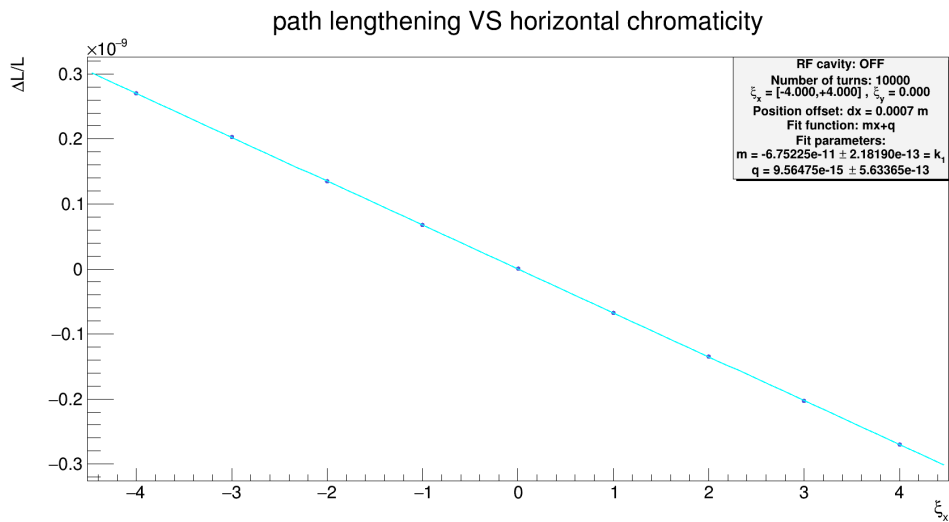


Figure A6

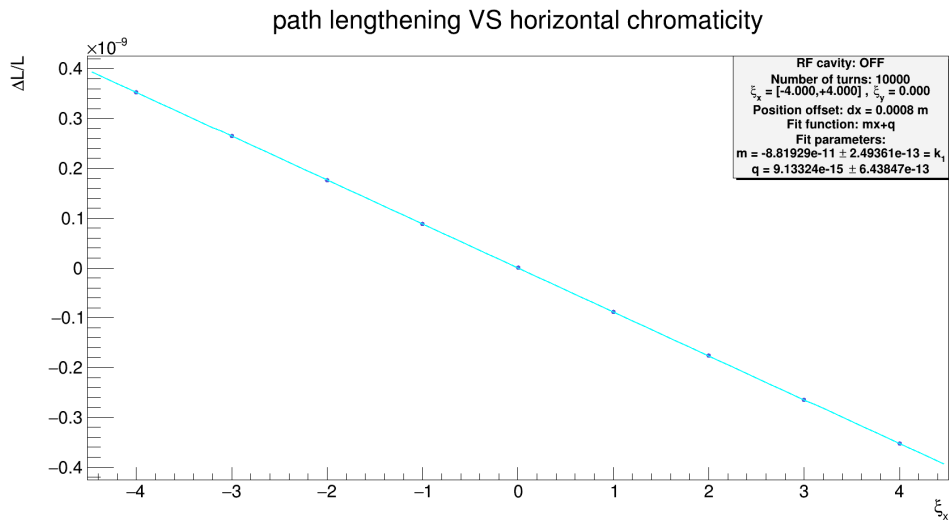


Figure A7

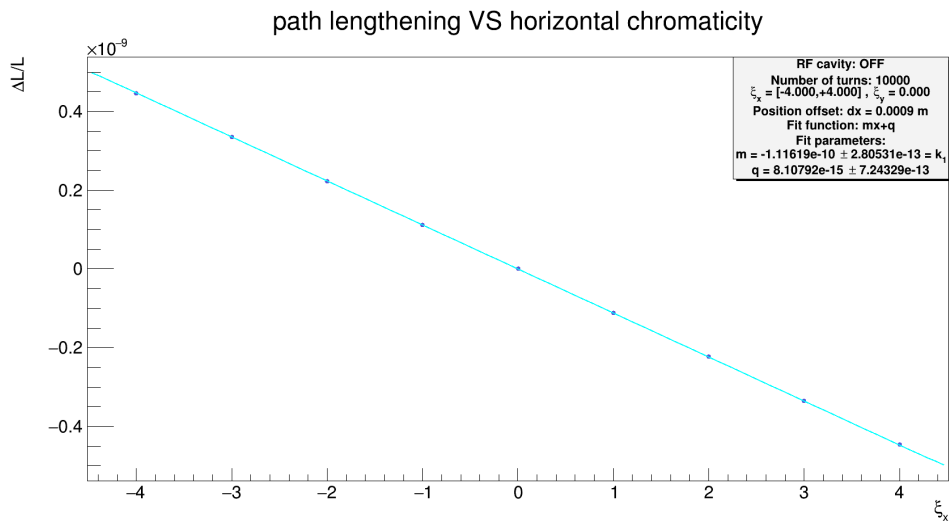


Figure A8



# Appendix A2

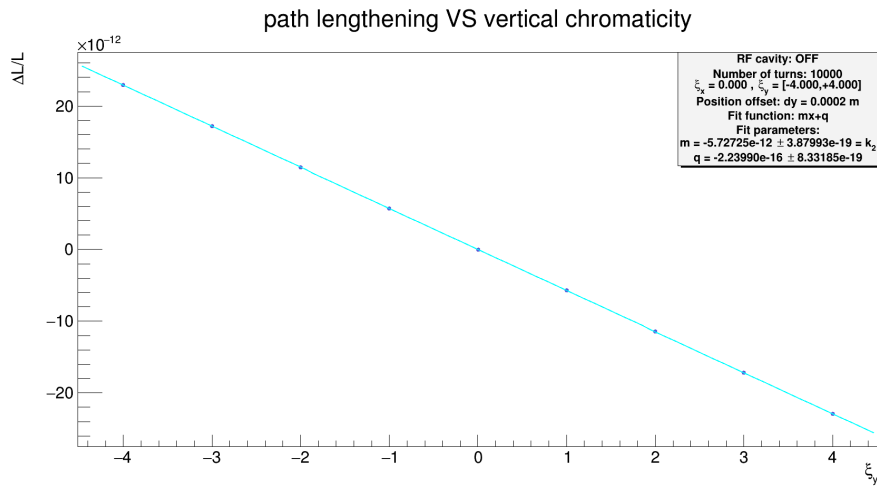


Figure A9

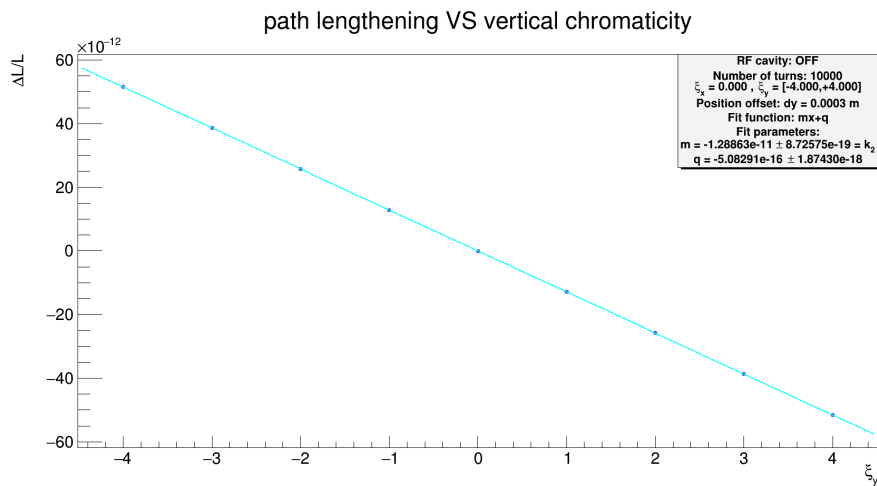


Figure A10

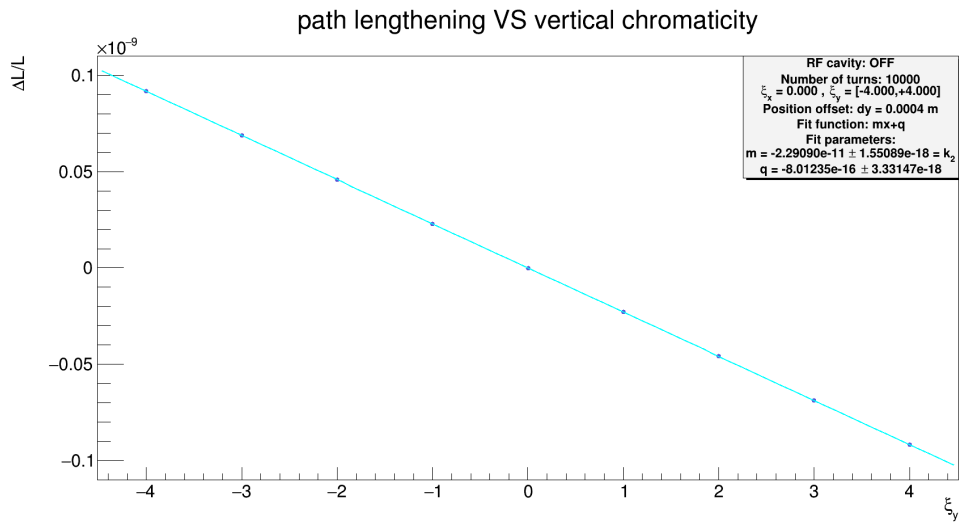


Figure A11

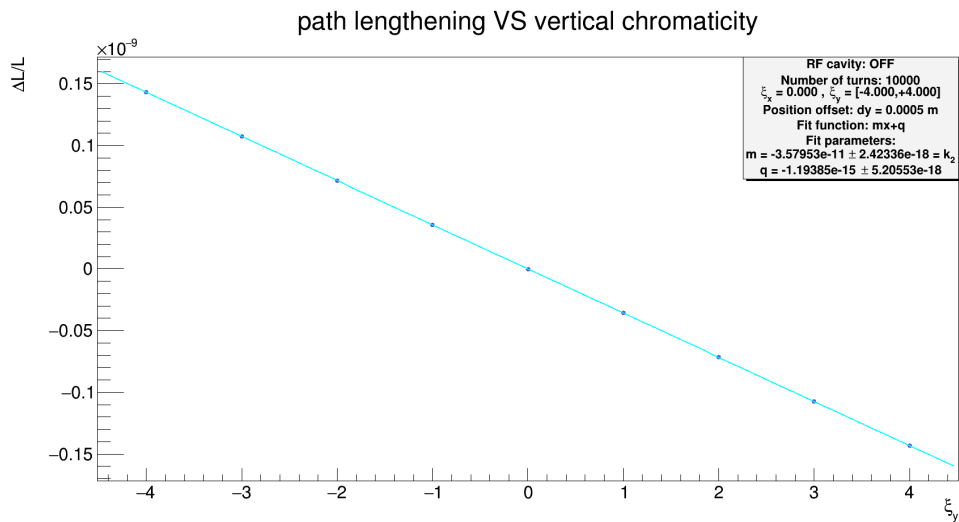


Figure A12

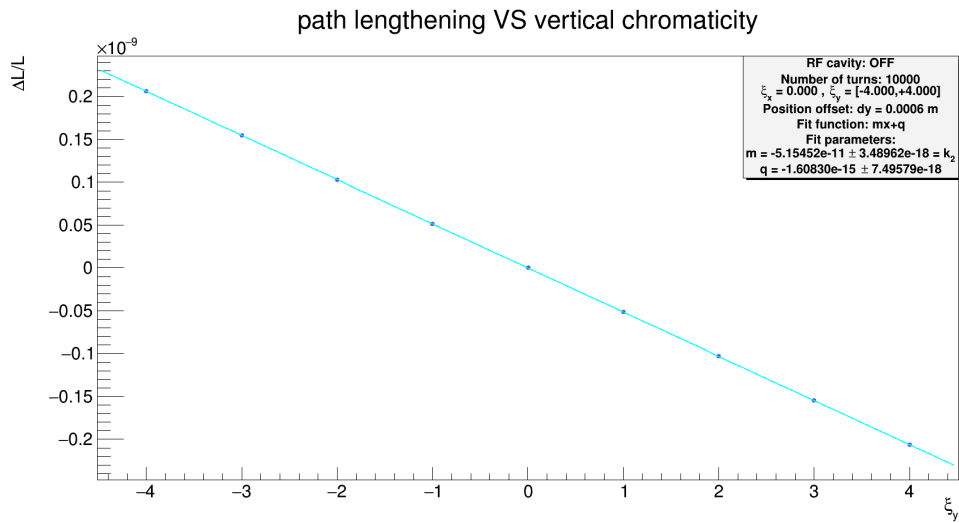


Figure A13

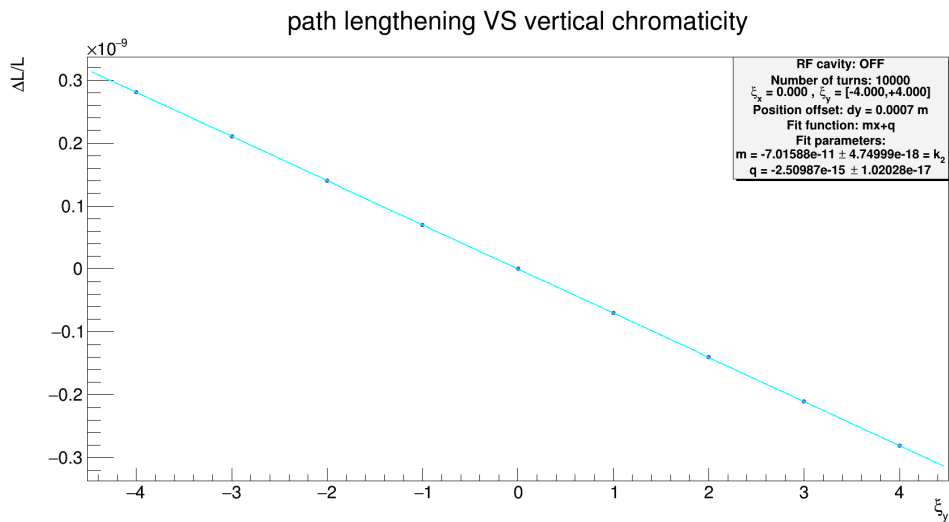


Figure A14

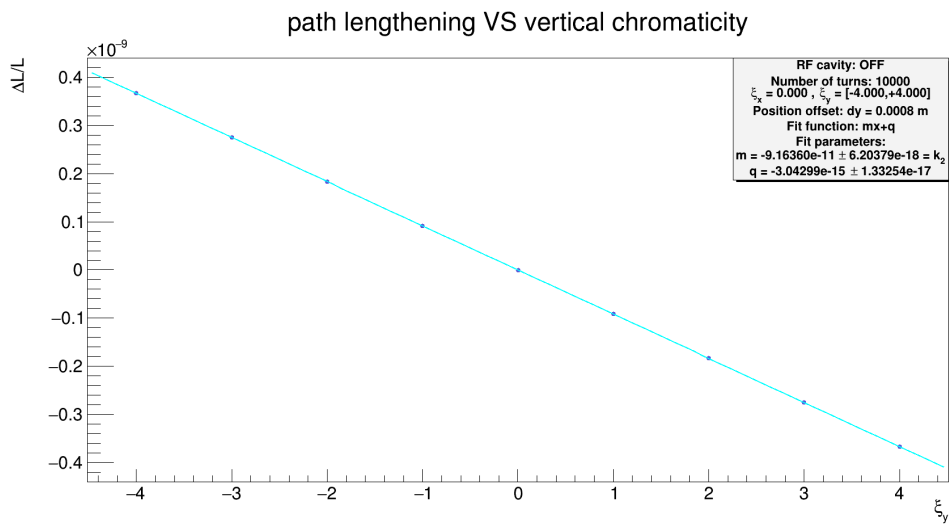


Figure A15

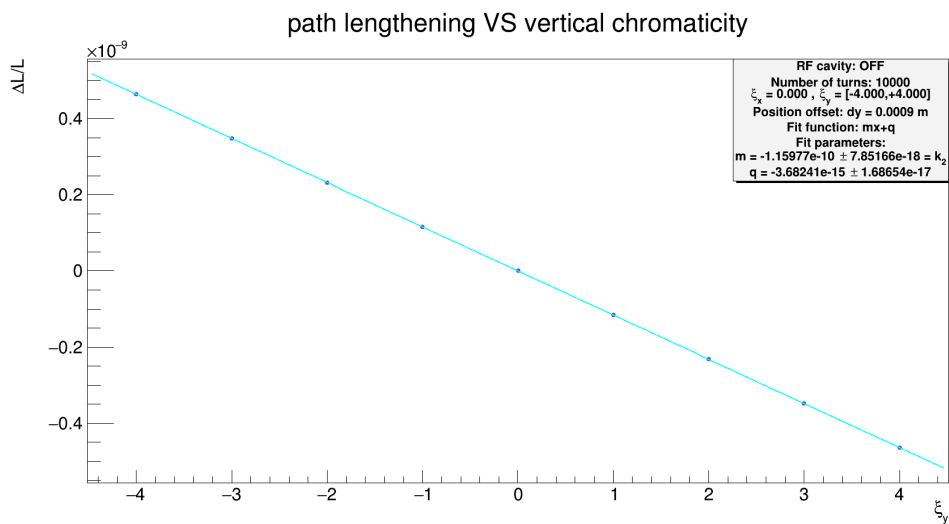


Figure A16

# Appendix B1

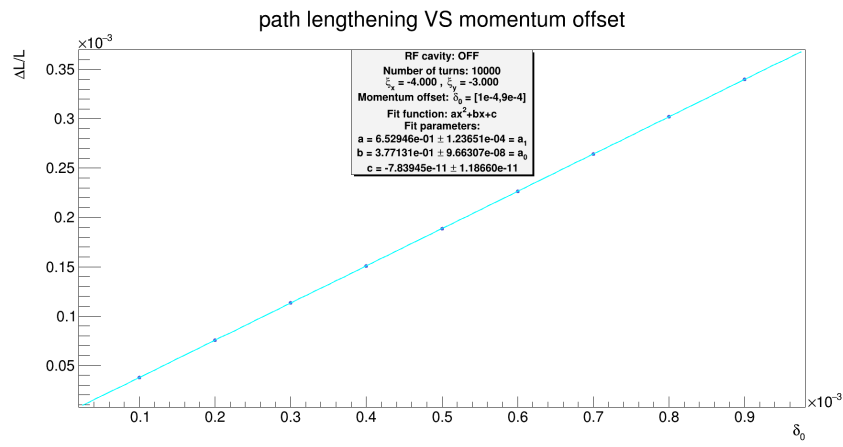


Figure B1

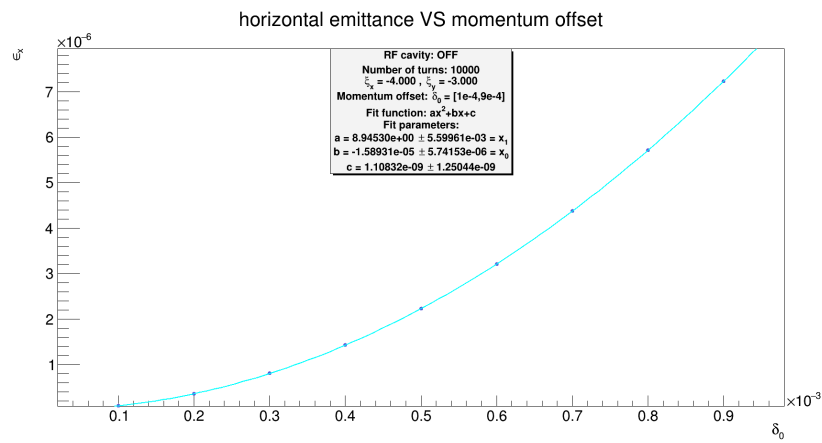


Figure B2

|            |                                       |
|------------|---------------------------------------|
| $\alpha_0$ | $0.377131 \pm 1.32056 \times 10^{-7}$ |
| $\alpha_1$ | $0.512714 \pm 1.61542 \times 10^{-4}$ |

Figure B3

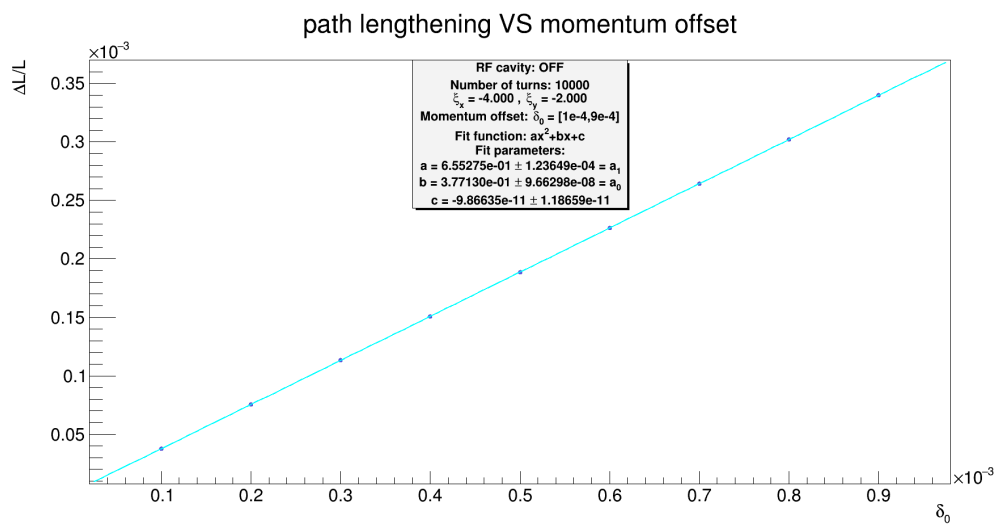


Figure B4

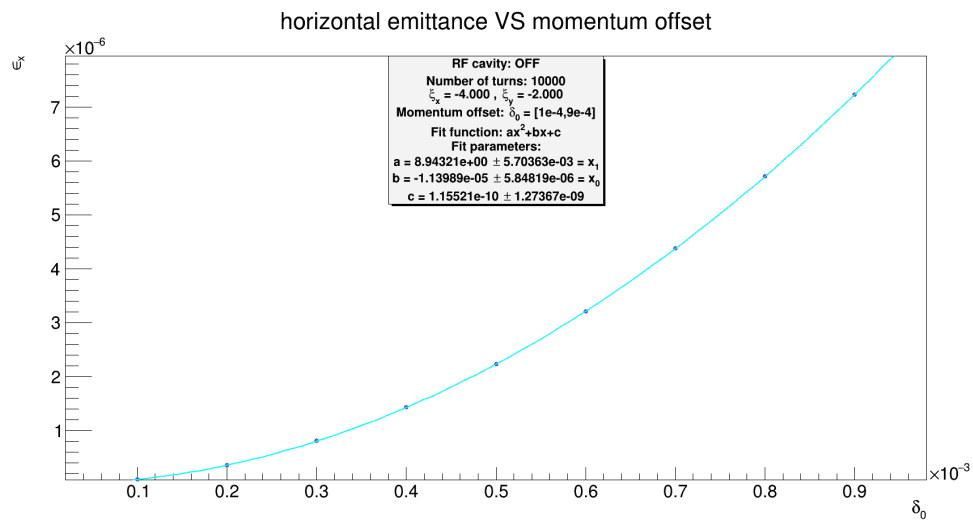


Figure B5

|            |                                       |
|------------|---------------------------------------|
| $\alpha_0$ | $0.377131 \pm 1.33201 \times 10^{-7}$ |
| $\alpha_1$ | $0.515076 \pm 1.52591 \times 10^{-4}$ |

Figure B6

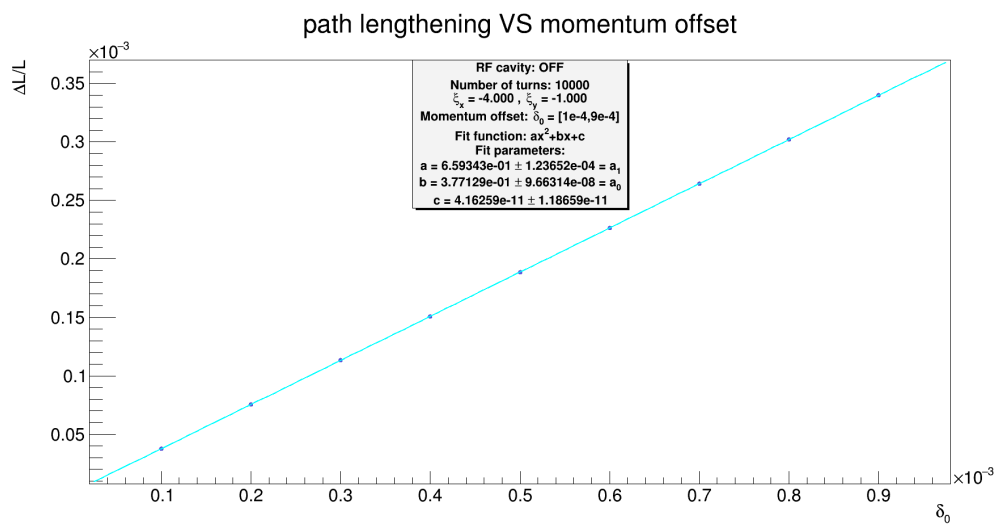


Figure B7

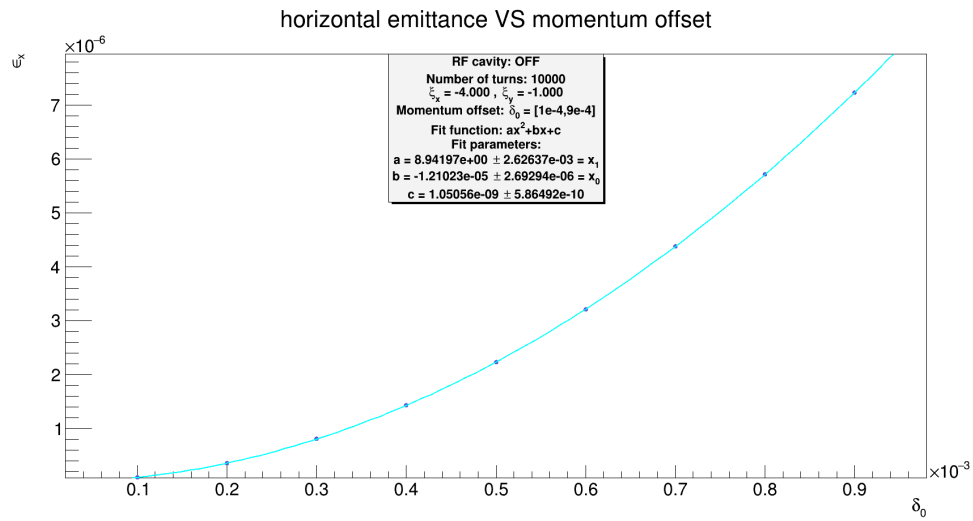


Figure B8

|            |                                       |
|------------|---------------------------------------|
| $\alpha_0$ | $0.377129 \pm 1.05451 \times 10^{-7}$ |
| $\alpha_1$ | $0.519163 \pm 1.30327 \times 10^{-4}$ |

Figure B9

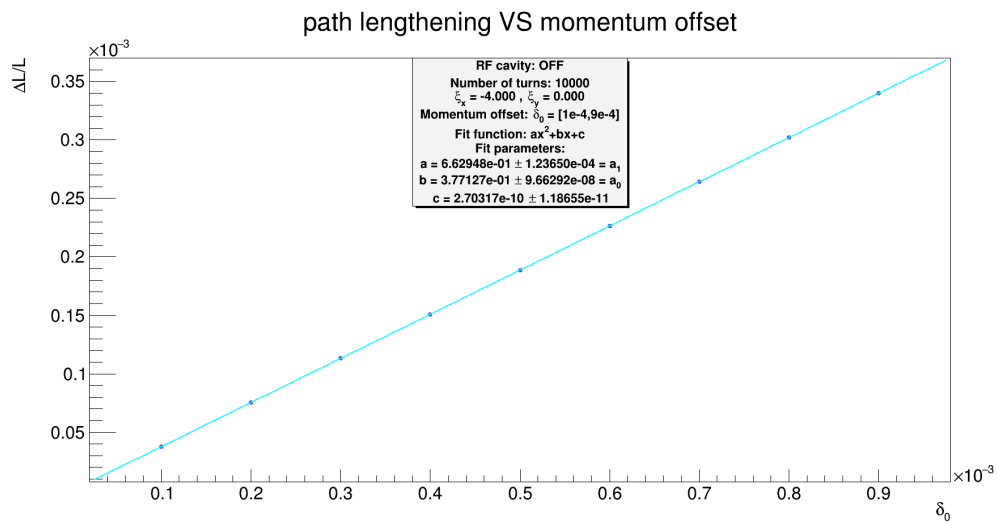


Figure B10

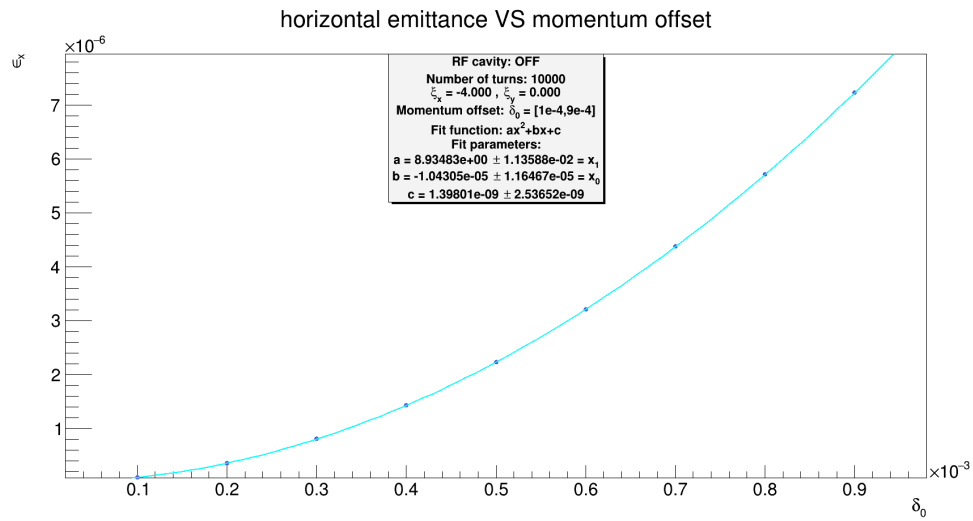


Figure 11

|            |                                       |
|------------|---------------------------------------|
| $\alpha_0$ | $0.377127 \pm 2.06574 \times 10^{-7}$ |
| $\alpha_1$ | $0.522880 \pm 2.16789 \times 10^{-4}$ |

Figure B12



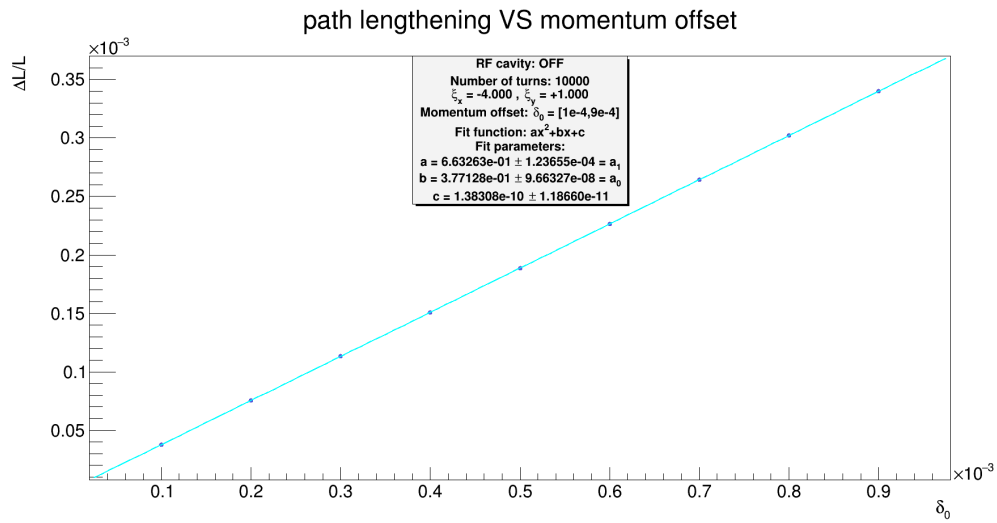


Figure B13

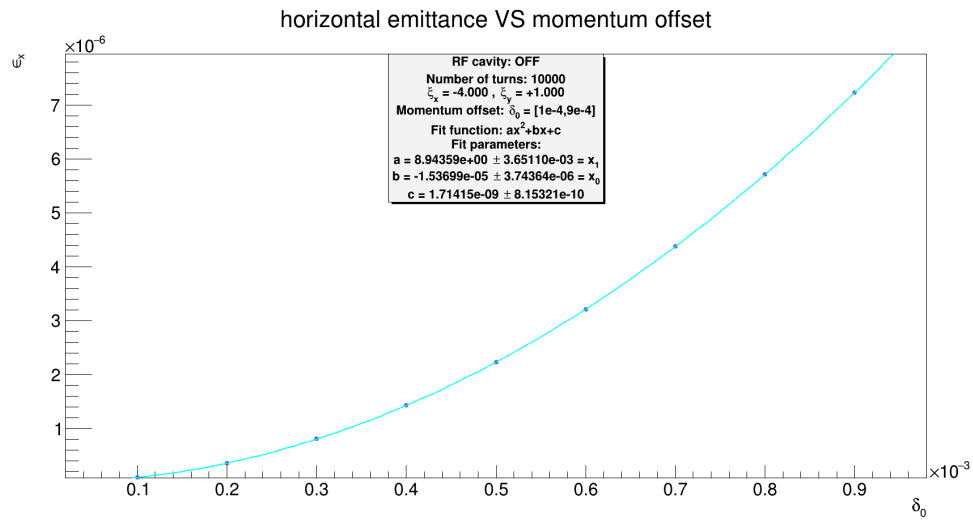


Figure B14

|            |                                       |
|------------|---------------------------------------|
| $\alpha_0$ | $0.377128 \pm 1.13058 \times 10^{-7}$ |
| $\alpha_1$ | $0.523058 \pm 1.36259 \times 10^{-4}$ |

Figure B15

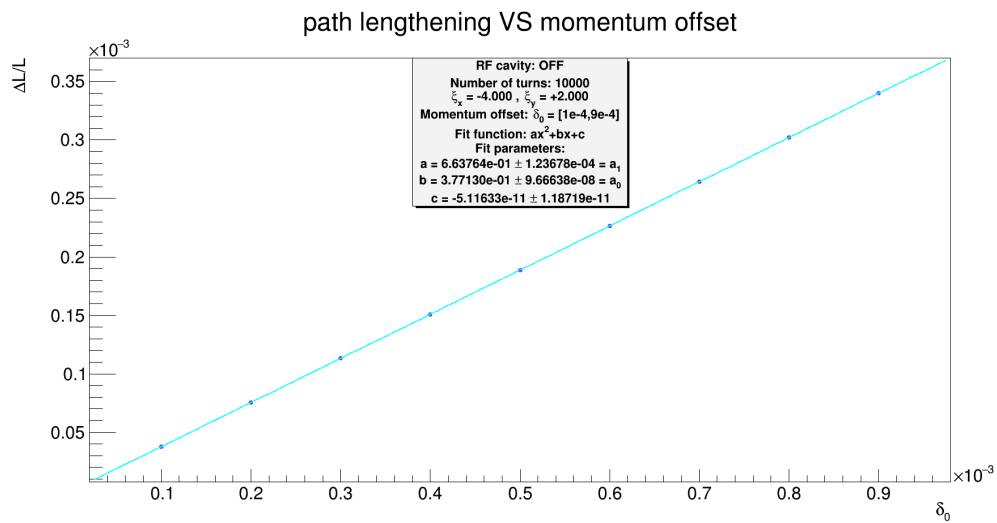


Figure B16

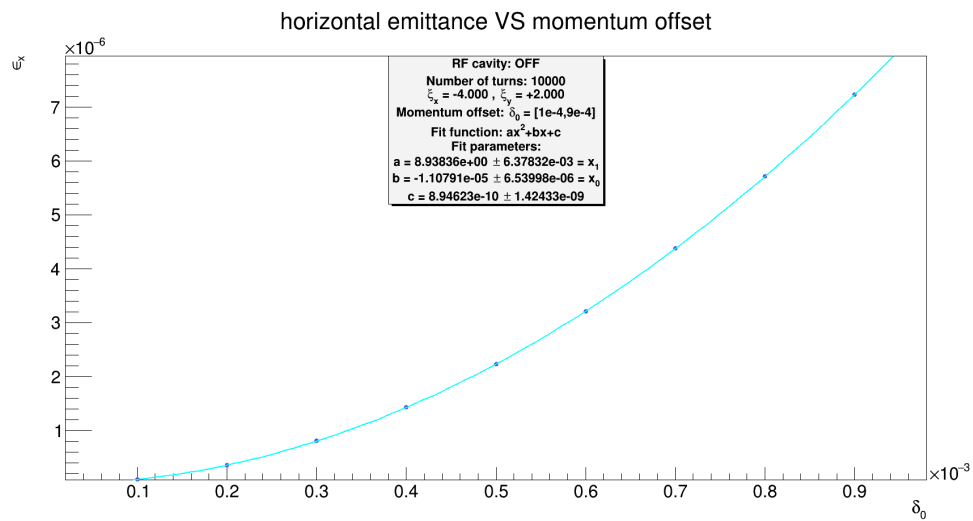


Figure B17

|            |                                       |
|------------|---------------------------------------|
| $\alpha_0$ | $0.377130 \pm 1.40909 \times 10^{-7}$ |
| $\alpha_1$ | $0.523641 \pm 1.59042 \times 10^{-4}$ |

Figure B18

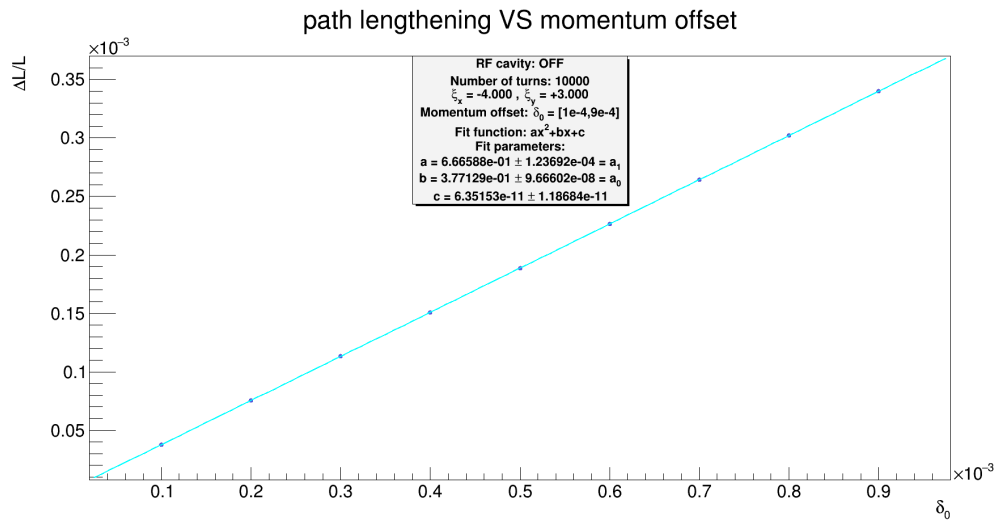


Figure B19

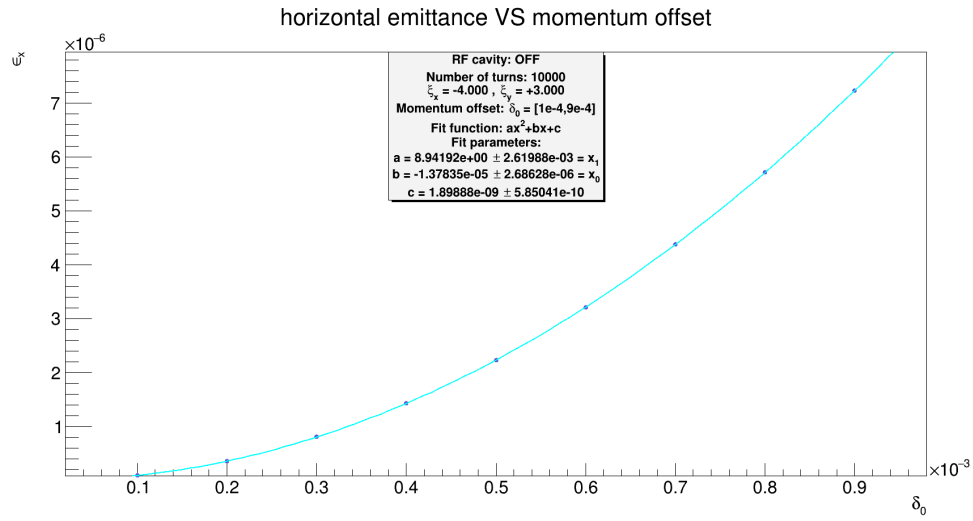


Figure B20

|            |                                       |
|------------|---------------------------------------|
| $\alpha_0$ | $0.377129 \pm 1.05435 \times 10^{-7}$ |
| $\alpha_1$ | $0.526409 \pm 1.30332 \times 10^{-4}$ |

Figure B21

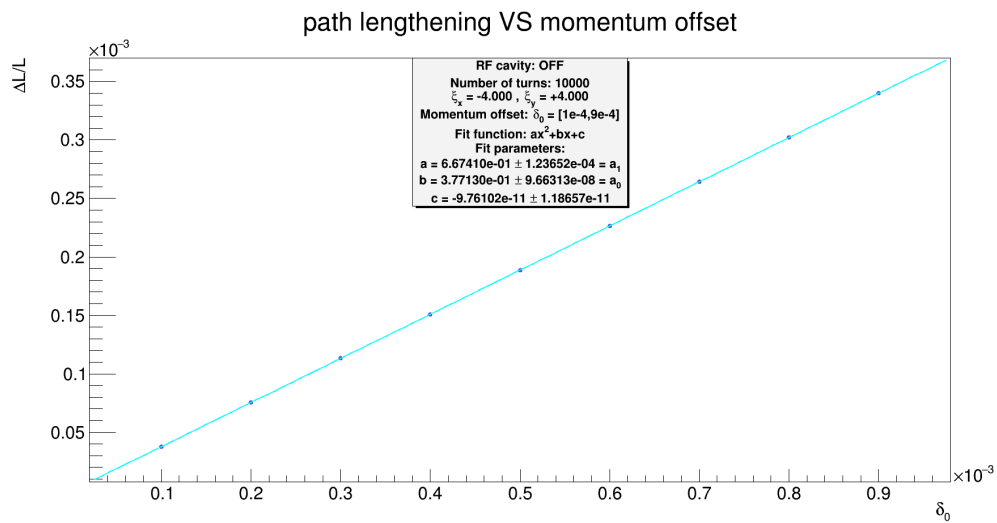


Figure B22

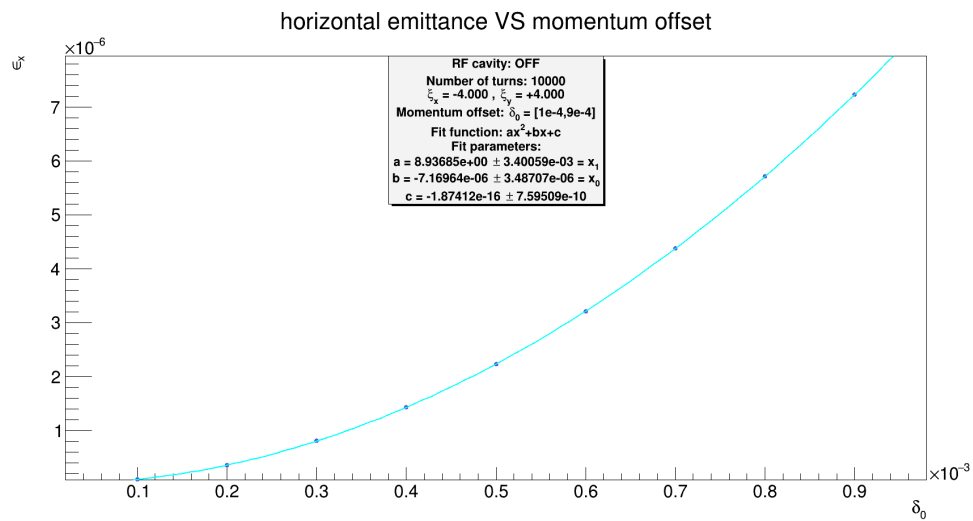


Figure B23

|            |                                       |
|------------|---------------------------------------|
| $\alpha_0$ | $0.377130 \pm 1.11022 \times 10^{-7}$ |
| $\alpha_1$ | $0.527310 \pm 1.34654 \times 10^{-4}$ |

Figure B24

# Appendix B2

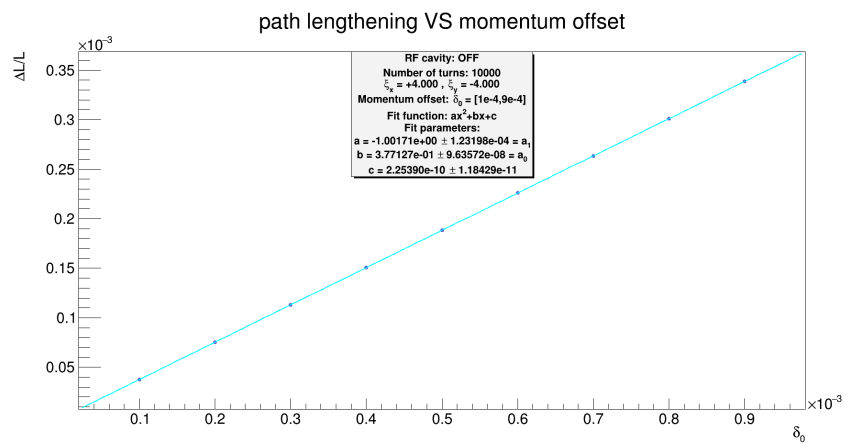


Figure B25

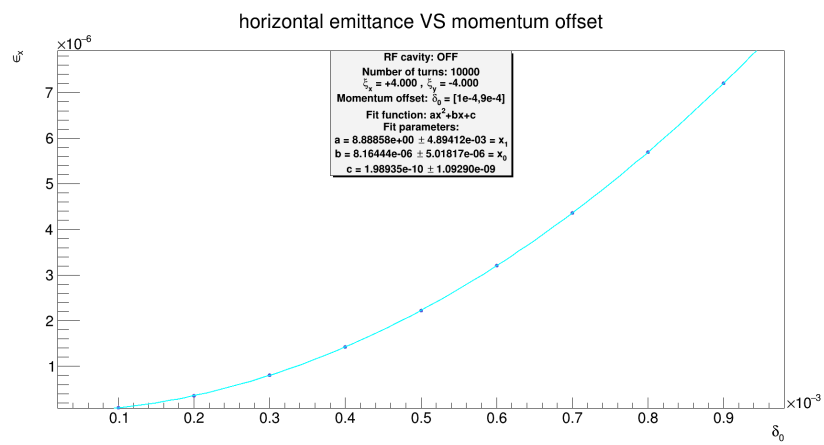
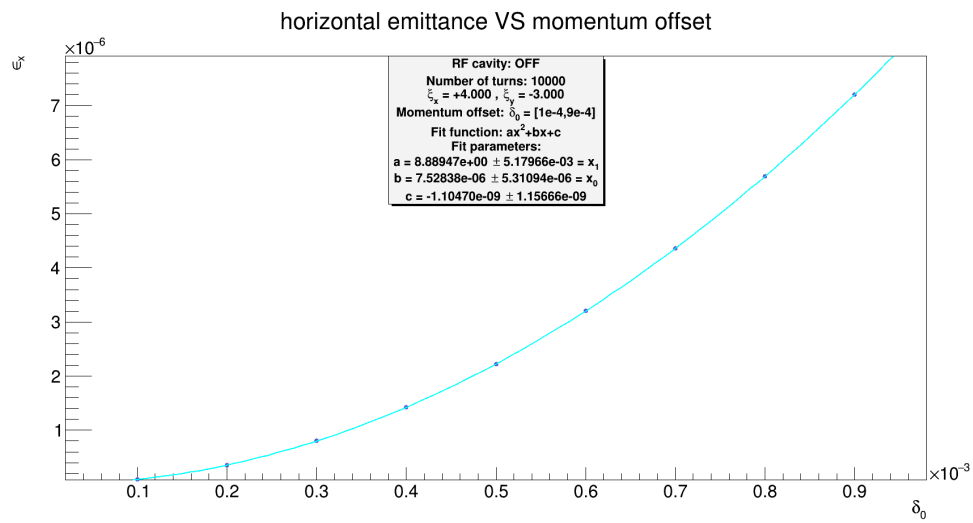
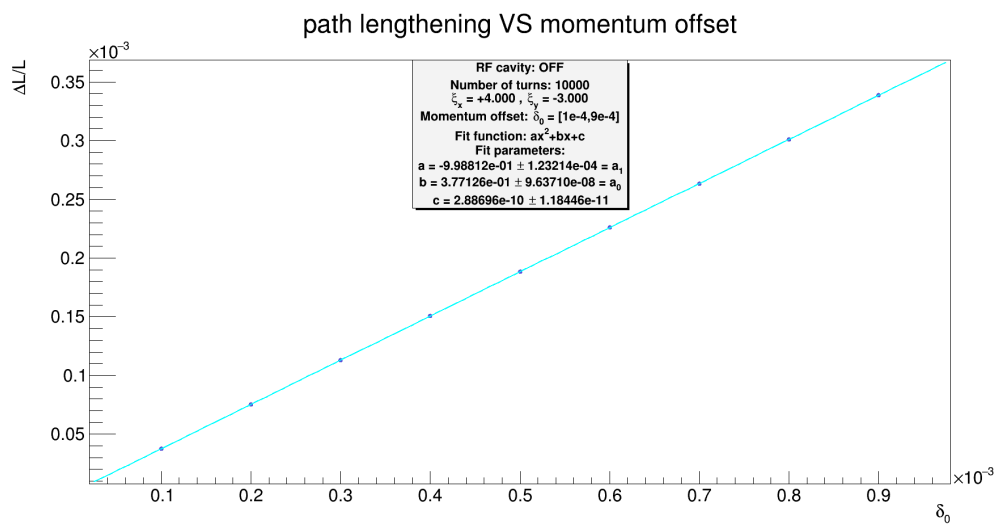


Figure B26

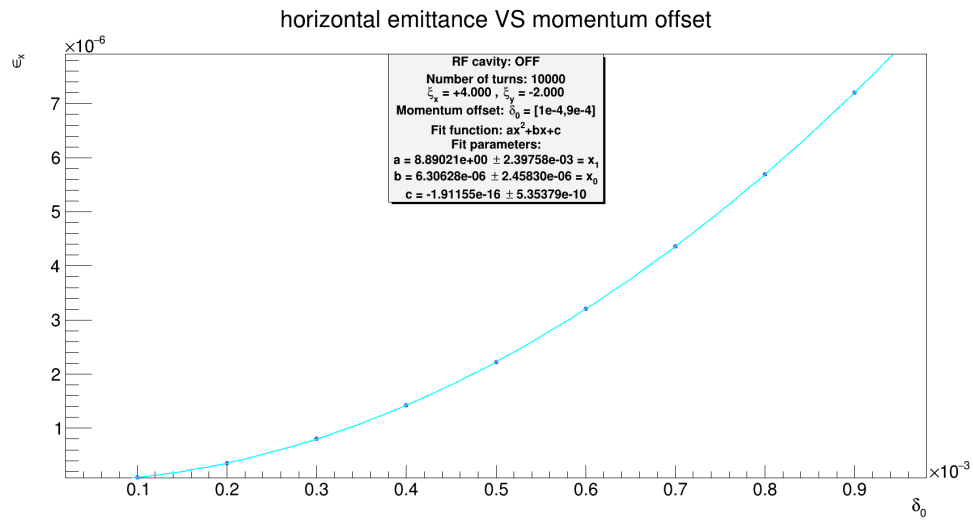
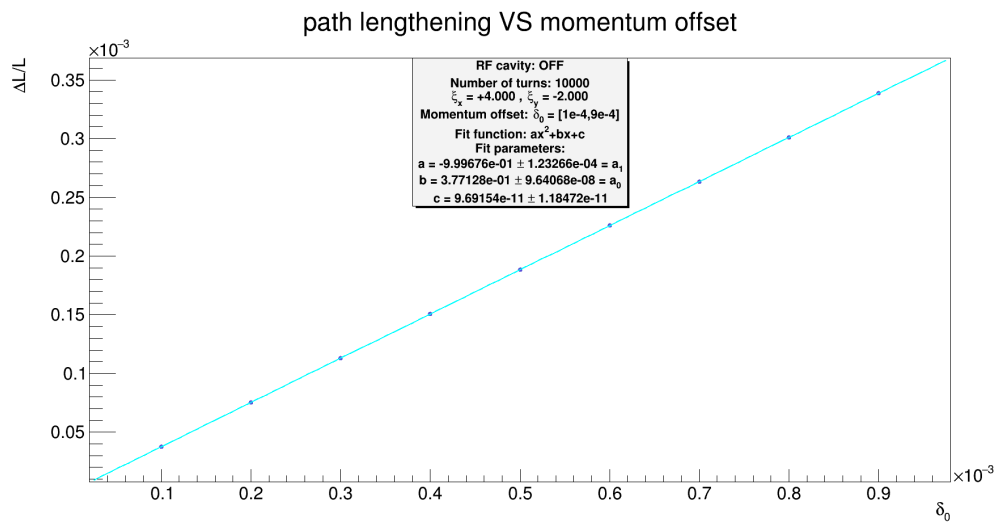
|            |  |
|------------|--|
| $\alpha_0$ | $0.377127 \pm 1.24392 \times 10^{-7}$  |
| $\alpha_1$ | $-0.862367 \pm 1.45135 \times 10^{-4}$ |

Figure B27



|            |  |
|------------|--|
| $\alpha_0$ | $0.377126 \pm 1.27355 \times 10^{-7}$  |
| $\alpha_1$ | $-0.859455 \pm 1.47564 \times 10^{-4}$ |

Figure B30



|            |  |
|------------|--|
| $\alpha_0$ | $0.377128 \pm 1.03824 \times 10^{-7}$  |
| $\alpha_1$ | $-0.860308 \pm 1.28869 \times 10^{-4}$ |

Figure B33

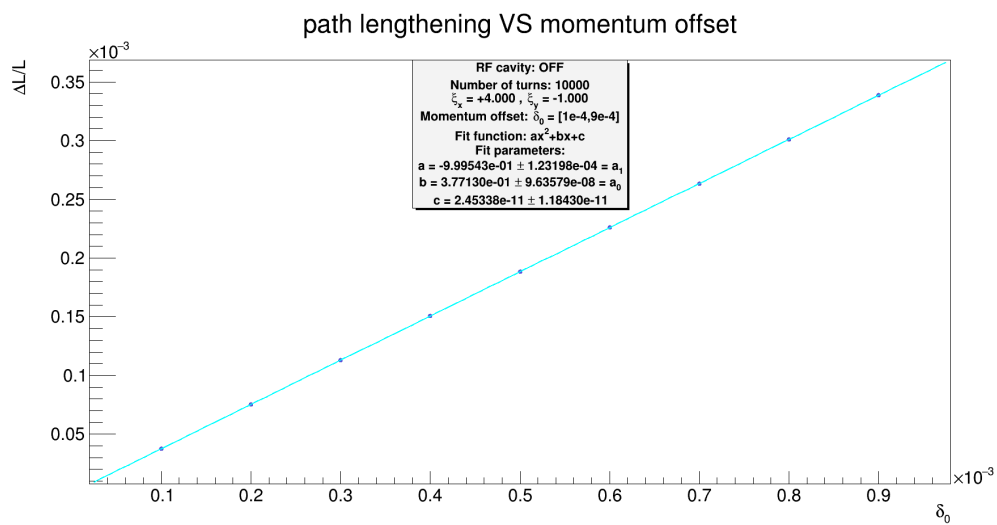


Figure B34

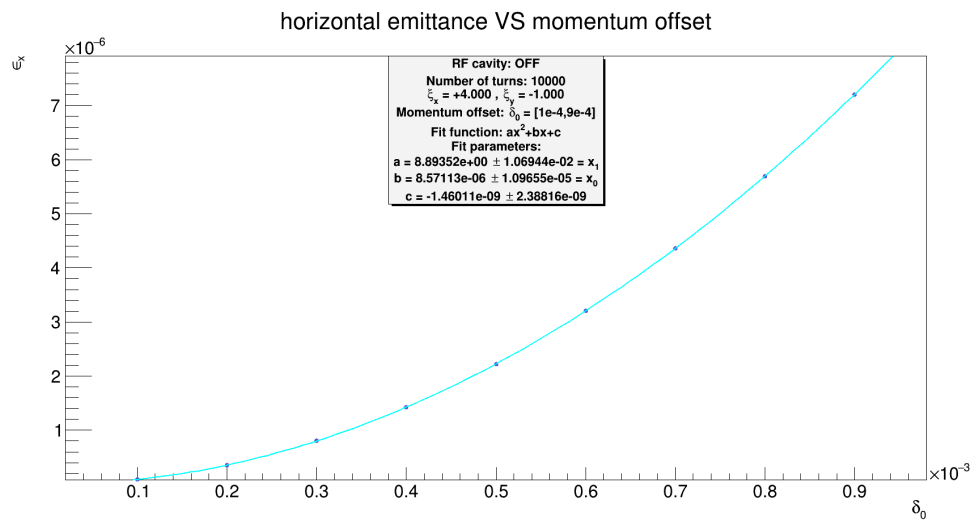


Figure B35

|            |  |
|------------|--|
| $\alpha_0$ | $0.377130 \pm 1.97066 \times 10^{-7}$  |
| $\alpha_1$ | $-0.860123 \pm 2.08050 \times 10^{-4}$ |

Figure B36



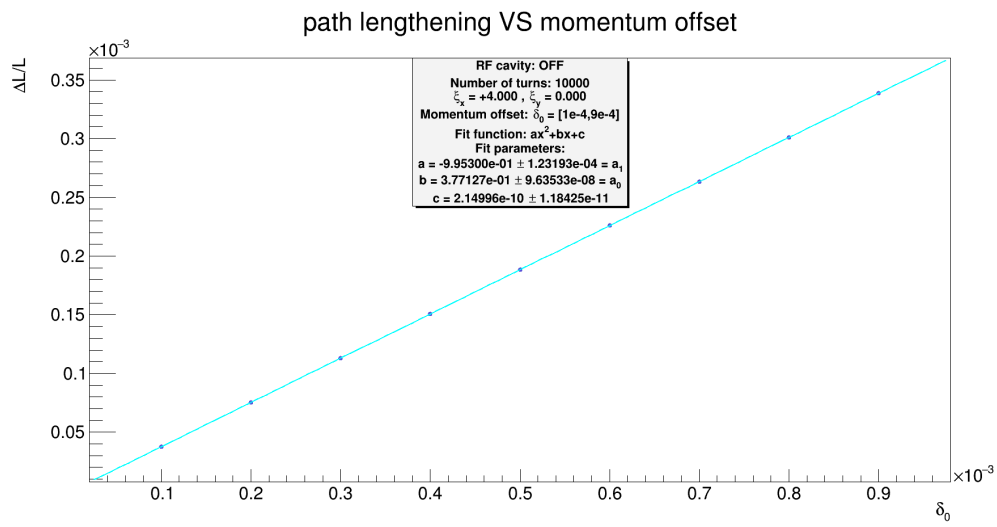


Figure B37

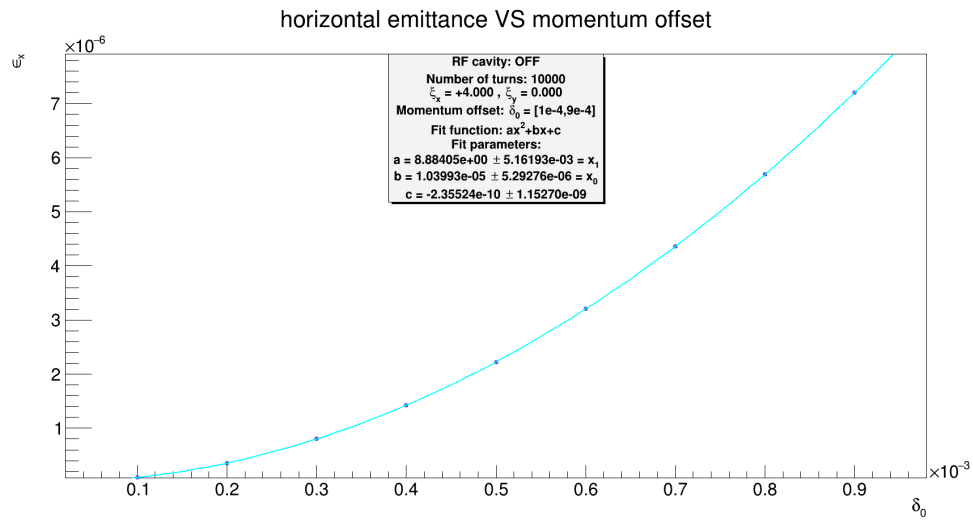


Figure B38

|            |  |
|------------|--|
| $\alpha_0$ | $0.377127 \pm 1.27155 \times 10^{-7}$  |
| $\alpha_1$ | $-0.856028 \pm 1.47393 \times 10^{-4}$ |

Figure B39

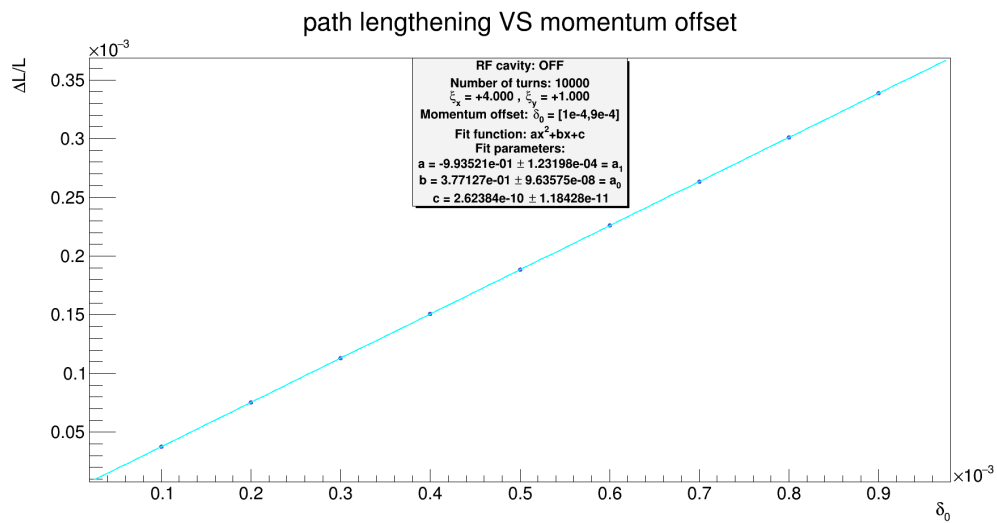


Figure B40

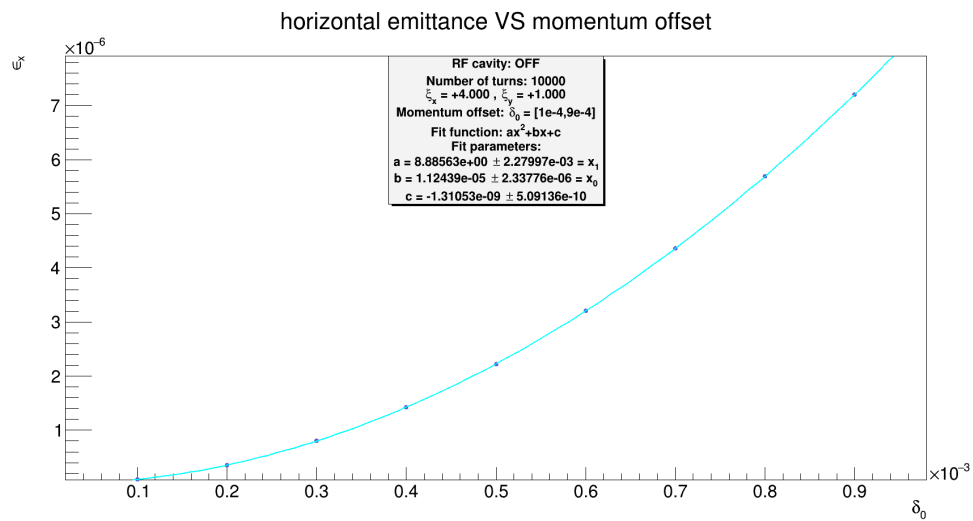


Figure B41

|            |  |
|------------|--|
| $\alpha_0$ | $0.377127 \pm 1.03091 \times 10^{-7}$  |
| $\alpha_1$ | $-0.854224 \pm 1.28278 \times 10^{-4}$ |

Figure B42

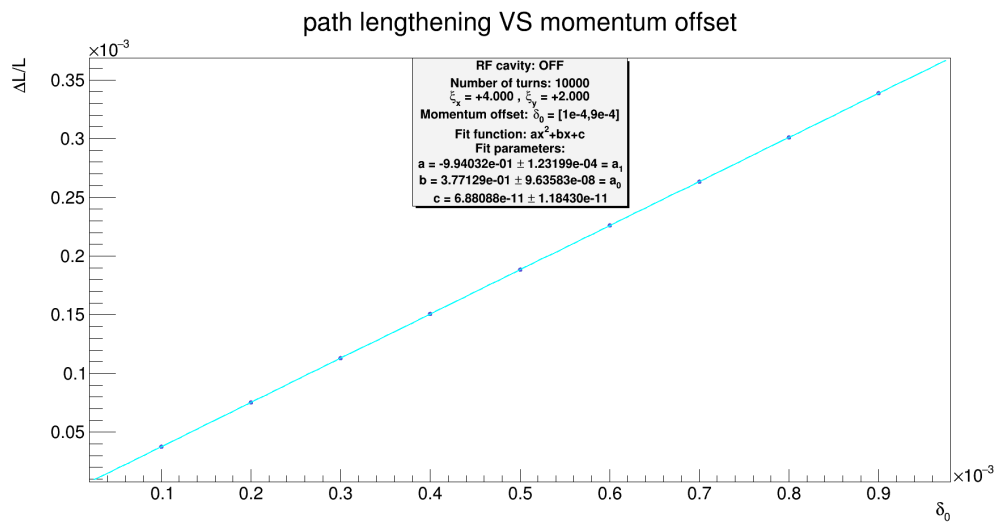


Figure B43

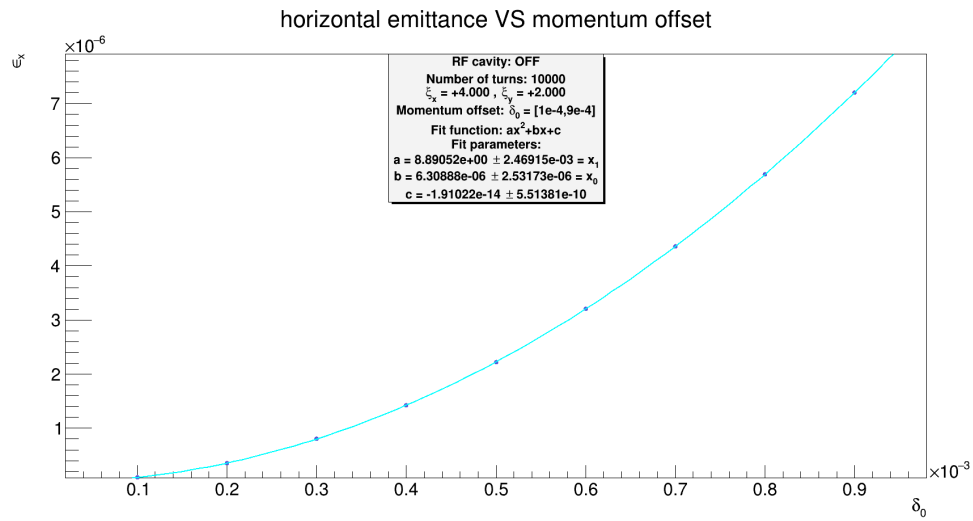


Figure B44

|            |  |
|------------|--|
| $\alpha_0$ | $0.377129 \pm 1.04212 \times 10^{-7}$  |
| $\alpha_1$ | $-0.854659 \pm 1.29237 \times 10^{-4}$ |

Figure B45

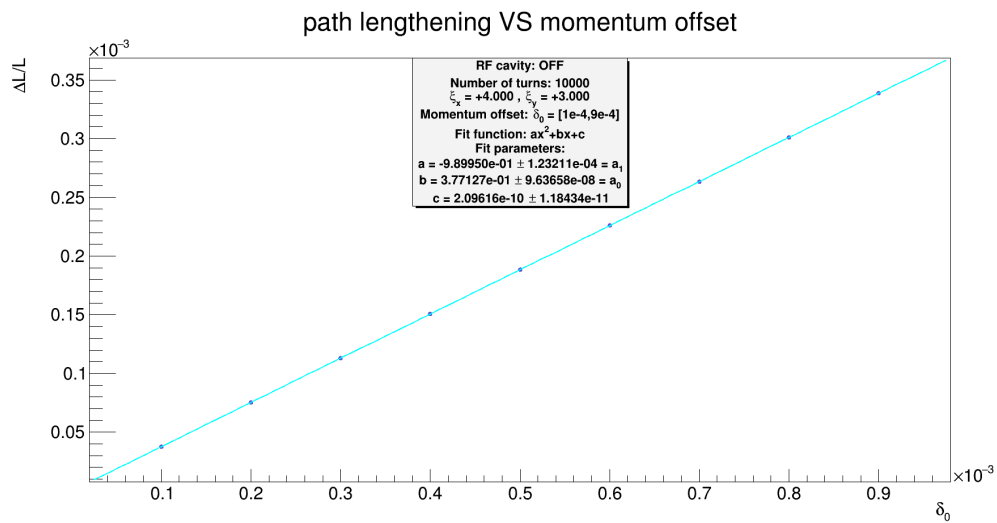


Figure B46

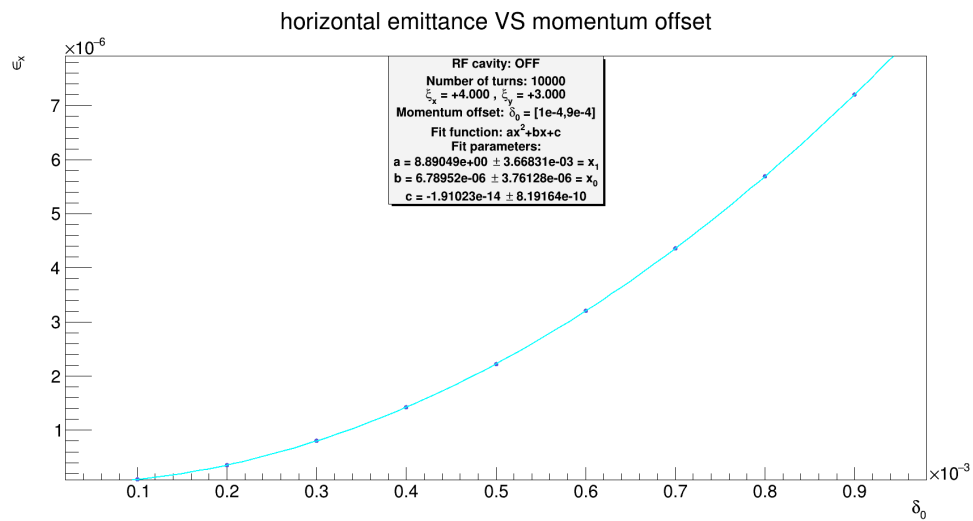


Figure B47

|            |  |
|------------|--|
| $\alpha_0$ | $0.377127 \pm 1.12974 \times 10^{-7}$  |
| $\alpha_1$ | $-0.850577 \pm 1.35970 \times 10^{-4}$ |

Figure B48

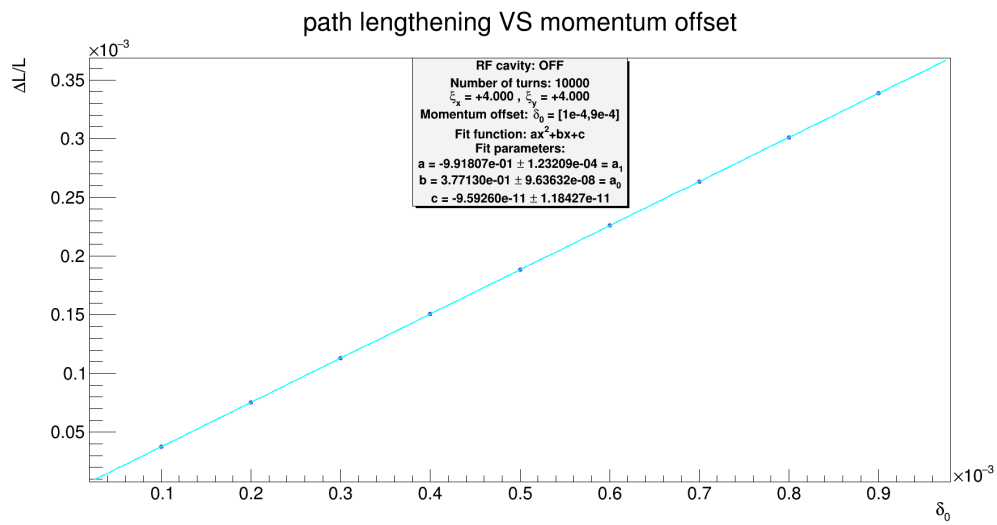


Figure B49

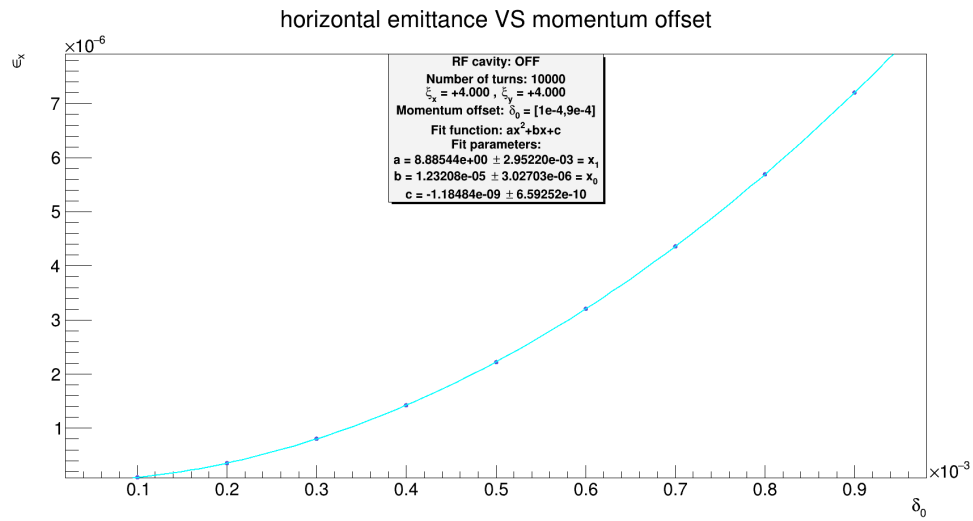


Figure B50

|            |  |
|------------|--|
| $\alpha_0$ | $0.377130 \pm 1.07414 \times 10^{-7}$  |
| $\alpha_1$ | $-0.852513 \pm 1.31614 \times 10^{-4}$ |

Figure B51



# Appendix C1

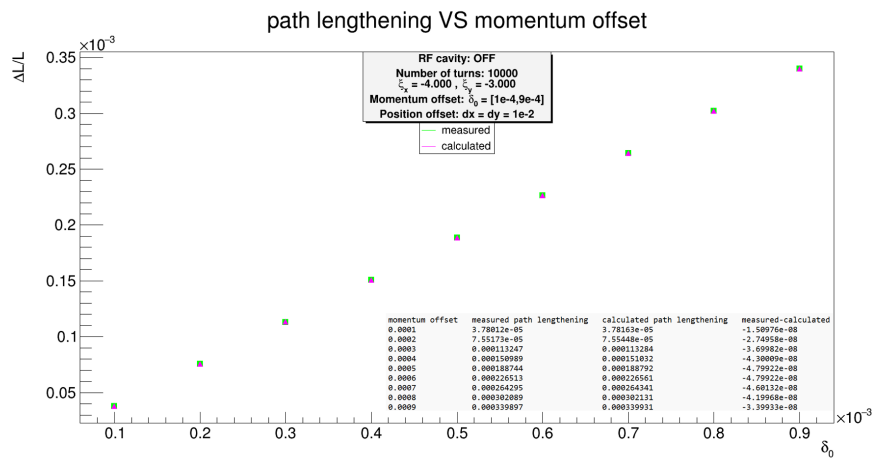


Figure C1

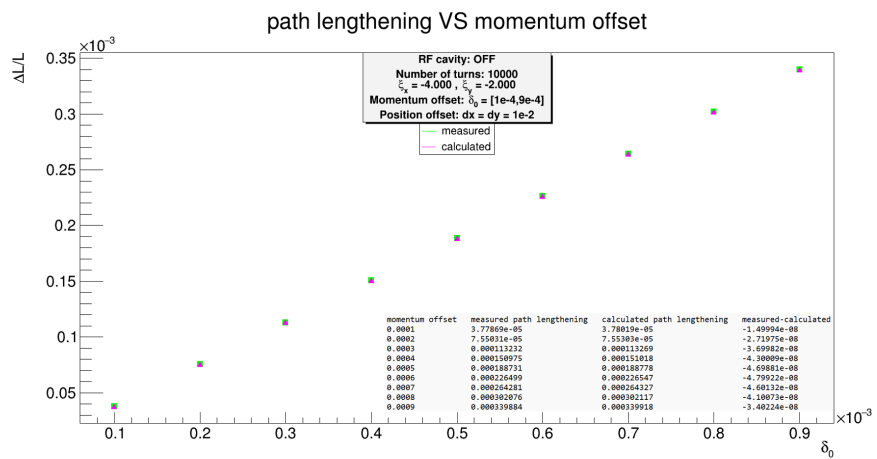


Figure C2

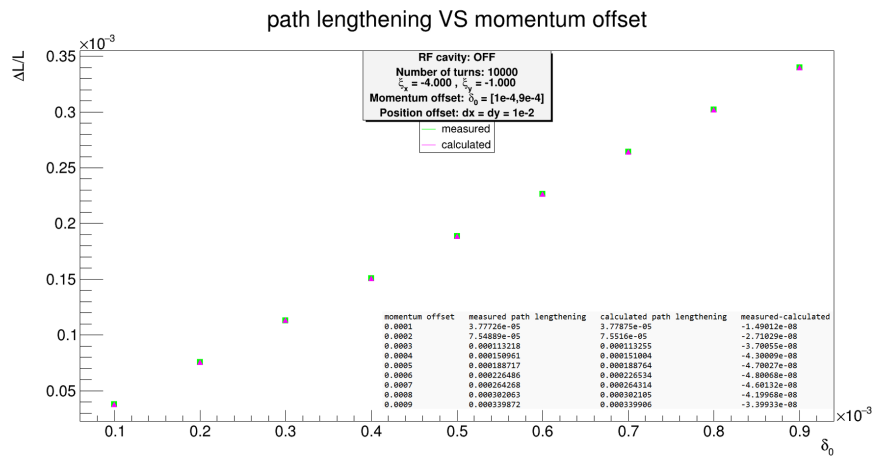


Figure C3

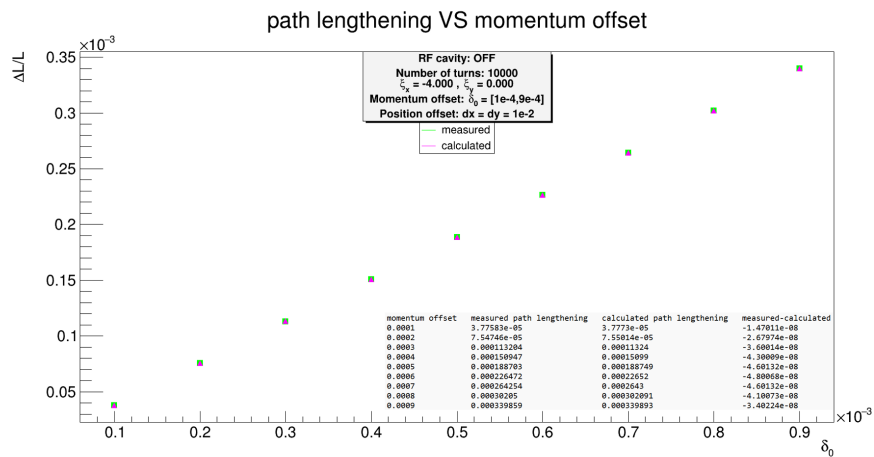


Figure C4



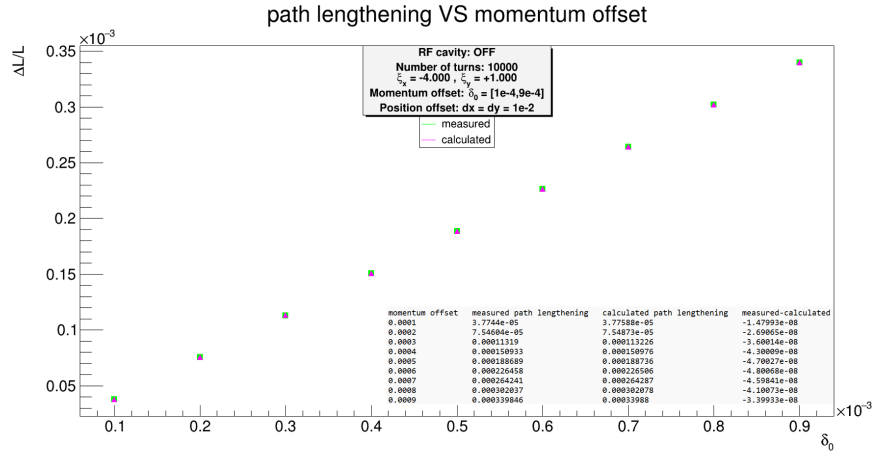


Figure C5

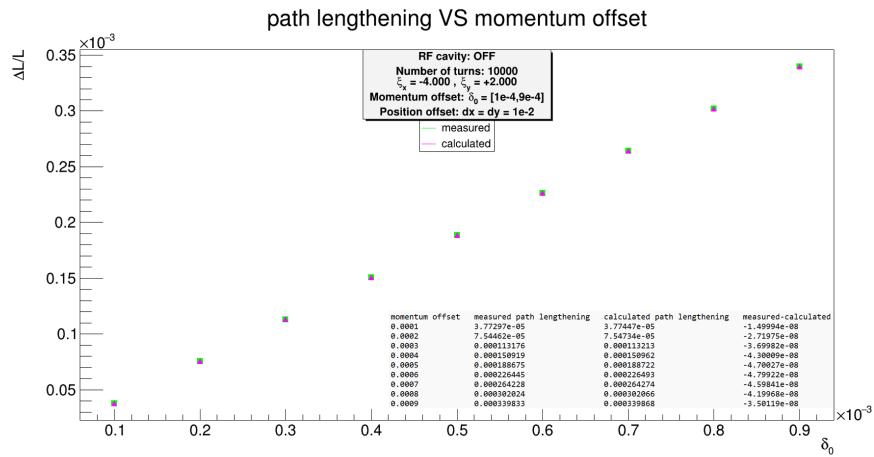


Figure C6

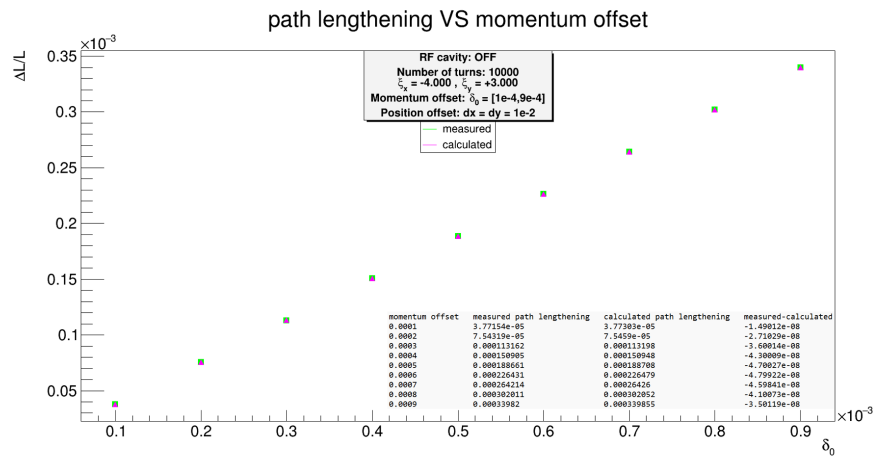


Figure C7

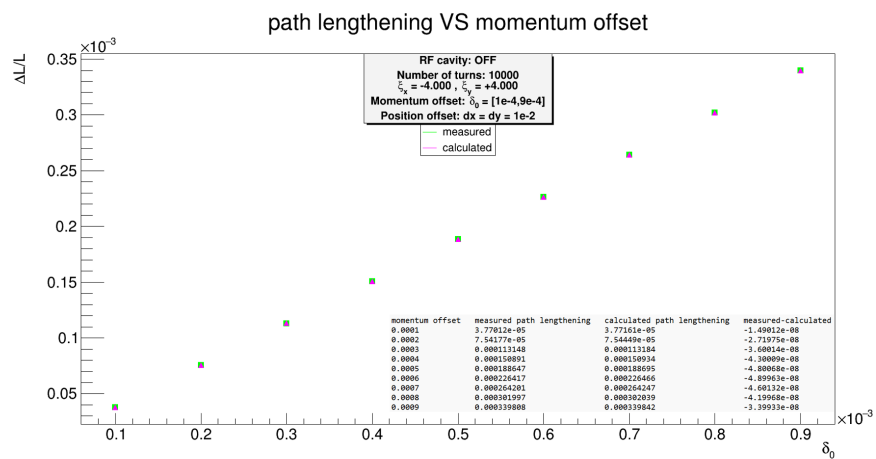


Figure C8

# Appendix C2

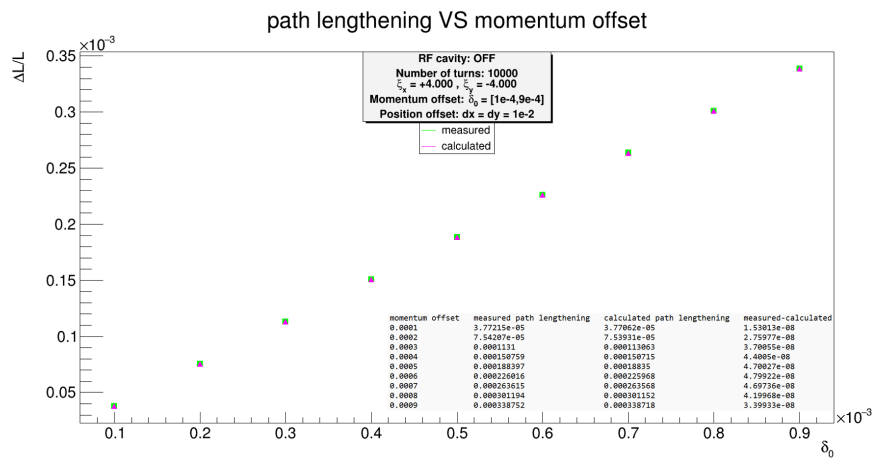


Figure C9

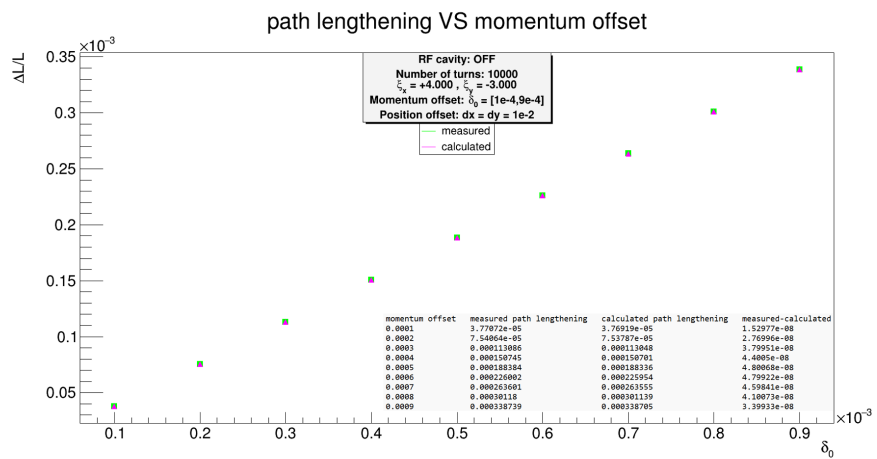


Figure C10

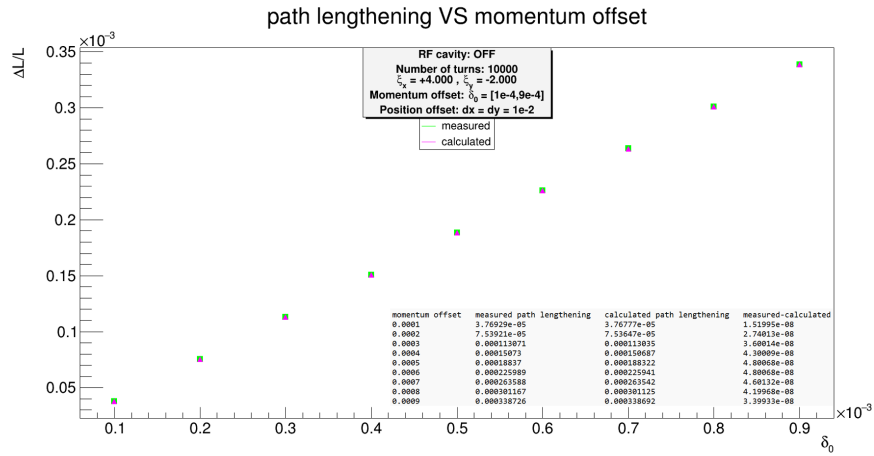


Figure C11

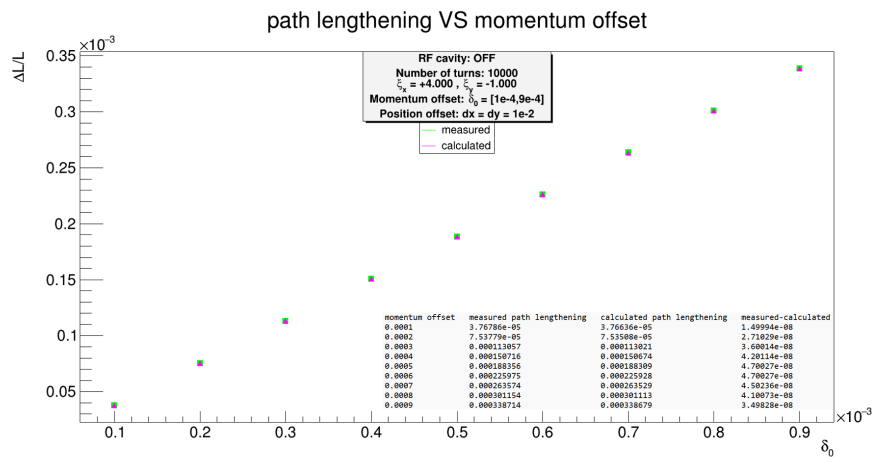


Figure C12

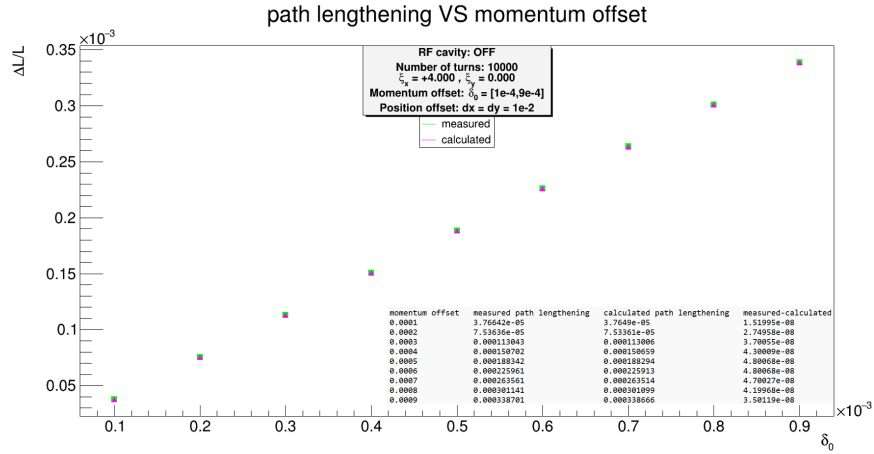


Figure C13

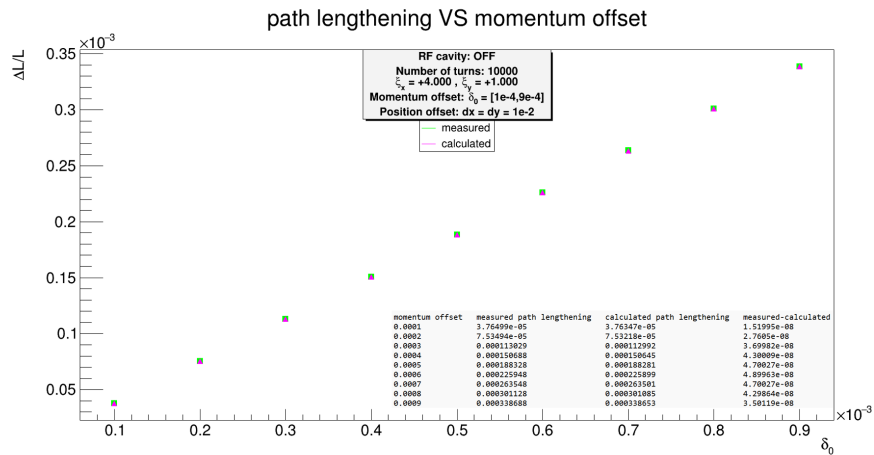


Figure C14

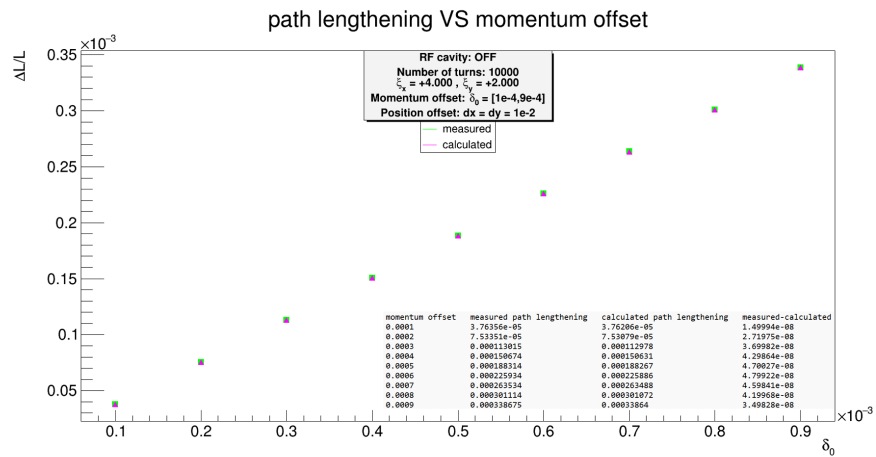


Figure C15

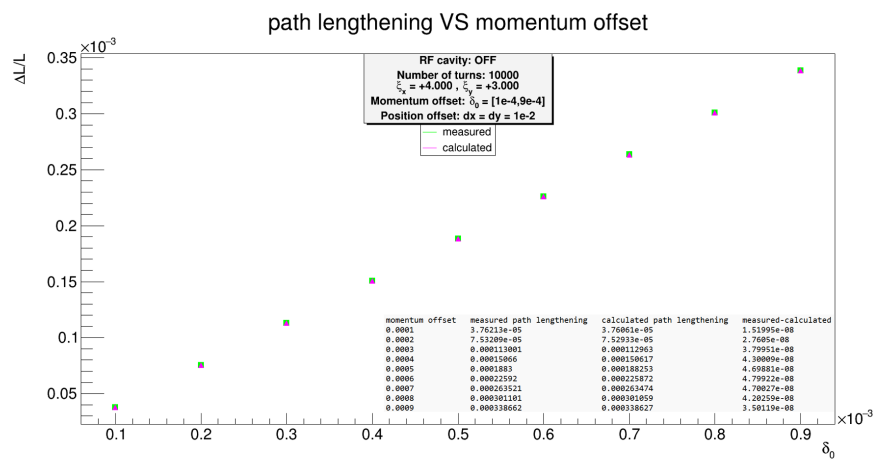


Figure C16

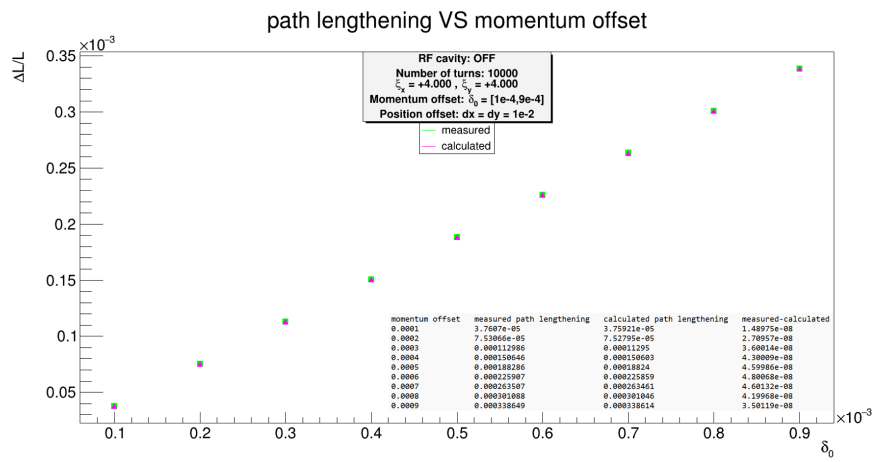


Figure C17





# Appendix D

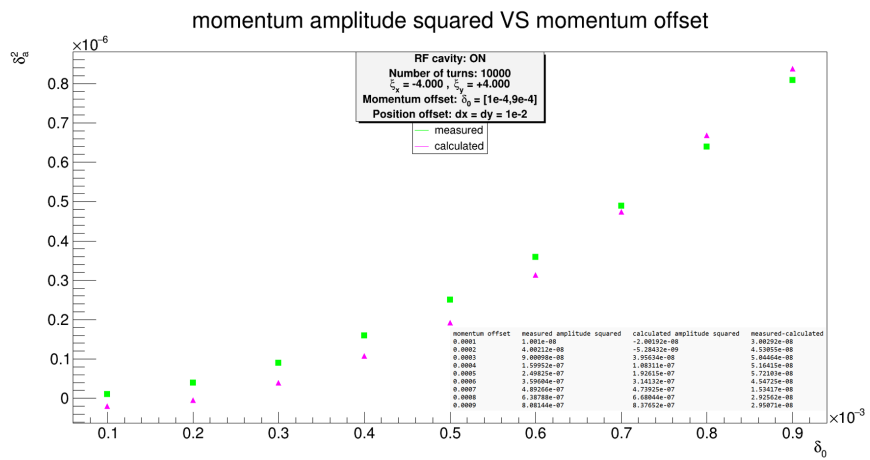


Figure D1

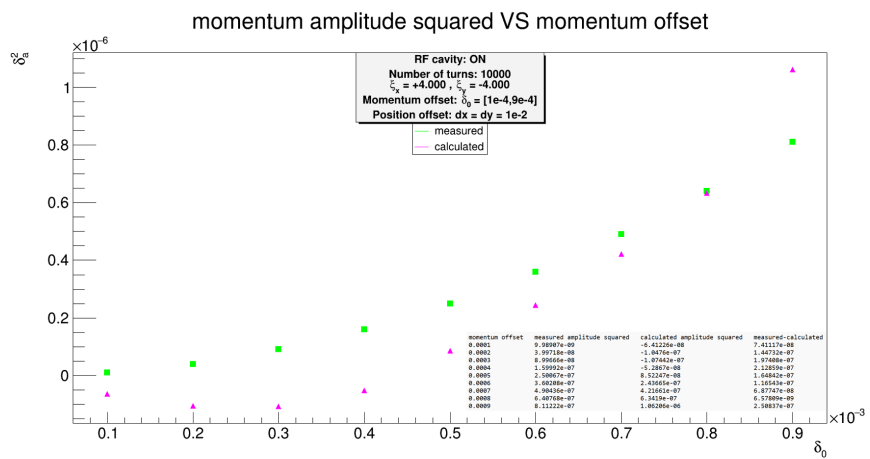


Figure D2

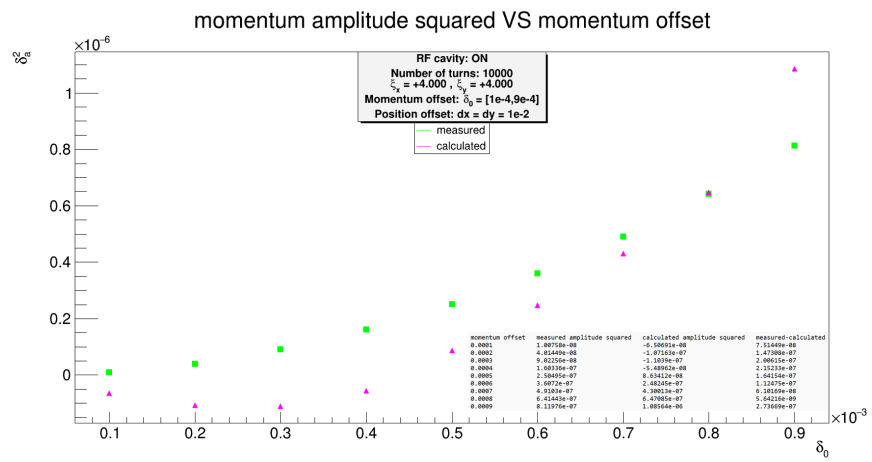


Figure D3

# Bibliography

- [1] Falastine Abusaif et al. “Storage Ring to Search for Electric Dipole Moments of Charged Particles–Feasibility Study”. In: *arXiv preprint arXiv:1912.07881* (2019).
- [2] Jim Alexander et al. “The storage ring proton EDM experiment”. In: *arXiv preprint arXiv:2205.00830* (2022).
- [3] Benat Alberdi Esuain. “Optimization of Injection in COSY”. PhD thesis. RWTH Aachen University, 2019.
- [4] Takeshi Fukuyama and Alexander J Silenko. “Derivation of generalized Thomas–Bargmann–Michel–Telegdi equation for a particle with electric dipole moment”. In: *International Journal of Modern Physics A* 28.29 (2013), p. 1350147.
- [5] Greta Guidoboni. “Spin Coherence Time studies for the storage ring EDM search.” In: *Pubblicazioni dello IUSS* 8.1 (2014), pp. 1–86.
- [6] Wiedemann H. *Particle accelerator physics*. Springer Nature, 2015.
- [7] Andreas Lehrach et al. “Design of a prototype edm storage ring”. In: *Proceedings, 23rd International Spin Physics Symposium: Ferrara, Italy*. 2018, pp. 10–14.
- [8] Paolo Lenisa. “Search for Electric Dipole Moments of Charged Particles with Polarized Beams in Storage Rings”. In: *The 18th International Workshop on Polarized Sources, Targets, and Polarimetry, Knoxville*. 2019.
- [9] Edwards D.A. & Syphers M.J. *An introduction to the physics of high energy accelerators*. John Wiley & Sons, 2008.
- [10] Zhanibek Omarov et al. “Comprehensive symmetric-hybrid ring design for a proton EDM experiment at below 10- 29 e· cm”. In: *Physical Review D* 105.3 (2022), p. 032001.
- [11] Vera Poncza. *Extensive optimization of a simulation model for the electric dipole moment measurement at the Cooler Synchrotron COSY*. Tech. rep. Kernphysikalische Großgeräte, 2021.

- [12] Marcel Rosenthal. “Experimental benchmarking of spin tracking algorithms for electric dipole moment searches at the Cooler Synchrotron COSY”. PhD thesis. Universitätsbibliothek der RWTH Aachen, 2016.
- [13] Lee S.Y. *Accelerator physics*. World Scientific Publishing Company, 2018.
- [14] Rahul Shankar, Maximilian Vitz, and Paolo Lenisa. “Optimization of spin coherence time at a prototype storage ring for electric dipole moment measurements”. In: *Proceedings of the 24th International Spin Symposium (SPIN2021)*. 2022, p. 021105.
- [15] Yoshihiko Shoji. “Dependence of average path length betatron motion in a storage ring”. In: *Physical Review Special Topics-Accelerators and Beams* 8.9 (2005), p. 094001.
- [16] Maximilian Vitz, Andreas Lehrach, Rahul Shankar, et al. “Simulation and Optimization of the Spin Coherence Time of Protons in a Prototype EDM Ring”. In: *The 12th International Particle Accelerator Conference, Online*. 2021.